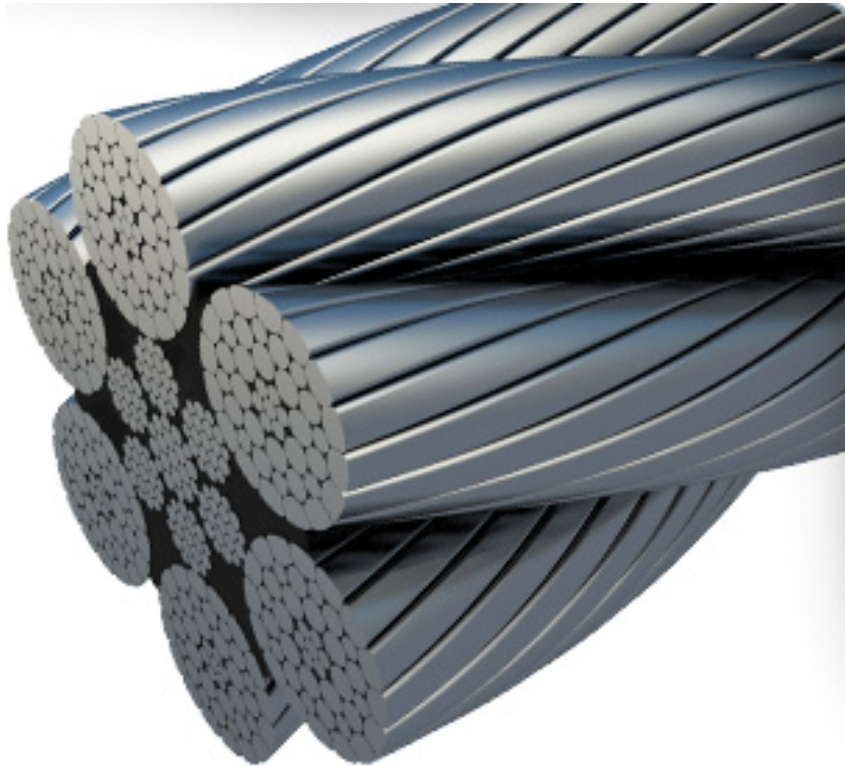


# Pieter Schelte Jacket Lift System

Behaviour of steel wire ropes subjected to severely oscillating tensile loads alternating between taut and slack.



*author:* Erik Robers  
*date:* September 2011



Department of Precision and Microsystems Engineering

## **Pieter Schelte Jacket Lift System**

Behaviour of steel wire ropes subjected to severely oscillating tensile loads  
alternating between taut and slack.

Name: E S Robers

Report no: 11.028

Coach: ir.J.Regelink

Professor: Prof.dr.ir.D.J.Rixen

Specialisation: Engineer Mechanics

Type of report: Masters Thesis

Date: Delft, October 12, 2011



## Acknowledgements

First I'd like to thank my family. Thank you for everything.

*Allseas* has given me the chance to freely pursue my interests within their context. I appreciate it that it was emphasized that graduating is a chance to do research that is not mainly aimed at practical implementation but also at personal curiosity.

I'd like to thank the following people for giving active support during this journey:

- My professor Daniel J. Rixen for support and direction.
- Jeroen Regelink for all discussions/conversations on wire ropes.
- Natalia Ermolaeva for providing in depth comments on the draft reports.
- Marijn Dijk for the general direction and support at the start of my graduation.
- Andre Steenhuis for sending me first to Hamburg to do a weight survey on the *Audacia* and later to the Shetland Islands for a good experience working on a pipeline construction site.

I've had a lot of good laughs with many colleagues. They provided a well needed comic relief on a very regular basis. Many have also given a lot of pointers with regards to graduating in general.

Thanks also to all my friends who have not forgotten me and have supported me while getting deep in the dark hole of graduating.



## Abstract

The pipe lay company Allseas is developing a new vessel, the Pieter Schelte. This vessel will be capable of not only laying gas and oil pipelines on the seabed, but also (de)commissioning oil platforms and the jackets that support them. Over 600 offshore installations have been constructed in the North Sea. Half of these installations are scheduled to be decommissioned before 2021. Up to 200 of these installations have been analyzed for removal. The jackets weigh up to 25000 ton.

Previous dynamic analysis has shown that tensile loads in the hoisting wire ropes for jacket decommissioning alternate between taut and slack. They also in- and decrease significantly faster than what is considered good working conditions. These characteristics are preferably avoided. However, avoiding these is a difficult and expensive task.

Possible effects on the steel wire ropes have been investigated that are subjected to these tensile load characteristics. It has been chosen to investigate the internal frictional energy generation due to inter-wire friction within the steel wire ropes. The resulting frictional energy generation has been applied on a cross-section of a steel wire to determine the temperature change. When temperature changes of the steel wires are too large, material structure changes can occur and consequently weaken the steel wires.





## Contents

<b>Acknowledgements</b>	<b>I</b>
<b>Abstract</b>	<b>III</b>
<b>List of abbreviations</b>	<b>1</b>
<b>List of symbols</b>	<b>3</b>
<b>1 Introduction</b>	<b>11</b>
<b>2 Problem definition</b>	<b>13</b>
2.1 Finding a Challenge . . . . .	13
2.2 Lifting a challenge . . . . .	16
2.3 Objectives . . . . .	17
2.4 Report Structure . . . . .	18
<b>3 Wire Ropes in General</b>	<b>21</b>
3.1 Brief History . . . . .	21
3.2 Construction . . . . .	21
3.2.1 Single-Strand-Ropes (SSR) . . . . .	21
3.2.2 Multi-Stranded-Ropes (MSR) . . . . .	22
<b>4 Selecting a Cause of Wire Rope Failure</b>	<b>25</b>
4.1 Elastic waves . . . . .	25
4.1.1 Stress Doubling . . . . .	27
4.1.2 Birdcaging . . . . .	28
4.2 Hockling . . . . .	30
4.3 Internal Heat Generation . . . . .	32
4.3.1 Clues for excessive internal friction . . . . .	33
4.3.2 On inter-wire friction . . . . .	35
4.3.3 Models on wire ropes for internal heat generation . . . . .	36
4.4 Conclusions . . . . .	38
<b>5 Implementing the Orthotropic Sheet Theory (OST)</b>	<b>41</b>
5.1 Basics of the OST . . . . .	42
5.1.1 Orthotropic Tensor . . . . .	42
5.1.2 Kinematics in Wire-Layer Continuum subjected to a tensile Strand Strain . . . . .	45
5.1.3 Radial Load Transfer in Multi-Layered Strands . . . . .	48
5.1.4 Orthotropic Compliances . . . . .	50
5.1.5 Effective Young's Modulus of a strand . . . . .	50
5.2 Implementation of the OST . . . . .	51
5.2.1 Implementation for SSR's . . . . .	51
5.2.2 Implementation for MSR's . . . . .	52
5.2.3 OST procedures . . . . .	54
5.2.4 Implementation for Dynamic Model for SSR's and MSR's . . . . .	57
5.3 Results . . . . .	58
5.3.1 Results for 39mm SSR . . . . .	58
5.3.2 Results for 40mm MSR . . . . .	60
5.4 Conclusions . . . . .	61
<b>6 Frictional Energy Generation and resulting Temperature Changes</b>	<b>63</b>

6.1	Frictional Energy Generation . . . . .	63
6.1.1	Multiscale $FE^2$ Modeling . . . . .	63
6.1.2	Wire Ropes used for Modeling . . . . .	64
6.1.3	Cyclic Load . . . . .	65
6.1.4	Non-Cyclic Load . . . . .	67
6.2	Temperature Change . . . . .	68
6.3	Conclusions . . . . .	68
<b>7</b>	<b>Conclusions and Recommendations</b>	<b>69</b>
7.1	Conclusions . . . . .	69
7.2	Recommendations . . . . .	70
<b>A</b>	<b>Wire Rope Geometry</b>	<b>75</b>
A.1	Core Wire of a Helical Strand (Single Helix) . . . . .	75
A.2	Wires in a Helical Strand (Double Helix) . . . . .	76
<b>B</b>	<b>Orthotropic Sheet Theory</b>	<b>81</b>
B.1	Symbols and Notation . . . . .	81
B.2	Strand Kinematics . . . . .	82
B.3	Internal Forces of a Strand . . . . .	87
B.4	OST Compliances . . . . .	90
B.5	Strand hysteresis under cyclic loading . . . . .	92
B.6	Strand's Young's Modulus . . . . .	95
B.7	Validation of implementation with Numerical Examples . . . . .	96
B.7.1	Validation . . . . .	97
B.7.2	Conclusions . . . . .	101
<b>C</b>	<b>Friction</b>	<b>103</b>
C.1	Coulomb's dry friction Law . . . . .	103
C.2	Masing's Rule . . . . .	104
<b>D</b>	<b>Dynamic Modeling</b>	<b>105</b>
D.1	Homogenized Model . . . . .	105
D.1.1	Mathematical model . . . . .	105
D.1.2	Solving Dynamic Model . . . . .	106
D.2	Multiscale $FE^2$ Model . . . . .	108
D.2.1	Mathematical model . . . . .	108
D.2.2	Solving Dynamic Model . . . . .	108
<b>E</b>	<b>Solving a set of non-linear functions</b>	<b>113</b>
E.1	Newton-Raphson . . . . .	113
E.2	Central Difference method . . . . .	114
E.3	Implementation in the OST . . . . .	115
	<b>Bibliography</b>	<b>117</b>

## List of abbreviations

CoG	: Center of Gravity
DP	: Dynamic Positioning
H&vR	: Hessels & van Rooij
JLS	: Jacket Lift System
KCI	: Korndörffer Contracting International
MSR	: Multi-Stranded Rope
OST	: Orthotropic Sheet Theory
OT	: Orthotropic Tensor
PS	: Pieter Schelte
SSR	: Single-Stranded Rope
TLB	: Tilting Lifting Beam
TP	: Thesis Program
WR	: Wire Rope



## List of symbols

### OST

$D$	: Wire diameter.
$L$	: Undeformed strand length.
$L'$	: Deformed strand length.
$P_{ine}$	: Inter-wire line contact force <i>with</i> in general.
$P_{MS}$	: Inter-wire line contact force <i>with</i> outer layer taken into account.
$P_{RC}$	: Inter-wire line contact force <i>without</i> outer layer taken into account.
$R$	: Wire radius.
$S_1$	: Axial strain of the wire in the layer.
$dS_1$	: Change in wire axial strain due to deformation of the wires.
$S_2$	: Approach strain normal to $S_1$ between the centres of wires in line contact.
$S_{6T}$	: Tensor shear strain within wire layer.
$S_{ij}$	: Compliances of strain tensor of wire layer.
$S'_1$	: Axial strain of strand.
$S'_2$	: Net radial strain of strand; $S'_2 = S'_{2C} - S'_{2R}$ .
$S'_{2C}$	: Radial strain of layer with the rigid core removed.
$S'_{2R}$	: Strand radial strain due to changes of lay-angle where the wires are treated as rigid bodies and the rigid core is absent.
$S'_{ij}$	: Compliances of strain tensor of strand.
$T_1$	: Wire axial tension.
$T_2$	: Wire diametral tension.
$T_6$	: Inter-wire tangential tension.
$X_{MS}$	: Resultant force in radial direction <i>with</i> outer layer taken into account.
$X_{RC}$	: Resultant force in radial direction <i>without</i> outer layer taken into account.
$X_R$	: Radial force of wire layer $i$ acting on wire layer $i+1$ .
$P_{TR}$	: Normal forces on inter-layer trellis contact patches.
$T_6$	: Wire layer shear tension.
$n_i$	: Number of wires in layer $i$ .
$r$	: Helix radius before deformation.
$r'$	: Helix radius after deformation.
$\alpha$	: Lay-angle of wires before deformation.
$\alpha'$	: Lay-angle of wires after deformation.
$\beta$	: Tangential inter-wire slippage within wire layer.
$\mu$	: Friction coefficient.
$\nu$	: Poisson's ratio.
$\psi$	: Specific energy dissipation per cycle for a constant load perturbation, $\psi = \frac{\Delta U_{cycle}}{U_{cycle}}$ .
$\delta_n$	: Diametral deflection between two adjacent wires within a wire layer.

## Wire Rope Geometry

$x_0, y_0, z_0$	:	Coördinates in the inertial frame where the z-axis coincides with the core wire of the core strand.
$x_1, y_1, z_1$	:	Coördinates in the inertial frame where the z-axis is tangent with the core wire of the laid strand. Note that the location is dependent on the polar angle $\phi_{ab}$ .
$r_{ab}$	:	Helix radius of wire in layer b of strand a.
$\phi_{ab}$	:	Polar angle describing the helical wire in layer b of strand a.
$\alpha_{ab}$	:	Lay angle describing the helical wire in layer b of strand a, where right-hand lay is positive.
$L_{ab}$	:	Length of the helical wire in layer b of strand a.
$R_\phi$	:	Matrix rotating the $x, y, z_1$ - frame around its z-axis with polar angle $\phi_{ab}$ .
$R_\alpha$	:	Matrix rotating the $x, y, z_1$ - frame around its x-axis with lay angle $\alpha_{ab}$ .
$R_{\phi\alpha}$	:	The final rotation matrix by performing the multiplication $R_\phi R_\alpha$ where the order is of essence.

## Dynamic Modeling

$x_i$	:	Position with respect to origin of 1 dimensional $x_i$ frame.
$\dot{x}_i$	:	Velocity (first time derivative of $x_i$ ) with respect to origin of 1 dimensional $x_i$ frame.
$\ddot{x}_i$	:	Acceleration (first time derivative of $\dot{x}_i$ ) with respect to origin of 1 dimensional $x_i$ frame.
$m_i$	:	Mass of element i.
$c_i$	:	Damping between element i and i-1, if i = 1 it is the damping between element 1 and the earth.
$k_i$	:	Stiffness between element i and i-1, if i = 1 it is the stiffness between element 1 and the earth.
$g$	:	Gravitational acceleration.

## List of Figures

1	Sequence of jacket lift. . . . .	12
2	Example of axial loading taken from ADAMS model. . . . .	14
3	Potential effects due to expected loading during jacket decommissioning by the PS. . . . .	18
4	Chosen wire ropes for investigation. . . . .	19
5	Clarification of wire rope construction and associated terminology [44]. . . . .	21
6	Types of Single-Strand Ropes. . . . .	22
7	Types of Multi-Stranded Ropes. . . . .	23
8	The DB2K wire rope . . . . .	23
9	Examples of failing wire ropes. . . . .	25
10	An example of tensile loading on one wire rope during jacket decommissioning. . . . .	26
11	Elastic wave attenuation (left) and simultaneous occurrence of elastic waves (right) in a wire rope. . . . .	27
12	Example of birdcaging a.k.a core protrusion. . . . .	28
13	Picture of birdcaging and graph showing the border between separation and non-separation of outside wires/strands taken from [8]. . . . .	29
14	Velocities of wire rope elements subjected to a tensile load as shown in figure 10a. . . . .	30
15	Sequence of loop forming of a rod, due to sufficient initial twist combined with sufficient slack, followed by snarling, taken from [16]. . . . .	31
16	[12]:"Critical relative slack $\frac{B}{L}$ for double-rope sets: 6-mm diameter hanging cables and 16 mm diameter cable on the ground. Solid lines give the theoretical prediction following equation 4. Marks correspond to test results." . . . . .	32
17	An example of a 'cup and cone' failure type. . . . .	33
18	A pearlite structure is desired (left), it is hard and tough. The stripes are plates of Ferrite and Cementite. The martensite structure (right) has a needle like appearance and is hard and brittle. A layer of martensite that as formed at the surface of a wire and has resulted in crackforming. . . . .	34
19	Schematical representation of line contact (right) and trellis contact (left). . . . .	35
20	The force equilibrium of a thin helical wire which forms the base of Costello's [7] wire rope theory and also for the theories developed by M. Raof. . . . .	36
21	Examples of specific heat dissipation derived theoretically with the OST developed by M. Raof taken from [24]. . . . .	37
22	Examples of FEM approaches. . . . .	38
23	The basic approach of the OST is to first analyse each wire layer separately. Each wire layer is approached as a cylindrical shell. . . . .	42
24	Illustrations of the strains in a cylindrical shell as defined for the OST. . . . .	43
25	Symmetry planes of the of the orthotropic tensor of a wire layer. . . . .	43
26	Side view (left) and cross-section (right) of a strand. . . . .	44
27	Change in helix radius due to change in lay-angle $\alpha$ where the wires are treated as rigid bodies. . . . .	46
28	Illustration of $dS_1$ as a result of strand tensile strain $S'_1$ when $S_1$ is kept zero and only the resulting lay-angle $\alpha'$ after deformation <i>is</i> taken into account. . . . .	47
29	A sketch clarifying the determination of wire slippage between two adjacent helical wires. . . . .	47

30	Forces, $P_{RC/MS}$ and $X_{RC/MS}$ , acting on the wire center (left) and the resultant force $X_{R_i}$ (right) when the multilayered strand is considered. . . . .	48
31	Cross-section of two wires in line-contact showing the diametral deflection $\delta_n$ as a result of the line-contact force $P_{RC}$ . . . . .	49
32	Flow chart for the energy dissipation $\psi$ of a SSR. . . . .	51
33	Schematical representation of approach 2 for applying the OST to MSR's. . . . .	52
34	Flow chart for determining the energy dissipation $\psi_{MSR} = \frac{\Delta U_{cycle}}{U_{cycle}}$ of a MSR depending on $\frac{\text{Load Perturbation}}{\text{Mean Load}}$ . . . . .	53
35	Flow chart for determining the effective Young's Modulus $E_{eff}$ of a SSR depending on $\frac{\text{Load Perturbation}}{\text{Mean Load}}$ . . . . .	55
36	Flow chart for determining values of a strand kept constant around a mean load. . . . .	55
37	Hysteresis cycle of friction with stick-slip regime. . . . .	56
38	Flow chart for determining the energy dissipation $\psi_{SSR} = \frac{\Delta U_{cycle}}{U_{cycle}}$ of a SSR depending on $\frac{\text{Load Perturbation}}{\text{Mean Load}}$ . . . . .	56
39	Flowchart of the implementation of the OST in a dynamic model where the hysteretic behavior is taken into account for a <i>cyclic</i> loading but not for <i>non-cyclic</i> loading. For the non-cyclic loading the slippage is continuously in the full-slip regime. . . . .	57
40	No-slip and full-slip effective Young's Modulus for the 39mm strand. . . . .	59
41	Specific damping $\psi_{strand} = \frac{\Delta U}{U}$ for the 39mm strand. The mean load is 0.415MN . . . . .	59
42	The no-slip and full slip Young's Moduli of 40mm MSR and its strands. . . . .	60
43	Specific damping $\psi_{strand} = \frac{\Delta U}{U}$ for the 40mm IWRC. The mean load is 0.204MN. . . . .	61
44	Schematical representation of multi-scale FE <sup>2</sup> modeling of a wire rope. . . . .	63
45	Cyclic axial load around a mean load applied . . . . .	65
46	Hysteresis loop for the cyclic axial load shown in 45 around a mean load of 0.42MN . . . . .	66
47	Heatflux (kW) in a wire layer of the bottom wire rope element resulting from the cyclic axial load shown in 45 around a mean load of 0.42MN . . . . .	66
48	Random like axial loading occurring during Jacket decommissioning by the PS modeled in ADAMS by [4]. . . . .	67
49	Energy flux on line contact area due to axial loading shown in figure 48. . . . .	67
50	Temperature change after 0.5s of the highest magnitude of heat flux, 11kW/m <sup>2</sup> resulting from non-cyclic dynamic model for the 39mm SSR. . . . .	68
51	Cross-section of a MSR wherein the use of the subscripts in this section are clarified. . . . .	75
52	Geometry of the core wire of a helical strand in the first layer. . . . .	76
53	Geometry of the centre wire of a helical strand in the first layer. . . . .	77
54	Plot of a helical wire (red) around the core wire (black) of a helical strand. . . . .	79
55	Lay angel $\alpha$ as defined by the different authors. . . . .	81
56	Cross-section of helical wire normal to strand axis. . . . .	84
57	eeeh . . . . .	85
58	Sketch clarifying the derivation for the wire slippage between two adjacent helical wires. . . . .	86
59	Strain relations between strand and wire layer. . . . .	87
60	Cross-section of two wires in line-contact showing the diametral deflection $\delta_n$ as a result of the line-contact force $P_{RC}$ . . . . .	88
61	Forces, $P_{RC/MS_i}$ and $X_{RC/MS_i}$ , acting on the wire center (left) and the resultant force $X_{R_i}$ (right). . . . .	90
62	Hysteresis loop as applied in the OST. . . . .	93



63	$P_{RC}$ data vs $X_{RC}$ data for a 39mm strand. The construction data can be found in table 3 taken from [23] and [26]. . . . .	98
64	Plot of tensile strand strain $S_1$ vs line contact force $P_{MS}$ produced by the TP (left) and produced by M. Raof in [23] (right) . . . . .	99
65	Frictional energy dissipation in a strand subjected to a mean tensile strand load of 0.42MN as a function of load perturbation. . . . .	99
66	Results for the 39mm SSR by the TP and from [24]. . . . .	100
67	Schematical representation of Coulomb's law. . . . .	103
68	Graphical representation of function accomodating for stick-slip behavior. . . . .	104
69	FEM of wire rope with viscous damping between the wire rope elemtens . . . . .	106
70	Scheme for Linear Newmark Intergration $\beta$ method . . . . .	107
71	First Eigen Frequency for corresponding amount of elements. . . . .	107
72	FEM of wire rope with frictional damping between the wire rope elemtens . . . . .	108
73	Scheme for Non-Linear Newmark Intergration $\beta$ method. . . . .	109
74	Scheme for Non-Linear Newmark Intergration $\beta$ method where the OST yielding the microscopic behavior is implemented in the convergence routine. . . . .	110
75	Scheme for Non-Linear Newmark Intergration $\beta$ method where the OST yielding the microscopic behavior is kept outside the routine. It thus only yields the microscopic behavior as a consequence of the dynamic response but it does not influence the dynamic response. . . . .	111
76	Graphical representation of Newton-Raphson method. . . . .	113
77	Graphical representation of Central-Difference method. . . . .	114



## List of Tables

1	Assumptions of interest made for the models investigated in [43] . . . . .	16
2	Rope construction terminology. Pictures are not scaled with respect to each other. . . . .	22
3	Construction details of a 39mm SSR taken from [26]. . . . .	58
4	Construction details of a 40mm MSR taken from [29]. . . . .	58
5	Relative errors of implementation of Newton-Raphson for solving for line contact forces. . . . .	97



## 1 Introduction

Allseas engineering is developing a new vessel the Pieter Schelte (PS). It will be able to (de)commission oil platforms and lay pipes.

In this thesis the focus is on the lifting process of a jacket, see figure 1.

During this operation the tensile forces in- and decrease significantly fast. It needs to be investigated.

What can the results be and do actions need to be taken to avoid these loading characteristics.

Initially four possible effects have been investigated:

- Stress-Doubling
- Birdcaging
- Hockling
- Frictional Energy Generation

The latter has been investigated further. However, birdcaging and hockling might also occur. For the investigation the *Orthotropic Sheet Theory* (OST) by M.Raoof has been applied. This is a very elaborate theory describing various aspects of wire rope behavior. Nevertheless, it has not been applied much. Only few papers mention it. No papers have been encountered where the theory has actually been applied.

After getting into the theory, it looks very convincing to describe wire rope behavior very well. Aspects like inter-wire slippage have also been investigated with elaborate FEM models. The OST, however cumbersome to implement, once running can yield the same results a lot faster.

While trying to understand the OST, it also gives great insight into wire rope behavior. Many intermediate interesting results can be investigated.

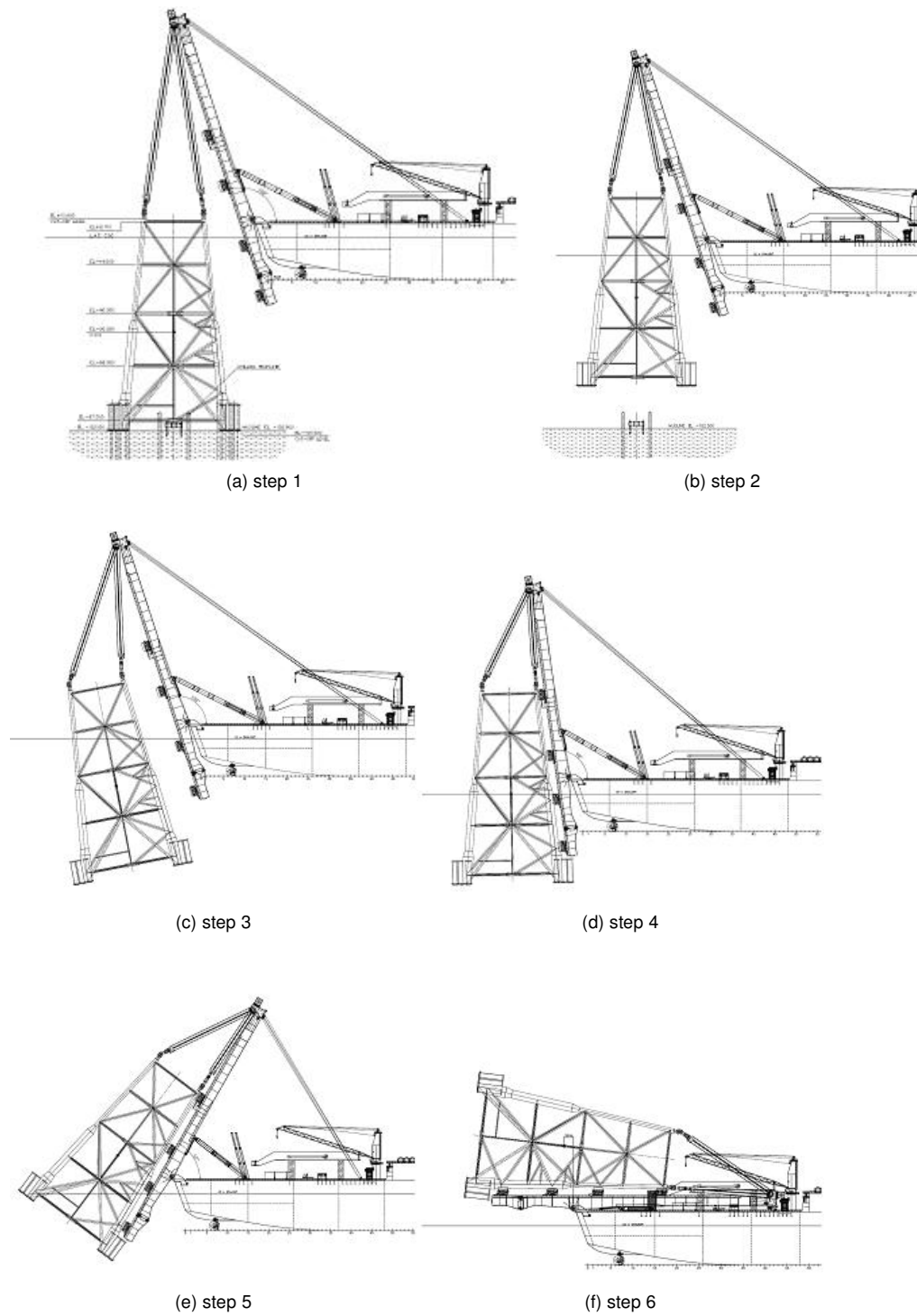


Figure 1: Sequence of jacket lift.

## 2 Problem definition

### 2.1 Finding a Challenge

At first glance it might seem that lifting a jacket out of the water with the *Pieter Schelte* (PS) should not be too complex. Just attach a few wire ropes to the jacket and turn on the winches until the jacket is hoisted to the desired height. As can be seen in Figure 1, at the desired height the jacket will then be aligned and in touch with the Tilting Lifting Beams (TLB). These TLB's then tip to the horizontal position, the jacket is skidded on board and the jacket is ready to be transported back home.

Unfortunately this operation is more complicated than described above. The sequence depicted in figure 1 shows a situation full of assumptions. There are no waves, it is only 2D, the vessel appears to be perfectly still and there are many more. Certain influences, if not all, are obviously left out, or, in other words, their effects are assumed to be negligible. Of course, Figure 1 is just an impression of the concept.

The question now becomes what are these influences and how to deal with them? Do they need a solution or is investigation of an influence already enough. The result can be that indeed the influence in question can be neglected. The research to determine the points of attention on the lifting phase of the jacket has been done by Florian J.M. Wasser(FJMW)[43]. He defined his objective as:

*Determination of key influences on the dynamic behaviour of substructure and lift system during the initial lifting phase.*

The effects that were analyzed are:

- The effect of changing the jacket size.
- The effect of changing the characteristics of the jacket drag.
- The effect of hoist wire rope stiffness and configuration.
- The effect of wave loading on the jacket.
- The effect of current loading on the jacket.
- The effect of horizontal and vertical seabed forces.
- The effect of horizontal and vertical foundation forces.

Four different dynamic models have been developed:

1. Hessels & van Rooij (H&vR)
2. Korndörffer Contracting International (KCI)
3. Model 1(FJMW)
4. Model 2(FJMW)

All these models have extensively been described in [43]. It should also be noted that model 1 is found in [43] to be inappropriate to get a good understanding of the dynamic effects.

This thesis will zoom in on one or more of the dynamic aspects discussed in [43]. A choice of conclusions and assumptions of the models above will be considered. These are shown in the next two paragraphs. Of these conclusions and assumptions a choice has been made for further investigation.

### Conclusions found in [43]

Of the many conclusions mentioned in [43], three have been chosen to be of interest and are repeated here:

1. "The occurrence of hoist wire rope slack is concluded for all simulations where regular waves are applied on the vessel. Peak forces during two occurrences of slack do not lead to forces higher than the maximum hoist wire rope capacity. Also in still water simulations slack wire ropes are detected, however with smaller corresponding peak forces."
2. "The occurrence of jacket support point re-bouncing is concluded for all simulations where regular waves are applied on the vessel. Applied peak forces by the support points during re-bouncing can be higher than when the jacket is at rest. Also in still water simulations re-bounces are detected, however with smaller corresponding peak forces."
3. "The maximum hoist velocity of the Jacket Lift System is too low to avoid the occurrence of slack wire ropes or re-bouncing. Hoisting speeds up to 10 times higher are required to compensate for the heave motion of the TLB tips when waves are applied on the vessel."

The jacket will bounce off the bottom due to the heaving motion of the vessel. This will cause the wire ropes to alternate between taut and slack. And even though this slacking of the wire ropes will not result in wire rope forces exceeding the Minimum Breaking Load (MBL), this does not assure there are no negative effect on the wire ropes. Tensile loading of wire ropes characteristic of the loading has been known to make wire ropes fail prematurely. An example of the characteristics of this type of loading is shown by an Adams model developed by E. Belderbos [4]. A result is shown in figure 2.

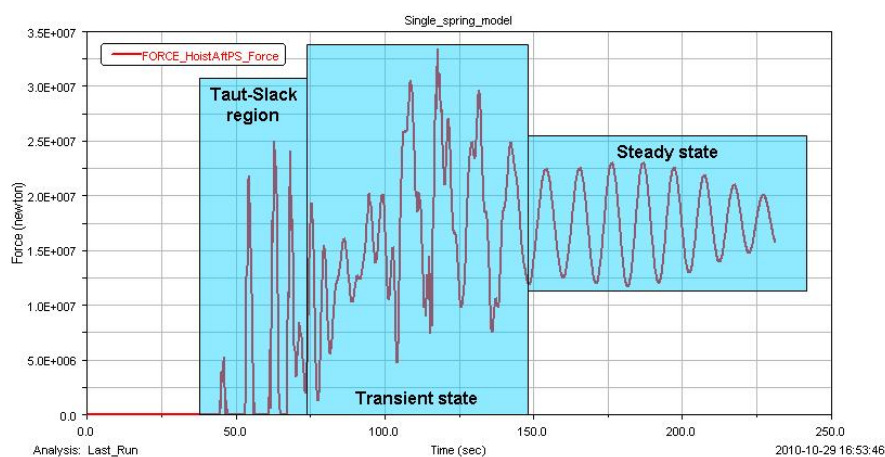


Figure 2: Example of axial loading taken from ADAMS model.

It is clear from the third conclusion that the taut - slack situation is unavoidable unless the hoisting speed is increased. Due to the scale, simply buying a faster winch is not an easy straightforward



solution. The hoisting velocity is 0.05 m/s, and this will need to be increased up to a velocity at least ten times higher according to [43]. One can imagine the extra space and power as well as the extra costs needed to realize this upgrade.

Another way to counter effect these taut - slack situations combined with bouncing of the jacket on the seabed, is to install a heave compensating system, i.e. with powerful winches or a hydraulic system with gas cylinders, to keep the wire ropes under tension. This solution, too, will add significant cost to the jacket (de)commissioning system, it is important to know whether the taut - slack situation is actually a problem or not. Preferably, the need for the two above mentioned solutions should be avoided.

Even if the expected shock loads do have a damaging effect on the wire ropes, it can still be more economical to accept a lower lifespan of the wire ropes than to design and produce a system to avoid these loads. What will be very important with this choice is to get enough insight in the damaging process to make proper decisions concerning the lifespan of the wire ropes. One can imagine the potential devastating effects on men and/or machine were the wire ropes to break during service.

### Assumptions made in [43]

Each model is based on assumptions. One has to be careful that they are valid and that they do not hide any non-negligible effects. Mostly, assumptions are made as it is known that certain influences or aspects of a system are negligible. One often applied example is the assumption of linearity around an equilibrium configuration of a system. Also for a first insight into a question it is not necessary to go into much detail.

In Table 1, assumptions of interest are listed as they are an example of convenience.

It is common to model wire ropes as built up of linear springs with no self-weight. In most applications this is a good approximation.

To model the dynamics of the lifting phase it is computationally convenient to assume the jacket to be rigid. This means that the Eigen modes, other than the rigid body modes, of the jacket are not taken into account. These modes will be excited each time the jacket bounces of the sea bottom as the impacts occurring during the bouncing can be nearly the same as applying a Dirac delta function to the structure. Theoretically it can be shown that this function excites all Eigen modes of the jacket. When the jacket starts to vibrate as a reaction to this bouncing, excited vibrations can be transferred to the hoisting wire ropes. What can the effects be? Will an Eigen mode of the wire rope be excited? If yes, what's next, what are the effects on the sheaves? How great will amplitudes of the vibrations in the wire rope be?

To get more insight into the excitation of the above mentioned modes of the jacket, it will be necessary to know more about the dynamic properties of the soil.

The assumption made for the *Dynamic Positioning* (DP) in the models is very interesting. It is either absent or, as in the KCI model, modelled as linear springs under pre-stress. Both are far from being realistic. The weight of the Jacket is large enough to have an effect on the dynamics of the vessel after lift off and will thus influence the behaviour of the DP. The models without DP will result in larger movements of the vessel and therefore have a different dynamic response of the jacket. The pre-stressed linear springs in the KCI model represent some sort of position control, at least it's bounded, though the way it is positioned does not have much reference with reality at best. Modelling the DP with pre-stressed linear springs is equivalent to modelling the DP as a proportional-only control system.

		H&vR	KCI	Model 2
1	<b>Hoisting wire ropes</b>	Modeled as linear spring without damping and no selfweight		
2		Modeled as rigid body		
3		No friction and suction		More details added
4	<b>Vessel</b>	No DP	DP modeled with pre-stressed mooring lines	No DP

Table 1: Assumptions of interest made for the models investigated in [43]

This type of control is not sufficient to control the position of a vessel to within i.e. 50cm of the desired position. The question here is what is the control algorithm of the DP of the vessel? Is the influence of the jacket weight taken into account by the DP system? Knowing this, one can get more insight into the dynamic behaviour of the vessel with jacket. The DP can then be implemented in the model to obtain more realistic results, especially with respect to retaining the desired position of the Pieter Schelte. Off course, as the DP contains a lot of blood sweat and tears, the deliverer Kongsberg will not just give it away. Though the current situation, unlike most vessels where the dynamics of the vessel don't change as dramatically, can be very interesting for them too. It might give new challenges and an opportunity to gain experiences that might increase their market value even more.

## 2.2 Lifting a challenge

From the above conclusions and assumptions three subjects are seen to be of interest for further investigation. They are shortly described here.

**Taut and slack wire ropes** It is evident that with the current design, the hoisting wire ropes will alternate between taut and slack. Not much is known about what happens exactly inside the wire rope, nor is it exactly clear what the wire rope forces will be if the wire rope is not assumed to be quasi-static.

Though what can be seen at this point, is that there are relative big accelerations which can lead to non-well known effects, i.e. the possibility of elastic waves is investigated in i.e. [21]. The main question is if any of these effects are dangerous or not. Is it absolutely necessary to avoid the taut-slack alternating situation?

**DP** The actual Kongsberg DP has not been taken into account. Only the KCI model incorporates some form of passive DP (pre-stressed linear springs). The behaviour of the vessel under influence of waves, wind and DP are essential for analysing not just the lifting process, but every (de)commissioning task. How well can the DP be expected to perform? If necessary, what can be done to increase the performance of the DP?

**Jacket and soil mechanics** The seabed has now been modelled as horizontal and vertical linear springs. What are the modes of the jacket that can be excited when bouncing on the seafloor? Can these resulting vibrations be transferred through the jacket onto the wire ropes? Can this lead to unwanted vibrations that might have a negative effect on the hoisting blocks, i.e. the sheaves?

## 2.3 Objectives

The DP challenge and the challenge with respect to the jacket and soil mechanics are already being addressed within Allseas. The challenge with respect to the taut-slack wire ropes, however, has not gotten enough attention yet. Though some work has been done, i.e. [4], the subject has not been clarified enough for Allseas to take a decision with respect to usage of the wire ropes for decommissioning a jacket. It is therefore chosen to investigate the taut-slack wire ropes and the associated fast in- and decreasing tensile loads. Within this subject it is necessary to learn which (negative) effects can be expected, thus:

*What are the possible effects of the expected loading during jacket lifting on the wire ropes and which of these effects, or combination thereof, is expected to have the greatest influence on the lifespan of the wire rope?*

After reading extensively the literature on wire ropes, it has become clear that it is necessary to limit the objective of this research further. There are many aspects of wire ropes to be researched and several possible effects to be investigated. The relevant ones are:

- Elastic linear and torsional waves causing:
  - Stress doubling; elastic waves reflect at the end termination and thus interfere with each other causing stress doubling, figure 3a.
  - Birdcaging; A combination of axial strain, negative or positive, torsional energy and elastic waves can cause wire/strand separation that can be permanent, figure 3b.
- Hockling; Slack wire ropes can form loops, consequently the wire rope can hockle when de-slacking, figure 3c.
- Frictional heat generation; Excessive frictional energy due to axial loading can cause a temperature rise consequently changing the material structure from pearlite to martensite possibly initiating crack formation, figure 3d.

It has been found here that the expected axial loading on the wire ropes can have elastic waves as a result. But these are not significant enough to cause either stress doubling and/or birdcaging.

From the ADAMS model developed in [4] it can be concluded that slack occurs. Within Allseas stability criteria with regards to hockling have been investigated and shown to be valid for multi-rope systems. These criteria need to be applied on hoisting wire ropes, but it is clearly not an underinvestigated effect.

Friction between the wires of a rope, however, is underinvestigated. It appears to play a significant role in most if not all the effects investigated. There is not much literature to be found on the subject, fortunately there are a few persons that have been dedicated to this subject. Especially the *Orthotropic Sheet Theory (OST)* developed by M. Raof looks very encouraging. It has, more or less, been verified with experimental results.

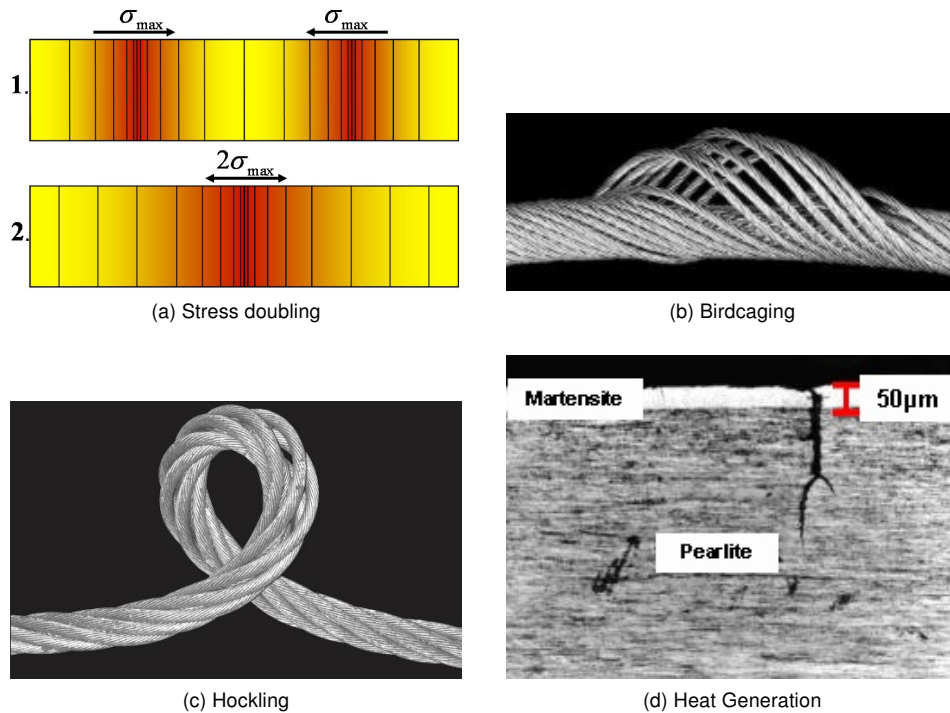


Figure 3: Potential effects due to expected loading during jacket decommissioning by the PS.

Related to friction is heat generation within a wire rope. Although steel is known to dissipate energy rather quickly, a few clues have been found to pursue this effect. One paper [36], for example, describes the possibility of an investigated wire rope that might have failed due to the consequences of excessive frictional heat generation.

The objectives of this thesis are:

*Implement the Orthotropic Sheet Theory (OST) by M. Raof for wire ropes by homogenization and multi-scale  $FE^2$  techniques in a dynamical model of the wire rope to investigate internal frictional energy generation.*

*Investigation of the temperature inside the wires of a wire rope due to the resulting energy generation.*

## 2.4 Report Structure

In this report the mathematics are mainly kept out of the main part. The reader that is interested in the details is referred to the appendices. The structure is as follows:

- Chapter 1: An introduction to the company *Allseas* and the project, development of the *Pieter Schelte* (PS), which has motivated this research.
- Chapter 2: The route to finding a final challenge for this thesis is described.
- Chapter 3: A brief history of wire ropes is given and the reader is introduced to the basic structures of wire ropes.
- Chapter 4: Several mechanism and their theories that can lead to failure are investigated. In the conclusion *internal heat generation* that is expected in the case of the hoisting procedure of the PS is chosen and the chosen theory is the *The Orthotropic Sheet Theory*.
- Chapter 5: The chosen theory , *Orthotropic Sheet Theory*, is explained, adapted and implemented.
- Chapter 6: The modelling of the internal heat generation is explained and the results are shown. The chapter starts with dynamic modelling followed by a heat conduction model.
- Chapter 7: The most important results are shown and discussed.
- Chapter 8: The main conclusions and recommendations are given.

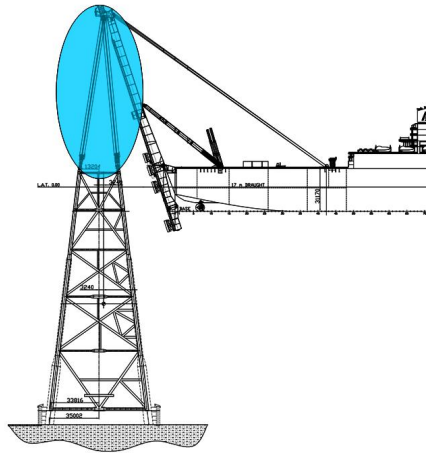


Figure 4: Chosen wire ropes for investigation.



### 3 Wire Ropes in General

Before the behavior of wire ropes can be investigated, one has to know about the structure. *First*, a very brief history will be given of the development of wire ropes, section 3.1. *Second*, a short description of the wire ropes is presented to get acquainted with the terminology and structure.

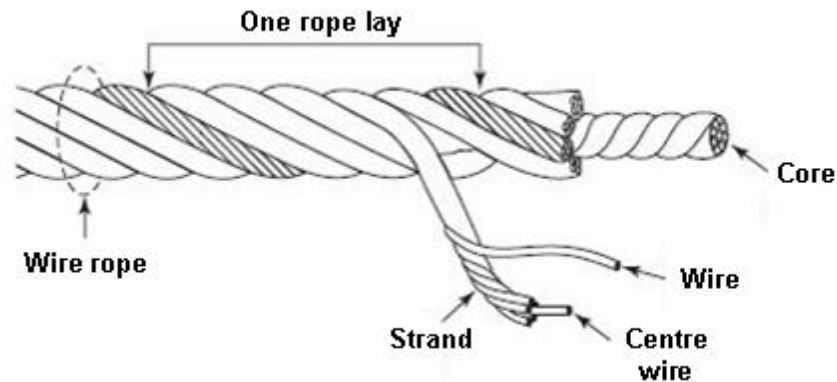


Figure 5: Clarification of wire rope construction and associated terminology [44].

#### 3.1 Brief History

The person that is accredited to inventing the first applied steel wire rope is a German mining engineer Wilhelm Albert. While working for the Mining and Forestry office in Clausthal, in 1829 he observed that iron mine-hoist chains can fail from repeated relative small loadings. His study and report is the first recorded account of metal fatigue.

He then took on the challenge of developing a steel wire rope to replace the iron chains. Reportedly, he is not the first to theorise about its use, though he is the first to make successful use of them. The first time he applied them in the mines in the Harz Mountains, Clausthal, Germany, it was 1834. They are seen as the forerunner of the modern day wire rope.

#### 3.2 Construction

A wire rope is constructed of wires. *First*, wires are combined to form a strand, and *second*, the strands can be combined to form a final wire rope. An overview can be seen in figure 5. Note that a strand can also be an end product. Thus the term *wire rope* can refer to a SSR and a MSR. In table 2 the terminology is clarified. Note that the pictures within this table are not scaled relative to each other.

##### 3.2.1 Single-Strand-Ropes (SSR)

A SSR starts with a straight wire. This wire is the core of a strand which is built up of wires that are laid helically around the core wire, see figure 6. How many wires per layer and how many layers of wires are applied, depends on the purpose of the strand. The most common is a seven wire strand shown in

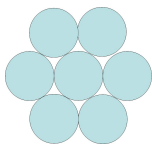
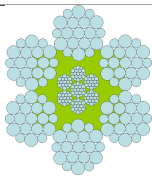
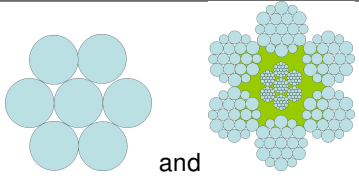
Single Stranded Rope (SSR)	
Multi Stranded Rope (MSR)	
Wire Rope (WR)	

Table 2: Rope construction terminology. Pictures are not scaled with respect to each other.

figure 6a, often referred to as 'ordinary' strand. There are many more varieties possible; The *ordinary* and three other main strand constructions are shown figure 6.

The *Filler* strand is characterized by the gaps between the outer layer and inner layer being filled with smaller diameter wires. The *Seale* strand consists of one layer of smaller diameter wires laid around the core wire, followed by a larger diameter outer layer. The diameters in *Warrington* strand alternate in the outer layer that are laid around an ordinary strand.

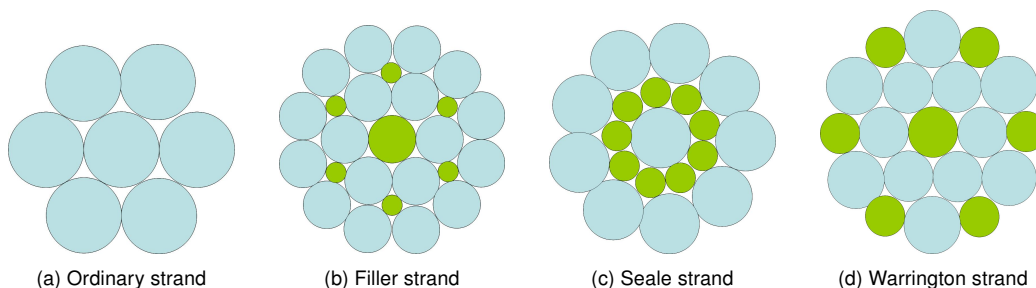


Figure 6: Types of Single-Strand Ropes.

### 3.2.2 Multi-Stranded-Ropes (MSR)

A MSR on its turn is constructed with the above mentioned strands which are helically laid around a core to form the wire rope, see figure 5. There are basically three types of wire rope core, see figure 7. The *fibre-core* rope may have i.e. hemp, plastic, or sisal as core material and offers the advantage of flexibility. For more strength, a *strand-core* rope can be used. Here all strands here are touching each other including the centre strand and some flexibility is lost. Another is the *IWRC*(Independent Wire Rope Core), where the core is a strand-core rope. The difference with the strand-core rope is that the



strand-core rope is *not* touching the outer strands and thus has more flexibility.

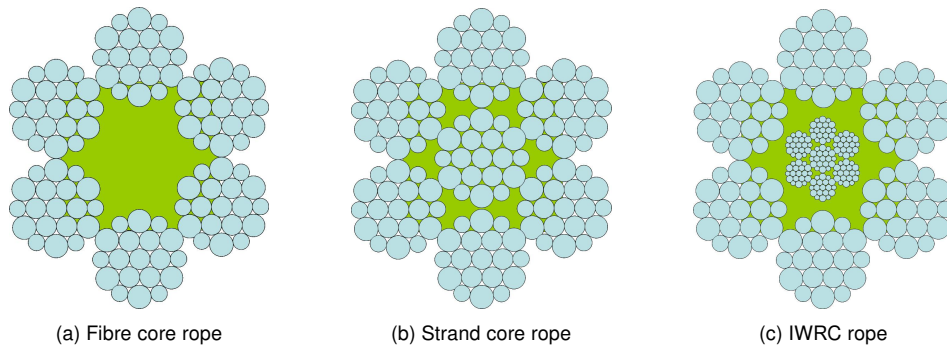
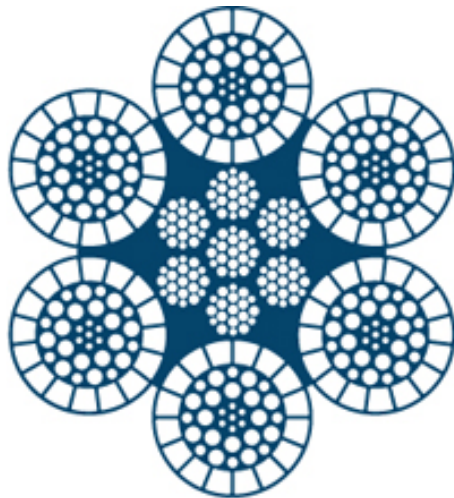
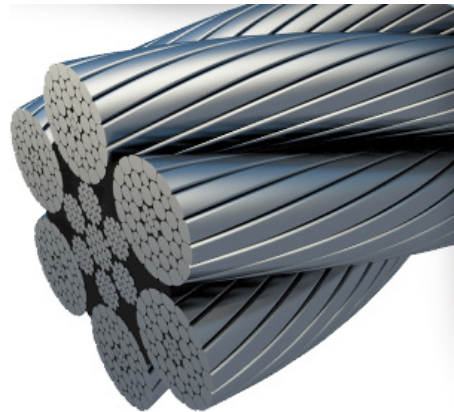


Figure 7: Types of Multi-Stranded Ropes.

The chosen wire rope by Allseas for the application of (de)commissioning of jackets is shown in Figure 8. Looking at the cross-section it can be clearly seen that it is an IWRC. The core wire rope is built up of Warrington strands. The outer layer of strands is an unconventional design. The centre wire of these strands taken with the first three layers can be seen as a Warrington strand with an extra layer. This Warrington strand has an outer wire layer of non-circular wires. They will be flattened though without the sharp corners as depicted in figure 8a.



(a) Schematic cross-section of chosen wire rope DB2K



(b) 3D impression of chosen wire rope DB2K

Figure 8: The DB2K wire rope



## 4 Selecting a Cause of Wire Rope Failure

There are many causes that can lead to the failure of a wire rope. Two obvious mechanisms are fatigue and plain overloading. Most of the times, however, there will be different mechanisms at play simultaneously. A cause of damage might be friction. The damage is the formation of a very thin layer of martensite which on its turn initiates a crack and thus accelerates fatigue.

An illustrative summary is given in [3], which is a wire rope inspection document provided by ALP industries, a wire rope producer. The examples range from corrosion to abrasion to crushing and more. Many of them are not relevant for the scope of this thesis, though two examples are shown in figure 9.

In figure 9a the wire rope has been damaged because it has been running over an undersized sheave. The damage caused has as a result prematurely initiated fatigue failure. In figure 9b corrosion has weakened the wires and as a result have broken prematurely, probably under a load that the wire rope was able to withstand otherwise.



(a) Fatigue failure initiated because the wire rope that ran over an undersized sheave.



(b) Wire breakages as a result of rust.

Figure 9: Examples of failing wire ropes.

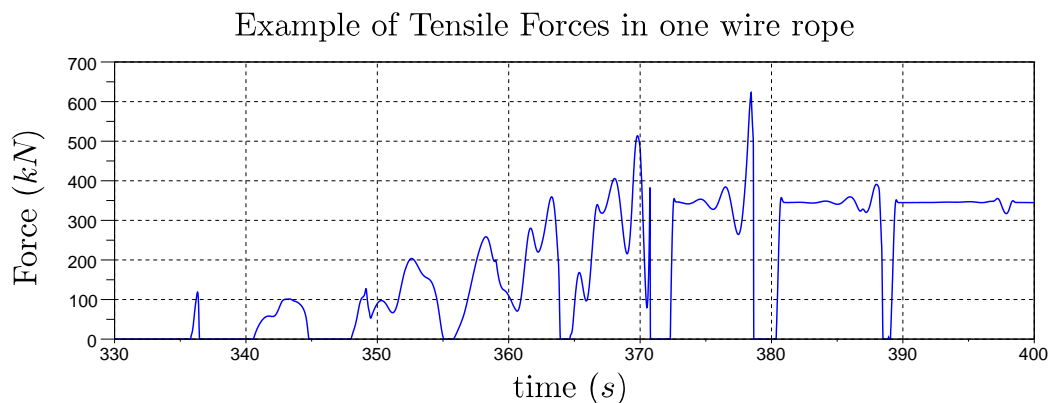
In this chapter a choice of potential causes of wire rope failure are presented. For each mechanism one or more available theories will be briefly discussed. *First* in section 4.1 *elastic waves* are investigated which can have *stress doubling* and/or *birdcaging* as a result. *Second*, in section 4.2, *hockling* can occur resulting from slack wire ropes caused by jacket rebounding on the seabed. *Third*, in section 4.3, the *internal heat generation* due to inter-wire friction is investigated. *Finally* in the *Conclusions* of this chapter, section 4.4, the following questions will be answered:

- Which mechanism, damage or failure, might cause premature failure in wire ropes caused by slack combined with tensile loads with shockload (like) characteristics that occur during the jacket decommissioning by the Pieter Schelte?
- What method is suitable to investigate the chosen mechanism

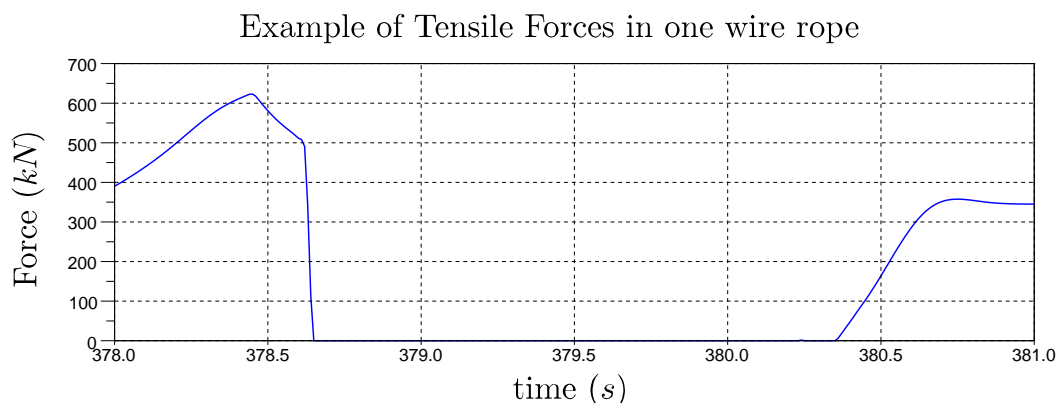
### 4.1 Elastic waves

It can be seen that the tension in the wire rope in- and decreases very 'suddenly' several times during the jacket decommissioning procedure. In section 2.1 an example of the tension in a hoisting cable is

shown in figure 2. Another example is shown here in figure 10a. Figure 10b zooms in on one of these 'sudden' in- and decreasing tensile loads. From the figure it is seen that the tensile load decreases from around  $500\text{ kN}$  to  $0\text{ kN}$  (slack) within  $0.05\text{ s}$  and then increases from slack to around  $350\text{ kN}$  in approximately  $0.4\text{ s}$ . Compare these values to the period of a typical wave,  $8 - 16\text{ s}$ , which in general is considered 'good working conditions' and it is clear that this de- and increase of tensile load is substantially fast. Wire rope producers recommend to avoid these characteristics. Throughout the jacket decommissioning, the decreases are on average ten times faster than the increases as seen in figure 10b.



(a) An example of the expected tensile loads in the hoisting wire ropes during jacket decommissioning.



(b) Zooming in on an example of a 'sudden' decrease followed by a 'sudden increase in tensile load in the hoisting wire ropes during jacket decommissioning by the PS.

Figure 10: An example of tensile loading on one wire rope during jacket decommissioning.

A known possible consequence of this type of loading characteristic are *elastic waves*. Elastic waves can be reflected at the end termination of the wire rope and interfere with each other causing *stress doubling*, section 4.1.1. They can also result in *birdcaging* when combined with built up torsional energy in the wire rope, section 4.1.2.

### 4.1.1 Stress Doubling

The wire rope to be used, figure 8, has a Minimum Braking Load (MBL) of  $4329kN$ . In [4] it is reasoned that the maximum allowed tensile force in the hoisting wire rope for jacket decommissioning is  $937kN$ . The reasoning is based on three safety considerations:

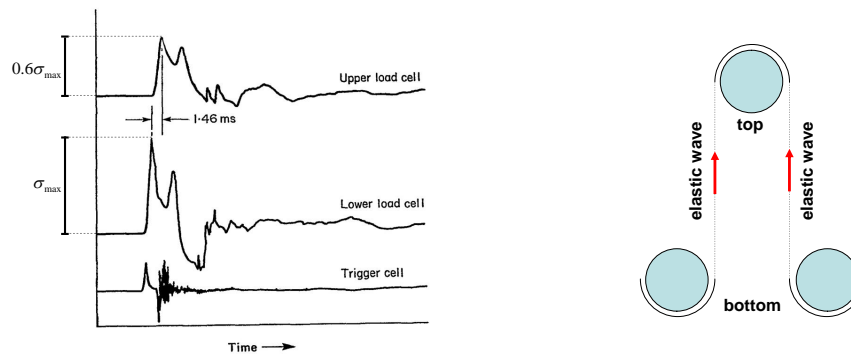
1. Difference in tensile force because the wire rope runs over several sheaves; a safety factor 1.09 is chosen.
2. Tensile force in wire rope to stay below 75% of the MBL with regards to elastic proportional limit of the wire rope.
3. Weight of hoisting equipment is not included in the ADAMS model of [4]; a safety factor of 1.06 is chosen.

According to the ADAMS model in [4], tensile force peaks of around  $600kN$  can be expected, see figure 10a. Thus if elastic waves cause stress doubling, the maximum allowed tensile force can be exceeded. For this to occur, two important influences on the severity of the elastic wave interference are:

- The energy conservation of the reflection of the elastic waves at the end termination.
- The resistance to elastic wave propagation in the wire rope, e.g., material damping and internal (inter-wire) friction.

In [21] a theoretical model is compared with experimental results also performed by the authors. To produce the impact load with resulting elastic waves, a weight is dropped onto the bottom end termination of the wire rope. This means that the tensile load in the experiment reaches its maximum significantly faster than the hoisting wire ropes considered for this thesis. Though not mentioned in [21], it can be expected that the time between zero and maximum tension will be a few orders smaller than the  $0.04s$  observed from the ADAMS model in [4].

In the experimental set up from [21], a wire rope is equipped with two load-cells that are placed  $3m$



(a) A plot of stress measurements performed in [21] where the distance between the upper and lower load cell is  $3m$ . The attenuation of the elastic waves over this length is significant, losing approximately 40% of its energy.

(b) Sketch of elastic waves occurring in different parts of the wire rope simultaneously.

Figure 11: Elastic wave attenuation (left) and simultaneous occurrence of elastic waves (right) in a wire rope.

apart from each other. This makes it possible to measure the propagation velocity as well as the attenuation of the elastic wave. The attenuation appears to be significant, see figure 11 a, over a length of  $3m$  the amplitude has decreased approximately 40%. The hoisting wire ropes are installed in a rigging block with 34 wire rope falls. From the upper rigging block the wire rope is led through the hollow TLB tips. The true end termination of the wire rope is the winch that is placed in the aft of the PS. Before elastic waves reach this end termination, they thus need to travel over several sheaves, followed by the length of the TLB tips and last through the wound-up part of the wire rope on the winch. Considering the length of the TLB tips,  $155m$ , and the distance between the top and bottom rigging blocks, approximately  $80 - 90m$ , the question is rather if the elastic waves will make it that far? Rather than whether how much of the elastic wave energy will be reflected.

Because the wire rope runs over several sheaves, elastic waves can be generated simultaneously in several places in the wire rope, see figure 11b. Even in this case the distance for the elastic waves to travel is significant, approximately  $80m$ .

Comparing the expected travel distances in the hoisting wire ropes with the distance travelled in the experimental set up in [21], it is clear that stress doubling is not likely to appear at all.

#### 4.1.2 Birdcaging

Impact loads result in tensile and torsional waves through the wire rope. When the loads are compressive (slack wire rope) or there is a 'sudden' drop in tension, helical wires and/or strands can separate from the inner layer(s). When this separation is *permanent* this phenomenon is called *birdcaging*, in the literature also referred to as *core protrusion*. See for an example figure 12.



Figure 12: Example of birdcaging a.k.a core protrusion.

If and how much separation occurs depends on the axial strain  $\epsilon$ , the rotational strain  $\beta$  and the velocity of the impacted end of the wire rope. In [7] a theory has been derived to determine when wire/strand separation occurs for SSR's and MSR's. The procedure is described briefly without going into mathematical detail.

*The first step* in this theory is to determine when the line contact forces are zero. These are the normal forces that act between adjacent wires/strands within a layer. When these forces are zero, the wires/strands are just touching. In the sign notation of the theory in [7], negative forces mean the

wires/strands are pressed against each other and positive forces mean they are moving away from each other and are thus separating. The following relation can be derived:

$$F_{line} = c_1\beta - c_2\epsilon \tag{1}$$

The line contact force  $F_{line}$  thus depends on the axial strain  $\epsilon$  and the rotational strain  $\beta$ . This line is drawn in figure 13. The constants  $c_1$  and  $c_2$  depend on the construction of the wire rope, e.g. lay-angle of the wires etc.

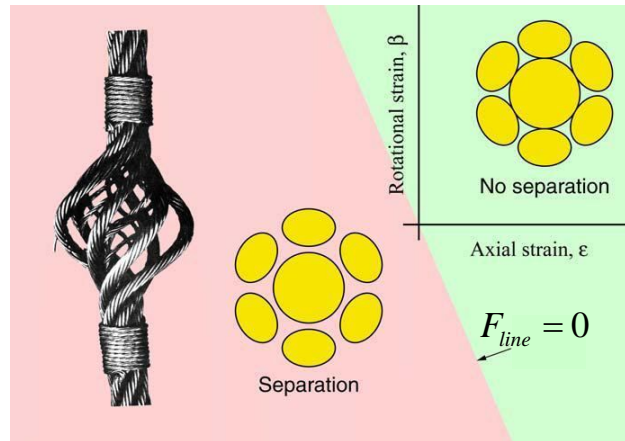


Figure 13: Picture of birdcaging and graph showing the border between separation and non-separation of outside wires/strands taken from [8].

The second step is to derive the linear differential equations of motion,  $f_1(x, t)$  and  $f_2(x, t)$ , describing the tensile and torsional motion for each point in the wire rope in the time domain. The excitations are the linear and angular displacements due to the variation of the tensile force  $F$  and torsion  $M$  (twisting moment). The origin of the reference frame for  $f_1(x, t)$  and  $f_2(x, t)$  is at the top of the wire rope that is hanging down. The linear boundary conditions, where  $u(x, t)$  is the linear displacement function, describe tensile load excitation at the bottom and the suspension at the top:

$$u(0, t) = 0 \quad , \text{and} \quad u(L, t) = u_{ext}(t) \tag{2}$$

The angular boundary conditions, where  $\phi(x, t)$  is the angular displacement function, describe non-rotating ends:

$$\phi(0, t) = 0 \quad , \text{and} \quad \phi(L, t) = 0 \tag{3}$$

the third step is to apply the Laplace transformation on  $f_1(x, t)$  and  $f_2(x, t)$  in combination with the above boundary conditions and a chosen impact displacement function  $u_{ext}(t)$ , e.g. a step impuls. This will yield the local strains  $\epsilon$  and  $\beta$  anywhere in the wire rope in the time-domain subjected to a sudden decrease in tension.

Now that the local strains are known together with the line showing where separation depending on the

strains begins, it is possible to determine whether birdcaging can occur, see figure 13. It can be seen that even with a positive strain, wire/strand separation can occur. It must be stressed that separation does not by definition lead to birdcaging.

The interested reader is referred to [7] for the mathematical details of the theory. An important note is that this theory is applicable to small axial strains only, of the order up to around  $5e^{-3}$  and that it is assumed that the helical wires/strands retain their shape. The allowable tensile stress in [4] yields a allowed maximum strain of  $3.5e^{-3}$  and is thus within the limits of this theory.

A dynamic model has been developed to investigate the velocity of the impacted end of the wire rope, see appendix D.1. The model consists eight *mass-spring-damper* elements. The velocities resulting from the tensile loads shown in figure 10a are plotted in figure 14. The impacted bottom end of the wire rope is represented by the blue line. The maximum velocity is seen to be around  $5m/s$ . In [7], an example impact velocity is mentioned of around  $7m/s$ . Even though a different wire rope is considered in [7], it implies that the expected velocity is in the order where Birdcaging might occur.

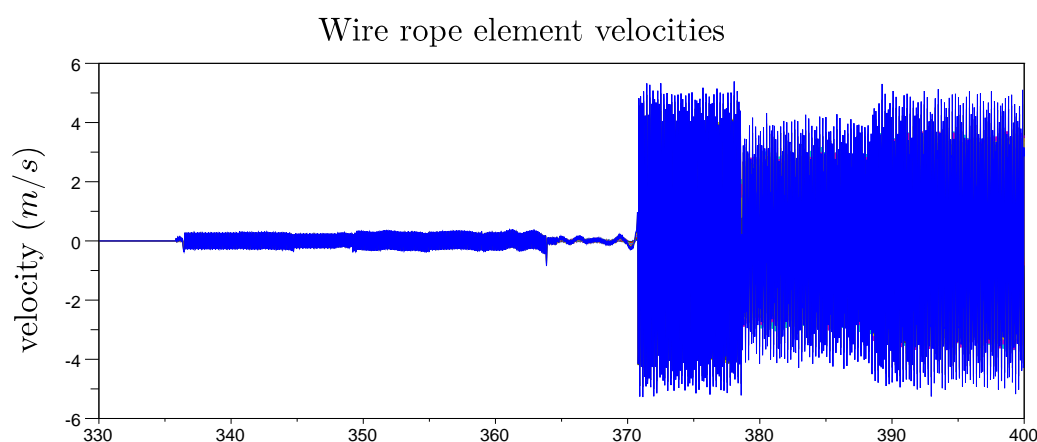


Figure 14: Velocities of wire rope elements subjected to a tensile load as shown in figure 10a.

## 4.2 Hockling

A *hockle* is a loop that forms in a wire rope. The hockling of a wire rope can only occur when it becomes sufficiently slack. What is 'sufficiently' depends on the torsional energy at the moment the wire rope becomes slack and on the bending and torsional stiffness of the wire rope. A sequence of the hockling process is shown in figure 15 taken from [16]. After the forming of a hockle, subsequently *snarling* can occur, see the right most picture of figure 15. It is the helical twisting of the wire rope starting at the contact point of the hockle where the wire rope crosses. The hockling itself is not damaging for the wire rope, though, when the tension in the wire rope increases and de-slackens and the hockle does not unwind, kinking will occur. This will seriously damage the wire rope making it useless for further safe use. Torsional energy can be built up in the wire rope basically in two ways:

1. When a payload hoisted or lowered by a wire rope whose ends are not permitted to rotate. The (uncontrolled) rotating of the payload will then cause twisting in the hoisting rope and will thus build up torsional energy.



2. Due to the (double) helical structure of wire ropes, torque increases in the wire rope even when it is loaded under pure tension resulting in torsional energy being stored in the wire rope.

Most theoretical research with respect to hocking has been aimed at developing stability criteria, e.g. [38], [35] and [9]. The results in these papers offer methods to determine criteria on which to base decisions with regards to safe use of wire ropes. In [15] a dynamic model in the time domain of hocking has been developed. For the jacket decommissioning by the PS, however, applicable proven and stability criteria are needed.

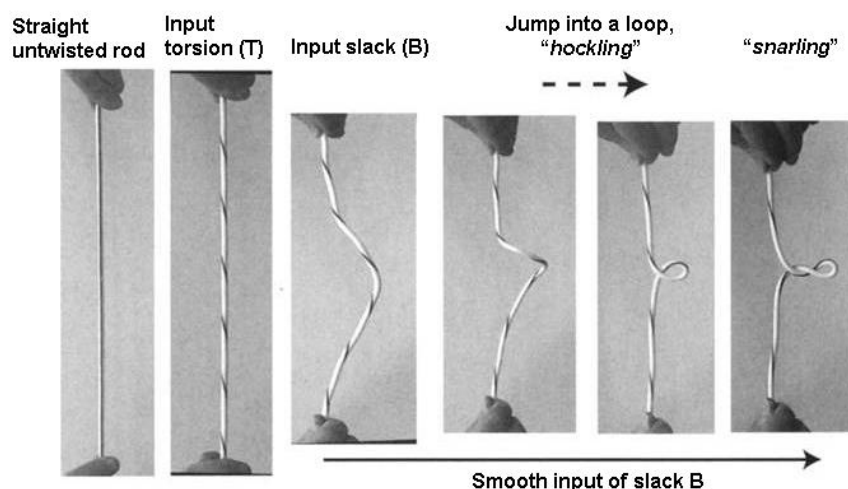


Figure 15: Sequence of loop forming of a rod, due to sufficient initial twist combined with sufficient slack, followed by snarling, taken from [16].

Within Allseas, too, research has been done, see [12], into hocking. The research was aimed at single- and multiple-rope systems and consisted of choosing stability criteria from available literature and performing experiments for verification. The research was motivated by the multi-rope 'Abandon&Recovery' system designed for the *Solitaire*, an Allseas pieplay vessel. Due to the systems' design it restricts untwisting unlike the single-rope system.

Stability criteria for hocking under two conditions have been investigated, *non-zero tension* and *zero tension*. Only the latter is considered here because this condition has been confirmed to occur (alternating taut-slack wire ropes) in [4] and [43].

Slack is defined as the difference between the initial unloaded cable length  $L$  and the length of the cable projected onto a line parallel to the direction of the load. The critical slack  $B$  is the amount of slack when hocking is expected to occur. Results from the tests done in [12] on the *double-rope* system have been compared to one of the available theoretical stability criteria developed for the zero-tension condition. This criterium relates relative critical slack  $\frac{B}{L}$  to amount of twists:

$$\frac{B}{L} = \frac{1}{2nN} \tag{4}$$

where  $N$  is the ratio between torsion and bending stiffness and  $n$  is the number of twists. The results of the tests with the double-rope system from [12] are shown in figure 16.

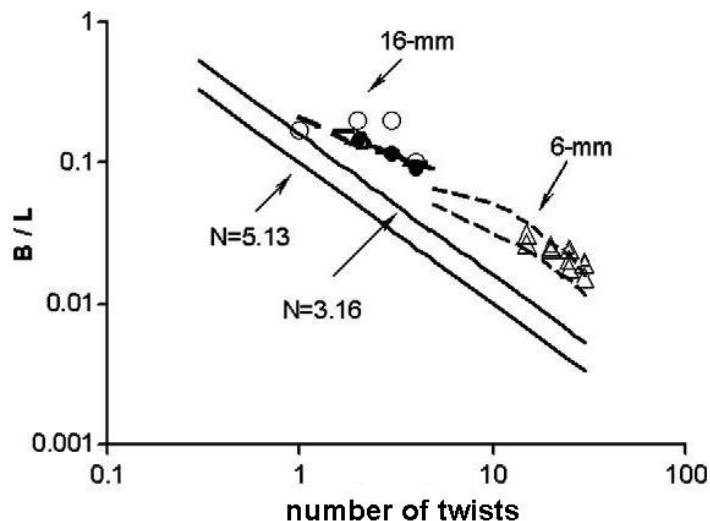


Figure 16: [12]: "Critical relative slack  $\frac{B}{L}$  for double-rope sets: 6-mm diameter hanging cables and 16 mm diameter cable on the ground. Solid lines give the theoretical prediction following equation 4. Marks correspond to test results."

What can be seen for all the tests is that hockling appeared with a larger number of twists than predicted by the theory. One of the important practical conclusions that is related to the jacket lifting procedure is:

*"...the criteria for one rope can be applied to multiple-rope systems."*

The results of the ADAMS model developed by [4] in the time domain can be used to determine the amount of slack and thus the critical amount of twists throughout the lifting procedure. A theoretical allowable maximum amount of twist can then be determined.

### 4.3 Internal Heat Generation

When a wire rope is subjected to an tensile, torsional or bending load, the wires will slide with respect to each other as a result of the deformation of the wire rope and their (double) helical construction. This will cause friction in the wire rope. A well known application of frictional energy is the process of making a fire in the woods with sticks, see e.g. [45]. It is thus clear that friction can lead to very high temperatures. But can high temperatures be achieved due to inter-wire friction in a wire rope?

Steel is known to conduct energy very fast. Most often the wires are made of non-alloy carbon steel. The thermal conductivity  $k$  of this steel is around  $50 \text{ W/mK}$ , compare this with wood, around  $0.2 \text{ W/mK}$  which can be held in your hand while the other end is burning. Therefore the frictional energy at the inter-wire contacts is expected to dissipate throughout the cross-section of the wire before having a significant effect on the material.

What is not known is how much friction energy can actually be expected inside a wire rope subjected to a loading as shown in figure 2, section 2.1. A few documents have been encountered that contain some clues that inter-wire friction can be significant, [36] and [2], or what the effects of a temperature rise can be [41] on wire ropes. They are described next.

### 4.3.1 Clues for excessive internal friction

**Premature failure of a hoisting wire rope in a mine** An analysis has been done on a hoisting wire rope that has been used at a mine in India. The wire rope failed prematurely and was handed over to the authors of [36] for investigation. The wire rope is a 25 mm diameter stranded wire rope. The operation and failure history given to the authors was almost nil. They applied the following tools in their research:

- Physical examination
- Mechanical test results
- Micro-examination of wires

Some interesting observations have been made. The *physical examination* clearly showed considerable plastic wear, though it was not believed that the ultimate failure was due to fatigue. This remark was motivated by the observation that the broken wires are of the 'cup and cone' type, see figure 17. The authors of [36] do not state whether the 'cup cone' type was found on every wire or not. This seems important information to discard the possibility of a premature break initiated due to fatigue, whether accelerated due to another mechanism or not. As stated in [41], a ductile wire diameter reduction of this type is generally associated with a tensile overload failure.

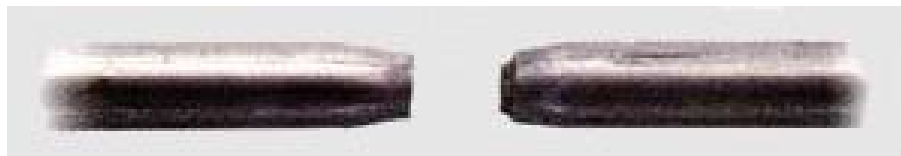


Figure 17: An example of a 'cup and cone' failure type.

It is also stressed that it does not mean that the cause of failure is due to an overload. The wire rope might have been weakened by another mechanism. Eventually the wire rope breaks and thus shows this type of break in the wires that have not been weakened. The tensile strength of the whole wire rope may have decreased due to, e.g. crushing in a sheave.

They were motivated by the *micro examination* of the failed examples. They noted that there were signs of plastic deformation normally observed with tensile failure. However, in their *mechanical examination* they found that strength loss due to deterioration was not appreciable and did not endanger safe operation.

The possible answer might be in the structure of the material. Originally, the material used had a pearlite structure, see figure 18a. It was observed that the structure had become martensite, see figure 18b at the surface of the worn out wires. This is possible when the material is rapidly cooled from an, minimum, elevated temperature. This process is called quenching and is used to obtain a certain material properties. The minimal elevated temperature is  $727^{\circ}C$ . These observations suggest that excessive frictional heat has occurred while the rope was in service. Pearlite is hard and tough where martensite is hard and brittle. When a small layer forms on the surface of the pearlite structure, martensite is susceptible to cracking and thus initiating/accelerating fatigue.

Even though they've made these observations they do not claim any single reason for the wire rope in

question to have failed. Nevertheless, it does motivate into looking into the heat generation caused by inter-wire friction.

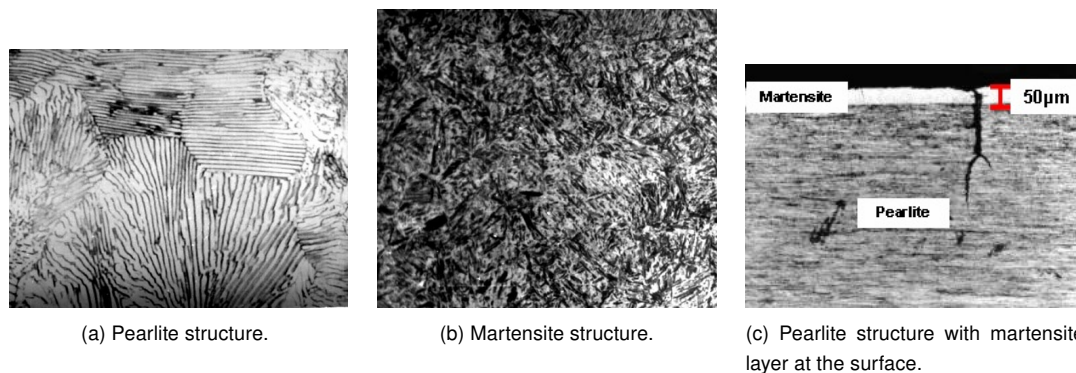


Figure 18: A pearlite structure is desired (left), it is hard and tough. The stripes are plates of Ferrite and Cementite. The martensite structure (right) has a needle like appearance and is hard and brittle. A layer of martensite that as formed at the surface of a wire and has resulted in crackforming.

**CASAR forensics on heat in wire ropes** Another hint to look into this direction is mentioned in [41]. These authors, too, mention that when the temperature within the rope exceeds a certain level, the material structure can change and thus also change its tensile strength. The temperature level they mention is even lower,  $300^{\circ}\text{C}$ , than the temperature mentioned in [36]. The cold drawn wires can then recrystallize losing two thirds of their tensile strength. They do not relate the material structure change to friction. What they do show is that a very small local layer of martensite can initiate fatigue cracks. The wire rope can then fail prematurely and potentially unexpectedly in case the significant fatigue cracks are not detected (expected) during wire rope services.

**Excessive friction in a heave compensation application** At a workshop about *heave compensation*, a presentation by Acergy [2] has been given about heat production in a wire rope while in service as part of a heave compensating system. It was about cyclic bending of a wire rope over sheaves which for many years has been known to have internal broken wires. Sometimes this has led to catastrophic failures.

To gain understanding in the failure process, they've built a test rig to carry out initial research on a large 109mm diameter wire rope. A clear conclusion they've drawn from these tests is: "It was clearly identified that the inherent rise in temperature increased the bending fatigue effect leading to rapid failure.". The conditions during the test were two meter waves and: "...represented good working conditions.". A series of tests was conducted with varying loads; 125, 175 and 225 ton. Each test had a duration of an hour. The maximum temperature measured was  $120^{\circ}\text{C}$ .

An important conclusion related to wire rope lubricant, is that they've found that it is best not to let the temperature rise above  $50^{\circ}\text{C}$ . From this point the temperature level has been found to increase rapidly.

Even though bending cycles are known to generate more friction than tensile cycles, this presentation is a hint that the same effect might be significant in the case of the jacket decommissioning. The

taut-slack situation with the rapid tension in- and decreases is far from being an equivalent of 'good working conditions'.

### 4.3.2 On inter-wire friction

It is known that there is inter-wire friction within a wire rope subjected to tensile, torsion and/or bending loads. Friction is the phenomenon of two materials being pressed against each other. When the two materials start to slide with respect to each other, the normal force and friction coefficient  $\mu$  result in a friction force directed opposite to the sliding direction, see figure 19a. There are two types of inter-wire friction at play within a wire rope:

1. Line contact between adjacent wires *within* a wire layer, figure 19a
2. Trellis contact between two wires crossing from *different* wire layer, figure 19b

A trellis contact has a normal force acting on an ellips shaped contact area with semi-major axis  $a$  and semi minor axis  $b$ , where the line contact is a surface load on the contact area with width  $b$  along the length of adjacent wires. The trellis contact has been found to be an important mechanism for fatigue [30] and line contact sliding has a significant greater effect on specific energy dissipation than the trellis contacts do, [26].

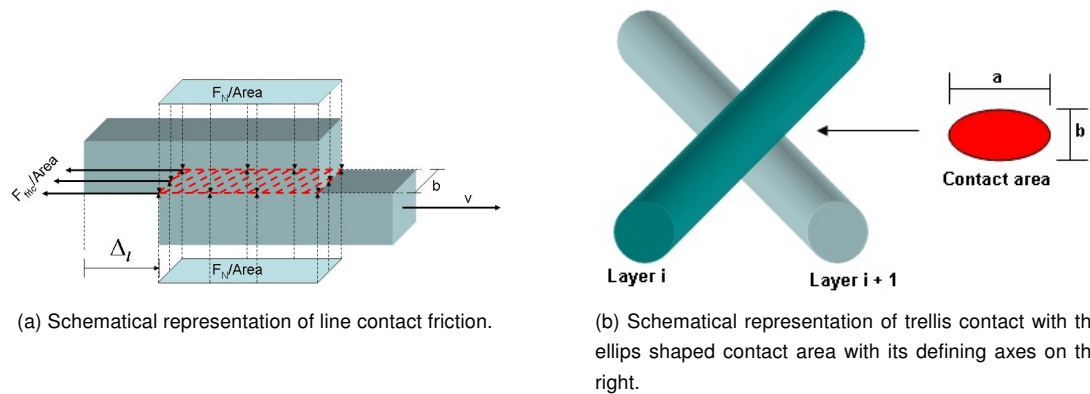


Figure 19: Schematical representation of line contact (right) and trellis contact (left).

So to determine the internal wire rope friction, methods need to be found and/or developed to determine for each time step; the normal line contact force  $F_N$ , the relative slip  $\Delta l$  between two adjacent wires within a wire layer and the line/trellis contact surface.

Summarized, what is needed is a theory that can evaluate the following for each timestep:

- Line and trellis contact forces.
- Sliding distance for the line and trellis contacts.
- Contact surface of the line and trellis contacts.

### 4.3.3 Models on wire ropes for internal heat generation

**Theoretical models** Above, it is summarized what needs to be determined to model internal frictional energy generation in a wire rope under tensile load. It is noted that preference goes out to a theory that has some verifications with experiments because experiments are not only expensive, they are also very time consuming.

Only a few notable theories have been developed on the subject of wire ropes. One is developed by *GA Costello*. He has also written a book on the subject, *Theory of Wire Rope* [7], referred to earlier in section 4.1.2. The theory is based on first describing the equations of equilibrium of a thin wire shaped as a helical spring. This provides the base for a collection of helical springs (thus strand) to describe the deformations of a strand under axial and bending loads. This base is then used to describe the static response of a strand, e.g. under pure bending but also stresses are determined of a strand passing over a sheave. An important assumption made is:

*The friction between the individual wires is neglected and are thus assumed to move collectively when the wire rope is subjected to a tensile strain.*

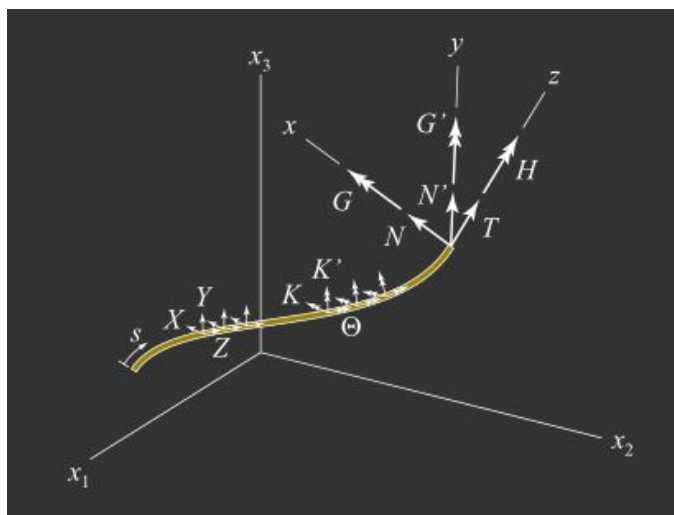


Figure 20: The force equilibrium of a thin helical wire which forms the base of Costello's [7] wire rope theory and also for the theories developed by M. Raoof.

But is this valid for the case of the lifting phase considered in this thesis? Furthermore the loads described in the book are static.

The above assumption in Costello's theory is addressed in [26]. Herein it is stated that only when the tensile load perturbations are relatively small compared to the mean tensile load, up to approximately  $\frac{\text{Load Perturbation}}{\text{Mean Load}} = 0.02$ , the inter-wire friction is negligible. The author of [26], *M Raoof*, has developed *The Orthotropic Sheet Theory* (OST). This theory goes into more detail with respect to inter-wire friction. It is based on the equilibrium equations developed by Costello, see figure 20, but deviates in describing the deformation of a strand under tensile, torsion and/or bending loads.

When larger load perturbations are applied to the wire rope it is found that inter-wire friction *does* play a significant role with regards to fatigue and wire rope dynamics. The latter can have a significant

influence on the behavior of the total system that the wire rope is part of. It is clear that for the case of the expected loading characteristics for the hoisting wire ropes of the PS, the load perturbations can be considered large. An example of the specific energy dissipation due to inter-wire friction for steady state cyclic loading is shown in figure 21.

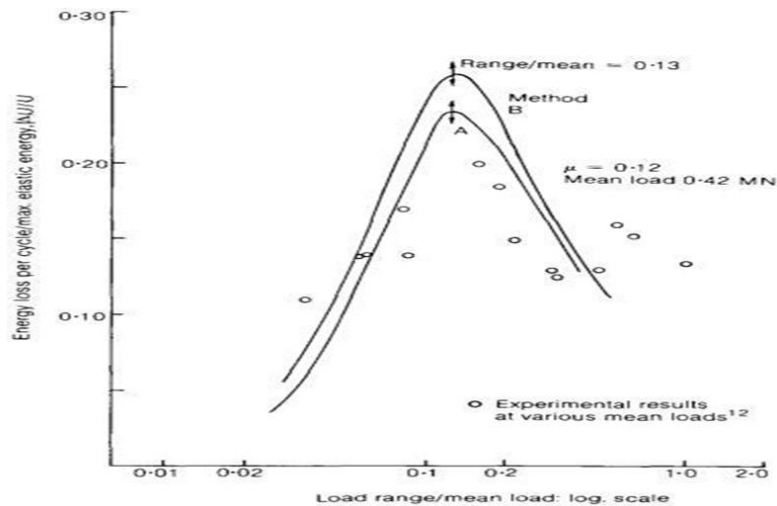


Figure 21: Examples of specific heat dissipation derived theoretically with the OST developed by M. Raouf taken from [24].

Examining figure 21 shows that the theory is far from predicting the specific energy dissipation near to the exact. One obvious reason for this is that the friction factor  $\mu$  of steel on steel is assumed to be constant, where in reality  $\mu$  will differ along the length of the wire rope. However, it does predict the scale and trend of the energy dissipation and thus is a proxy for confidence with regards to predicting line contact forces, contact areas and inter-wire slippages. A note to be made, stated by the author himself, is that the theory is especially suited for multi layered strands. And, like Costello's theory for birdcaging in section 4.1.2, the theory is applicable for strains up to  $5e^{-3}$ . It is repeated here that according to the allowable stress in [4], the maximum allowable strain is  $3.5e^{-3}$  and thus complies with the strain limit of the OST.

Summarizing, GA Costello's work, e.g. [7] and [8], does not take inter-wire slippage into account. Though it has provided a base for M Raouf to develop his *Orthotropic Sheet Theory*. The OST does take inter-wire slippage, and many more details, into account and is thus suited for the investigation of frictional energy generation within a wire rope.

### FEM models

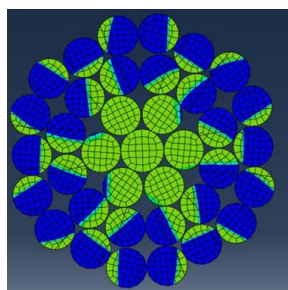
Due to development of computing power (*Moore's law*: "Computing power doubles every two years."), calculation time by FEM packages has been reducing dramatically. This development motivates the use of a FEM approach. This approach is described in e.g. [37], [19], [20] and [18].

As it turns out, even though computing power has increased, solving a FEM can still take significant time. In [37] the simulation time is mentioned of two wire rope models, 21hours and 70hours. The first model consists 11240 elements with 256623 nodes and the second model consists 152347 elements

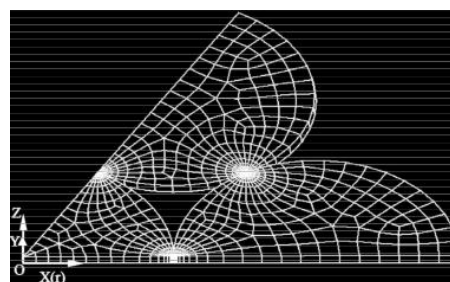
with 342947 nodes. In figure 22a it can be seen that the element resolution within a wire is still quite coarse. The element resolution applied will not suffice to investigate contact deformations and the associated contact stresses and inter-wire slippage in detail. Though it is mentioned in [37] that inter-wire contact and friction has been taken into account, no further details about the exact implementation are shown.

The various FEM models, however, are reported to have a fairly good agreement with experiments with respect to wire rope stiffness. Bear in mind though that there are several closed form solutions, e.g. [7], [23], [14] etc., that yield the same results.

An example with a higher and better chosen element resolution is shown in [19]. It focuses on contact stresses and inter-wire slippages under tensile and torsion loads. Their approach becomes clear by looking at figure 22b. The element resolution increases near the point of interest, the inter-wire contact. Their results have good agreement with *Costello's* theory mentioned earlier with respect to tensile and torsional stiffness. Interesting in this example are the contact stresses. It seems that good use is made of the advantages of FEM techniques because insight is gained on the more detailed inter-wire interactions.



(a) Cross-section of a FEM taken from [37].



(b) Finite element mesh from [19].

Figure 22: Examples of FEM approaches.

Another, novel, approach is demonstrated in [22]. Instead of applying existing FEM techniques, the authors have developed a *p-version* finite element software. It takes into account friction, contact deformation and inter-wire slippage amongst others. The contact forces are the line contact forces of the first (most inner) layer of wires on to the core wire and the contact forces of crossing wires from the second layer onto the first layer. The inter-wire contact forces *within* one layer are *not* considered. This approach does significantly reduce computing time. It is not mentioned by how much.

Summarizing, FEM approaches still demand a lot of computing time, especially when details like friction, contact forces and inter-wire slippages are taken into account. They have been shown, however, to have generally good agreement with regards to wire rope stiffness.

#### 4.4 Conclusions

As shown in section 4.1, although the increase and decrease of the loading can be relatively fast, the loading does not have any significant *elastic waves* as a result. Moreover, the distance travelled before interfering is too large,  $\gg 1m$ . Thus *stress doubling* will not be a potential problem.



Figure 14 in section 4.1.2 shows velocities that are in the same order as a numerical example in [7]. *Birdcaging* might thus occur. Further investigation is needed with the theory developed in [7].

Due to the expected amount of slack, hockling might be expected to happen during the jacket decommissioning. However, criteria on which to base decisions with respect to wire rope choice and hoisting procedure are shown to be available within Allseas, [12].

The loading will have more inter-wire friction as result compared to a 'normal' loading that has a steady state form. Some clues, in e.g. [41] and [36], have been found pointing to friction and the effects of a rise in temperature,  $> 300^{\circ}C$ , within the wire ropes. The frictional energy can have material structure changes as a result, pearlite to martensite, that might decrease the life of a wire rope or even cause sudden failure of the wire rope during the jacket decommissioning.

Summarizing, *stress doubling* is not expected to occur and available techniques are at hand to determine the potential occurrence of both *birdcaging* and *hockling*. The subject that needs more investigation is *frictional energy generation* and the resulting temperature rise, thus:

- More insight is needed into frictional energy generation within wire ropes with respect to heat dissipation and resulting potentially significant temperature changes of the wire rope material.

The FEM approach appears to still take up too much computing time, e.g. 21hours in [37]. The theoretical model of Costello neglects friction, where the *Orthotropic Sheet Theory (OST)* accommodates for more details. Not only does this theory yield the needed information, it also provides more insight into and understanding of wire rope behavior.

- It is chosen to apply the Orthotropic Sheet Theory (OST) to determine the frictional energy generated in a wire rope subjected to cyclic and non-cyclic axial loading.



## 5 Implementing the Orthotropic Sheet Theory (OST)

The OST is chosen as described in section 4. *First*, the basics of this theory are explained in section 5.1. *Second*, being then introduced to basics of the OST, it is explained in section 5.2 how the specific energy dissipation  $\psi = \frac{\Delta U}{V}$  and the Young's modulus  $E$  can be determined for a SSR and MSR. *Third*, in section 5.3 the results are shown of the implementation of the OST for SSR's and MSR's. *Fourth*, the conclusions are presented in section 5.4.

For the implementation of the OST a program is written. It is named the *Thesis Program (TP)*.

In this chapter and in appendix B the assumptions that underly this theory are explained. A summary of these assumption is presented here.

List of assumptions from section 5

- During deformation, twisting and bending of individual wires is negligible and thus wires carry only pure tension.
- Plane sections remain plane and thus the theory is applicable only remote from clamps.
- Centre line of wire forms a helix both before and after deformation.
- When considering a large number of wires in a layer,  $> 6$ , and small lay-angles,  $< 40$ , the cross-section of a cylinder under an angle can be reasonably approached as an ellipsis.
- The influence of the transverse contraction is assumed negligible for the derivation of the wire slippage  $\beta$  in the presence of a rigid core.
- The helical strands are approached as being straight.
- Strand tensile load is uniform over the whole strand cross-section because the lay-angles in different layers are very similar.

List of assumptions from appendix B

- Centre line of wire forms a helix both before and after deformation.
- In the unloaded situation the wires within the layer are just touching each other.
- The cross-section of the thin wires is an ellipse.
- The influence of the transverse contraction is assumed negligible for the derivation of the wire slippage  $\beta$  in the presence of a rigid core.
- A single layer on a rigid core is considered.
- Wires carry only pure tension.

Assumptions from [23], pagenumbers refer to paper-pages:

- Pure axial loading.
- Centre line of wire forms a helix both before and after deformation. P79
- All the wires are the same length and the plane sections remain plane which is at least reasonable for sections remote from the ends of the strand/rope. P79

- In normal rope construction, the lay-angles in different layers are very similar and the assumption of a uniform Faxial over the whole cross-section is a reasonable one. P82
- Changes in lay-angle  $\alpha$  and radius  $r$  are very small. P82
- $F_N$  and  $F_R$  are of the same order of magnitude. P82
- The shear strain  $S'_6$  is zero. P88

Important remark in [23]:

- "However, in a more realistic random loading situation it is reasonable to expect rather higher values for energy dissipation.", P91

## 5.1 Basics of the OST

In this section the basics of the *Orthotropic Sheet Theory* are explained. It has been developed for a multilayered strand. Here it will not be shown what the exact derivations are of the mathematical relations describing tensile deformation of a strand. Only the assumptions and reasonings that the derivations are based on will be presented. The mathematics can be found in appendix B. The notation for the strain tensor compliances differ from conventional notation. On the left of the following equation is the notation as used in the papers of M. Raoof where on the right the conventional notation is shown:

$$\begin{bmatrix} S_1 \\ S_2 \\ S_6 \end{bmatrix} = \begin{bmatrix} S_{11} & S_{12} & 0 \\ S_{12} & S_{22} & 0 \\ 0 & 0 & S_{66} \end{bmatrix} \begin{bmatrix} T_1 \\ T_2 \\ T_6 \end{bmatrix} \equiv \begin{bmatrix} \epsilon_x \\ \epsilon_y \\ \gamma_{xy} \end{bmatrix} = \begin{bmatrix} \epsilon_{11} & \epsilon_{12} & 0 \\ \epsilon_{21} & \epsilon_{22} & 0 \\ 0 & 0 & \epsilon_{33} \end{bmatrix} \begin{bmatrix} \sigma_x \\ \sigma_y \\ \tau_{xy} \end{bmatrix} \quad (5)$$

### 5.1.1 Orthotropic Tensor

A tensor describes linear relationships between vectors and scalars. Here the tensor is a strain tensor. It represents the relation between the forces per unit surface, and the coordinates of the normal directions of the surfaces for which those forces are considered. The resulting strains are a measure of deformation where a distinction is made between *normal strains* and *shear strains*. Normal strains are coupled with a change in volume where shear strains are not. The latter are coupled with a change in angle between two initially normal planes.

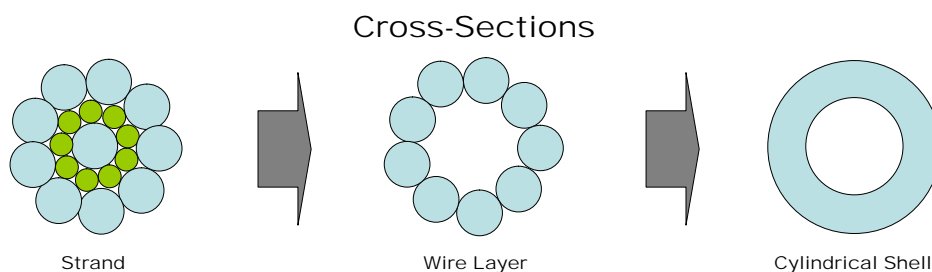


Figure 23: The basic approach of the OST is to first analyse each wire layer separately. Each wire layer is approached as a cylindrical shell.

Two strain tensors are defined for the OST. *First*, a strain tensor is defined that describes the deformations of a wire layer. Each wire layer is approached as a cylindrical shell, see figure 23, and is then analyzed. Once all wire layers have been analyzed, the strand properties can be determined. The wire layer is allowed to experience tensile ( $S_1$ ) and diametral (hoop) strain ( $S_2$ ). Hoop strain is in the circumferential direction. The wire layer has a lay angle  $\alpha$  with respect to the axial axis of the strand, whereof the wire layer is part of. When the strands experience tensile strain, the wire layer will, too, experience tensile strain. But because the wire layer has an angle  $\alpha$  with respect to the strand tensile strain, shearn strain ( $S_6$ ) will also occur. The shear strain will translate into slippage between the adjacent wires within this wire layer. In figure 24 the strains and the inter-wire slippage is depicted.

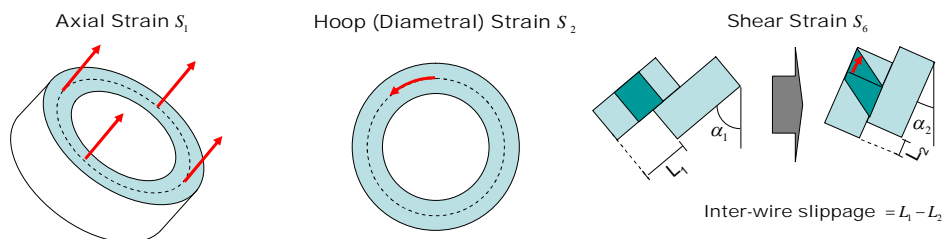


Figure 24: Illustrations of the strains in a cylindrical shell as defined for the OST.

When a material is said to be *isotropic*, its material property tensor (Hooke's tensor) relating stress to strain is invariant under coordinate transformation. In other words, the material behaves the same in all directions. From figure 24 it can be seen that a wire layer behaves different in each direction and is thus *anisotropic*.

An *orthotropic tensor (OT)* is a special case of anisotropy. It has at least two orthogonal planes of symmetry, see figure 25.

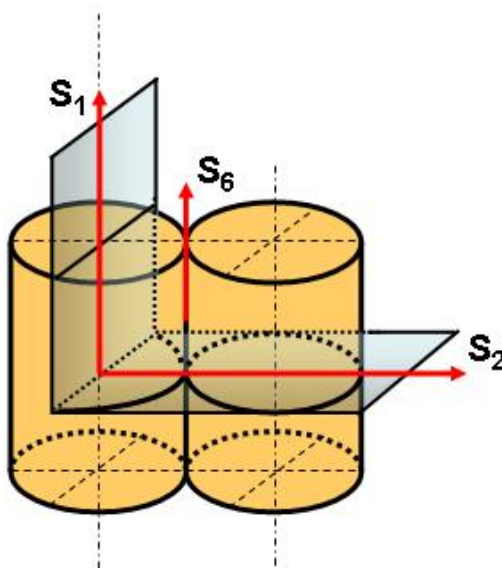


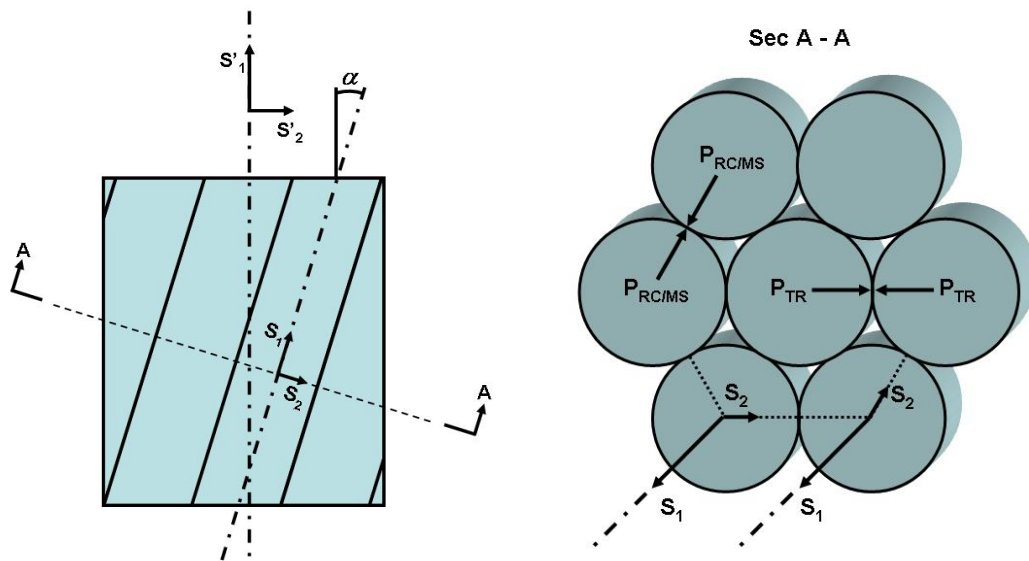
Figure 25: Symmetry planes of the of the orthotropic tensor of a wire layer.

The orthotropic tensor to be used within a wire layer,  $OT_{wl}$ , is two-dimensional and contains the

compliances based on a cylindrical shell. The determination of the compliances is based on the inter-wire interactions within this shell. The third dimension, in the strand radial direction, is assumed to be negligible and the wire is approached as experiencing *plane strain*. There are thus two orthogonal and one shear strain.

The subscript 1 refers to the axis in the axial direction of the wire. The radial strain, subscript 2, is chosen to be in the direction of the strand circumferential direction, or from wire center to wire center. As will be shown in 5.1.3, this is to accommodate for the diametral defelection  $\delta_n$  due to the wires being pressed against each other as a result of strand strain  $S'_1$ .

The subscript 6 refers to the shear strain. The shear strain occurs because the lay-angle  $\alpha$  changes. A line orthogonal between the wire centers before deformation is not orthogonal after deformation and thus the wire center lines have sheared with respect to each other. The tangential shear strain is thus related to the inter-wire slippage of two adjacent wires.



(a) Side view of strand with the principal axes of wire strains,  $S_1$  and  $S_2$ , and of strand strains  $S'_1$  and  $S'_2$ .

(b) Cross-section of strand with therein drawn the wire axial and radial strains,  $S_1$  and  $S_2$  respectively, and the line and trellis contact forces,  $P_{RC/MS}$  and  $P_{TR}$  respectively.

Figure 26: Side view (left) and cross-section (right) of a strand.

As each wire layer is evaluated, the strand radial direction is not taken into account in the tensor calculations within a wire layer. It is taken into account, however, when deriving kinematical relationships of the strand strains (axial  $S'_1$ , radial  $S'_2$  and torsional  $S'_6$ ), see figure 26a.

In the strand strain tensor, subscript 1 refers to the axial direction of the strand and subscript 2 refers to the radial direction. The subscript 6 refers to rotation around the strand axis,

$$\begin{bmatrix} S'_1 \\ S'_2 \\ S'_6 \end{bmatrix} = \begin{bmatrix} S'_{11} & S'_{12} & S'_{16} \\ S'_{12} & S'_{22} & S'_{26} \\ S'_{16} & S'_{26} & S'_{66} \end{bmatrix} \begin{bmatrix} T'_1 \\ T'_2 \\ T'_6 \end{bmatrix} \quad (6)$$

and, where  $x$  and  $y$  are the axial and radial strand direction respectively:

$$S'_1 = \epsilon_{x_{strand}} \quad , \text{and} \quad S'_2 = \epsilon_{y_{strand}} \quad (7)$$

Kinematical relations can be derived between the strand and wire-layer strains of a strand subjected to an axial strain  $S'_1$ . These relations are explained in section 5.1.2. The orthotropic compliances  $S'_{ij}$  are explained in section 5.1.4.

### 5.1.2 Kinematics in Wire-Layer Continuum subjected to a tensile Strand Strain

The change in geometry of a strand due to deformation can be described with a collection of eight equations. These are kinematical relations derived when the strand is subjected to an axial strain  $S'_1$ . All eight unknowns herein are depending, whether directly or indirectly, on the strand strain and the construction details of the wire layer being investigated. Here it will be described what these kinematical relations are based on. For the actual mathematics and derivations it is referred to appendix B.2

When a strand is stretched, the lay-angle  $\alpha$  of the wires will decrease. This change of lay-angle is accompanied with bending and twisting of the individual wires. However the following main assumptions in deriving this theory are [23]:

*During deformation, twisting and bending of individual wires is negligible and thus wires carry only pure tension.*

and:

*Plane sections remain plane and thus the theory is applicable only remote from clamps.*

During construction of the strand, it can be expected that the wires will deviate slightly from the helical geometry. Under axial stretch in the strand it is plausible to expect the wires to deviate even more from the ideal helix. This deviation is expected to be negligible, however, and therefore the following assumption is made:

*Centre line of wire forms a helix both before and after deformation.*

Two radial strand strains,  $S'_{2C}$  and  $S'_{2R}$ , are introduced. The strand strain  $S'_1$  results in a change in  $\alpha$  accompanied with a change in helix radius  $r$ . This change in helix radius determines the radial strains  $S'_{2C/2R}$  before and after deformation:

$$S'_{2C/2R} = \frac{r' - r}{r} \quad (8)$$

The difference between these radial strains is the reasoning behind the change in helix radius  $r$ . A relation between the strand tensile,  $S'_1$ , and radial,  $S'_{2C}$ , strain can be derived with the parametric

description of a helix:

$$x = r \cos \phi \tag{9a}$$

$$y = r \sin \phi \tag{9b}$$

$$z = r (\cot \alpha) \phi \tag{9c}$$

The situation of pure tensile strain is considered, thus:

*The ends of the wire rope are not permitted to rotate, thus  $\frac{\Delta\phi}{L} = 0$*

The radial strain  $S'_{2C}$  includes the effects of the rigid body movements of the wires due to a change of  $\alpha$  and contact patch deformation. The subscript  $C$  refers to a rigid core being present. The contact patches are the contact areas of wires being pressed against the next inner layer (Trellis Contact), see figure 19b in section 4.3.2. The contact patches can be included by making the assumption:

*For each wire layer a rigid core is present to derive  $S'_{2C}$ .*

The above mentioned rigid body movements of the wires do not contribute to line contact forces. The radial strain associated with these rigid body movements is denoted  $S'_{2R}$ . In determining the radial strain  $S'_{2R}$  the following assumption is made:

*When considering a large number of wires in a layer,  $> 6$ , and small lay-angles,  $< 40^{circ}$ , the cross-section of a cylinder under an angle can be reasonably approached as an ellips.*

In figure 27 it is visualized that the helix radius  $r$  shortens when the lay-angle  $\alpha$  becomes smaller. This radial strain is not directly related to the strand strain  $S'_1$ , only indirectly as the lay-angle changes due to the strand strain.

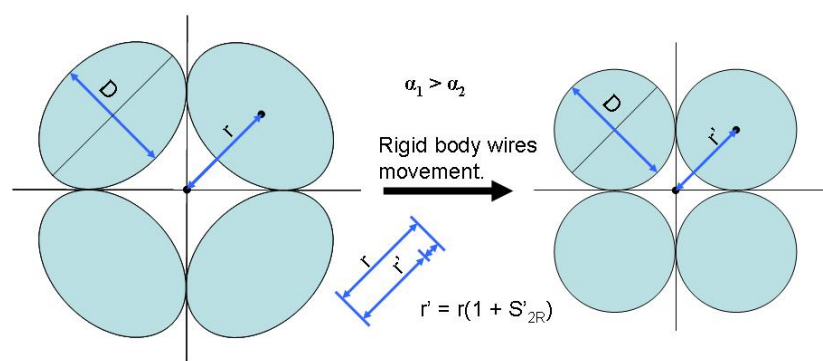


Figure 27: Change in helix radius due to change in lay-angle  $\alpha$  where the wires are treated as rigid bodies.

The strain  $S'_{2R}$  as a result of rigid body movements does not contribute to line-contact forces and



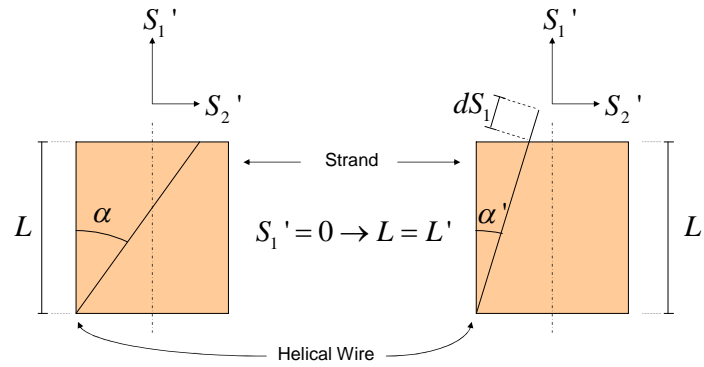


Figure 28: Illustration of  $dS_1$  as a result of strand tensile strain  $S_1'$  when  $S_1$  is kept zero and only the resulting lay-angle  $\alpha'$  after deformation is taken into account.

deformations and thus needs to be subtracted from  $S_{2C}'$  to yield the net radial strain:

$$S_2' = S_{2C}' - S_{2R}' \tag{10}$$

A change in lay-angle  $\alpha$ , with the associated strand tensile strain  $S_1'$  set to zero, results in a change in axial wire strain  $dS_1$ , see figure 28. In deriving wire slippage,  $\Delta_l$ ,  $dS_1$  must be subtracted from the total wire strain  $S_1$  and thus does *not* contribute to inter-wire slippage.

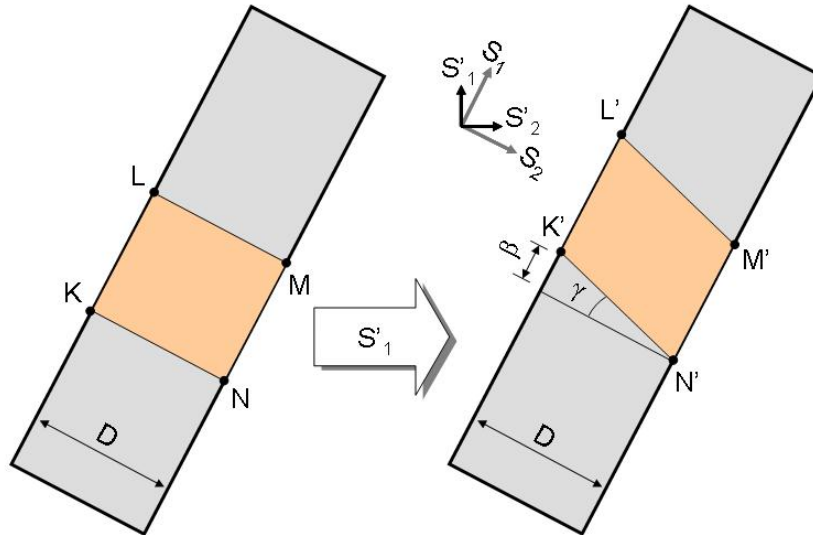


Figure 29: A sketch clarifying the determination of wire slippage between two adjacent helical wires.

Through lay-angle  $\alpha$ , two relations can be derived between; strand and wire tensile strain  $S_1'$  and  $S_1$ , and between the helix radius  $r'$  and the radial strain  $S_{2R}'$ . The latter relation can be substituted into a geometric relation, [6], that has been derived between the

tensile wire strain  $S_1$  and radial strand strain  $S_2$ . This is achieved by using the circumference of the circle with helix radius  $r$ . Setting the strand strain  $S'_1$  to zero will yield a relation whereof the wire tensile strain represents the strain that *would* occur due to the rigid body movements of the wires. When the lay-angle  $\alpha$  changes without strand strain  $S'_1$ , the wires thus have to axially contract. This strain is denoted as  $dS_1$  which will be subtracted from the total axial wire strain because it will *not* contribute to inter-wire slippage because all adjacent wires experience this same change.

With the relative wire movements known the inter-wire slip  $\beta$  can be derived. In figure 29 it is shown that there is only a diametral shear strain because the change in diameter is neglected and thus:

*The influence of the transverse contraction is assumed negligible for the derivation of the wire slippage  $\beta$  in the presence of a rigid core.*

In determining the tensorial shear strain  $S_{6T}$  the change in diameter is taken into account. The described relations derived between the strand construction details and an axial strain  $S'_1$  yields eight equations wherein there are eight unknowns. A solution can thus be found for these unknowns by simultaneously solving the set of equations. For more details about the derivation of each of the eight kinematical relationships it is referred to appendix B.2.

Because the equations are very non-linear, the *Newton-Raphson* method needs to be applied. How this method works and has been implemented is described in appendix E. The result yields:

$$S_1 \quad S_2 \quad S'_1 \quad S'_2 \quad S'_{2R} \quad S'_{2C} \quad S'_{6T} \quad \alpha'$$

### 5.1.3 Radial Load Transfer in Multi-Layered Strands

The inter-wire forces need to be determined first where each wire layer is treated as lying on a rigid core and there are no forces from outer layers. In every layer the line contact force  $P_{RC}$  can be calculated when the strand is subjected to an axial strain  $S'_1$ . The subscripts *RC* refer to the rigid core. The contact theory developed by *Hertz* is applied here. The formulas for two parallel cylinders are taken from a compilation [42] of this theory. These formulas show how diametral deflection  $\delta_n$ , line contact width  $b$  and line contact force  $P_{RC}$  relate to each other with the material properties Poisson's ratio  $\nu$ , Young's modulus  $E_{steel}$  and the wire diameters  $D_1$  and  $D_2$ , see figure 31.

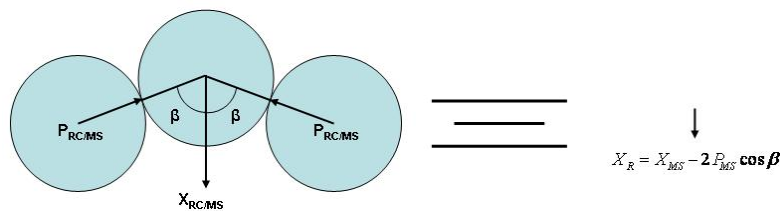


Figure 30: Forces,  $P_{RC/MS}$  and  $X_{RC/MS}$ , acting on the wire center (left) and the resultant force  $X_{R_i}$  (right) when the multilayered strand is considered.

The wires are indented at the contact surface and thus there is a change in distance between the adjacent wire centers, diametral deflection  $\delta_n$ . The diametral deflection  $\delta_n$  can also be derived with

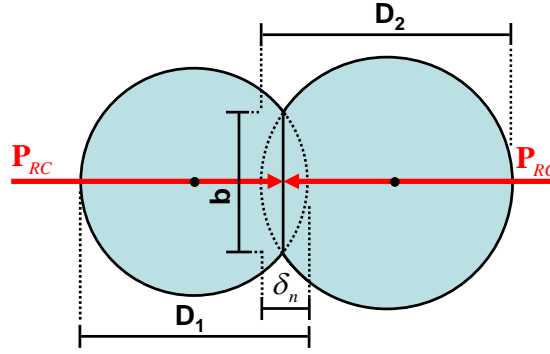


Figure 31: Cross-section of two wires in line-contact showing the diametral deflection  $\delta_n$  as a result of the line-contact force  $P_{RC}$ .

the diameters  $D_1$  and  $D_2$ , and the wire layer diametral strain  $S_2$ . The latter is a result of the solving of the eight kinematic relations as described in 5.1.2:

$$\delta_n = S_2 D \tag{11}$$

The width of the indentation is  $2b$ , [23], where it is noted that  $b$  is the full width of the indentation in [42]. Combining the Hertzian contact relations with equation 11 and writing for  $\delta_n$ , the following equation results where  $P_{RC}$  is the only unknown:

$$C_1 = \frac{4(1-\nu^2)}{\pi} \tag{12a}$$

$$C_2 = C_1 \left( \frac{1}{3} + \ln \left( \frac{1}{0.8\sqrt{2(1-\nu^2)}} \right) \right) \tag{12b}$$

$$\boxed{1.} \quad \delta_n = \frac{P_{RC}}{E_{steel}} \left( C_2 + C_1 \ln \left( \sqrt{\frac{E_{steel}(D_1 + D_2)}{P_{RC}}} \right) \right) \tag{12c}$$

Because of the helical form of the wires, when the strand is subjected to a tensile strain the wires straighten. When only one wire is considered this is possible but when a collection of wires is considered (strand) they restrict each others movement. This results in a force directed to the strand center, see figure 30, and is shown in [7] to be:

$$X_{RC} = \frac{EAS_1 \sin^2 \alpha}{r} \tag{13}$$

In [23] it is reasoned that each wire layer  $i$  has a  $\frac{P_{RC}}{X_{RC}}$  ratio for different mean tensile stresses  $T$ . The assumption here is:

*Strand tensile load is uniform over the whole strand cross-section because the lay-angles in different layers are very similar.*

With the  $P_{RC}$  and  $X_{RC}$  data known, their ratios within each wire layer  $i$  can be used to determine the line contact force,  $P_{MS}$ , and radial force,  $X_{MS}$ . The subscripts  $MS$  refer to the multi-layered strand.

The forces of all layers are taken into account in deriving these. In figure 30 the force equilibrium is shown. The resultant force  $X_{R_i}$  is the force acting upon the next (inner) layer  $i + 1$ . With  $X_{R_i}$  calculated, one can move into the next layer to determine  $X_{MS_{i+1}}$  and then use the  $\frac{P_{RC}}{X_{RC}}$  ratio to determine  $P_{MS}$ .

#### 5.1.4 Orthotropic Compliances

**OT of wire layer** The compliances  $S_{11}$  and  $S_{12}$  are according to Hooke's law. However, the net area  $A_{n,i}$  is the actual area of the cross-section of a wire layer normal to the direction  $S_1$  where the gross area  $A_{g,i}$  is the area of a cylindrical shell in that same direction. The gross area is approximated by summing the areas of squares with sides equal to the wire diameter. Both these compliances are thus multiplied by a factor  $\frac{A_{g,i}}{A_{n,i}} = \frac{4}{\pi}$ .

The compliance in the diametral direction,  $S_{22}$ , captures the change in deformation,  $\delta_n$ , of two cylinders in line contact under a normal force  $P_{line}$  with diameter  $D_1$  and  $D_2$ . Thus  $S_{22}$  is the resulting diametral strain. The compliance  $S_{22}$  can be derived by taking the derivative with respect to  $\frac{2P}{D_1+D_2}$ . So how much change wire center distance ( $D_1 + D_2$ ), and thus indentation, results from a change in line contact force  $P_{line}$ . This is then normalized over the wire centre distance to yield the diametral compliance:

$$S_{22} = \frac{2}{D_1 + D_2} \frac{d\delta_n}{d\left(\frac{2P}{D_1+D_2}\right)} \quad (14)$$

The compliance  $S_{66}$  is related to the inter-wire slippage. For details about the elaborate derivation it is referred to appendix B.

Recall now from section 5.1.2 that solving the kinematical relations yields amongst others the tensile and diametral wire strain  $S_1$  and  $S_2$  respectively. Thus with these strains and all compliances now known, the tensile and diametral wire stresses can be calculated,  $T_1$  and  $T_2$  respectively.

#### 5.1.5 Effective Young's Modulus of a strand

. The compliances of the OT of the wire layer can be transformed to the strand reference frame. This is done with Hearmon's notation [17]. The equations describing this transformation can be found in appendix B.6.

To derive the effective Young's modulus of a strand  $E_{eff}$ , the strand rotations around its axis  $S'_6$  are set to zero in equation 6. In the previous section 5.1.4 the wire tensile and diametral stresses  $T_1$  and  $T_2$  are derived. In [23] it is postulated that, where  $T'_1$  and  $T'_2$  are the strand tensile and hoop stresses:

$$\frac{T'_2}{T'_1} = \frac{T_2}{T_1} = K \quad (15)$$

The OT of the strand, equation 6, can then be solved to yield the relation for strand tensile strain and stress  $S'_1$  and  $T'_1$  respectively:

$$\frac{T'_1}{S'_1} = \left( S'_{11} + K S'_{12} - \frac{S'_{16}}{S'_{66}} (S'_{16} + K S'_{26}) \right)^{-1} \quad (16)$$

For each wire layer  $E_{eff}$  can then be derived. These are summed over all layers. Hereby the gross area  $A_{gross_i}$  of each wire layer  $i$  is used and the number of wires  $n_i$  in each layer. For mathematical details it is referred to appendix B.6.

The shear compliance  $S_{66}$  explained in section 5.1.4 depends on the wire slippage. It is infinite when  $\Delta_l > \Delta_{lmax}$ . Investigation leads to a value of 1 being relatively infinite. When  $S_{66}$  is infinite,  $E_{eff}$  remains fairly constant up to an allowable tensile strain of  $S'_1 = 5e^{-3}$ .

## 5.2 Implementation of the OST

The specific energy dissipation resulting from inter-wire friction for a strand can be determined for different load perturbations around a mean load by using the parts later described in this section.

### 5.2.1 Implementation for SSR's

The construction details of the strand and the material properties of steel are used to determine the Young's modulus of the strand,  $E_{strand}$  considering no inter-wire slip. Note that this will not be always necessary as rope producers might have determined this strand property. Also, it only has to be determined once for a range of axial strand strains and the information can be stored as a function of mean load.

Recall from section 5.1.5 that  $E_{strand}$  can be determine for the no- and full-slip case. The wire rope is stretched from the unloaded condition. When applying a mean load the wires will experience full-slip. The initial stretch is thus determined with the full-slip  $E_{strand}$ .

Furthermore, after an initial stretch,  $E_{strand}$  remains fairly constant. It is therefore expected that evaluating  $E_{strand}$  by taking its average after the initial stretch will be of sufficient accuracy to determine the mean strain.

The mean strain can then be used to determine the constant values to be used for tensile cyclic loading around a mean load. The initial values are the line contact force,  $P_{MS}$ , within each layer the normal compliance between the wires  $S_{22}$ , the stress tensile and diametral stress ratio of a wire, and the maximum wire slippage,  $\Delta_{lmax}$ . These are the values that are used to evaluate the energy dissipation of one load perturbation cycle.

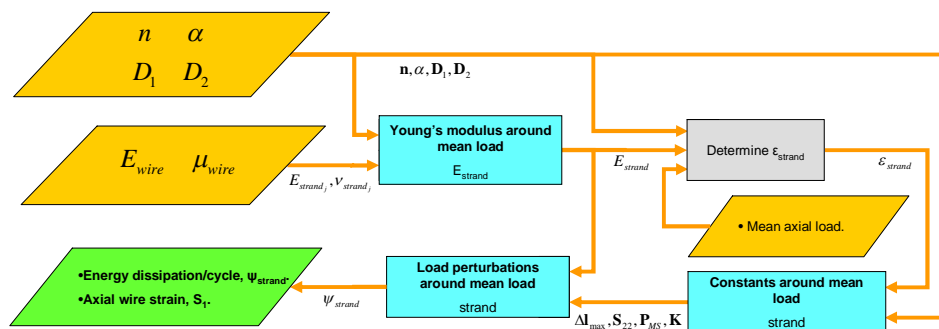


Figure 32: Flow chart for the energy dissipation  $\psi$  of a SSR.

The final step will yield the specific damping,  $\psi_{strand}$ , of the whole strand but also of each wire layer,

$\psi_{layer}$ , as a function of specific load perturbation. The energy dissipation is equal to the surface within the hysteresis loop, see figure 37. It is determined by methods developed in [10]. Therein a relation is derived between the aforementioned initial values and the friction factor  $\mu$ , the strand tension  $T'_1$  and the Poisson ratio. The indentation ( through Poisson's ratio) of the wires and the normal line contact and radial forces that are present are thus taken into account. The wire slippage  $\Delta_{l_{max}}$  indicates the transition from stick-slip to full-slip.

### 5.2.2 Implementation for MSR's

The OST needs to be developed for a MSR. Two approaches have been investigated:

1. Follow the theory analytically for double helices.
2. Treat the helical strands as wires and apply the existing OST theory. As the wire is actually a helical strand, apply existing theory again as if it is considering a straight strand, hereby ignoring the effect of the wires being actually double helices.

Once the OST theory has been understood and implemented for inter-wire friction in a single straight strand, it can be applied again the same way for determining the friction according to the first method. The axial stiffness is given by the wire rope producer for the entire wire rope, and not for the individual strands. Note that this is an essential property in determining the line contact forces. It will thus also be necessary to apply the OST to determine the stiffness of the individual strands.

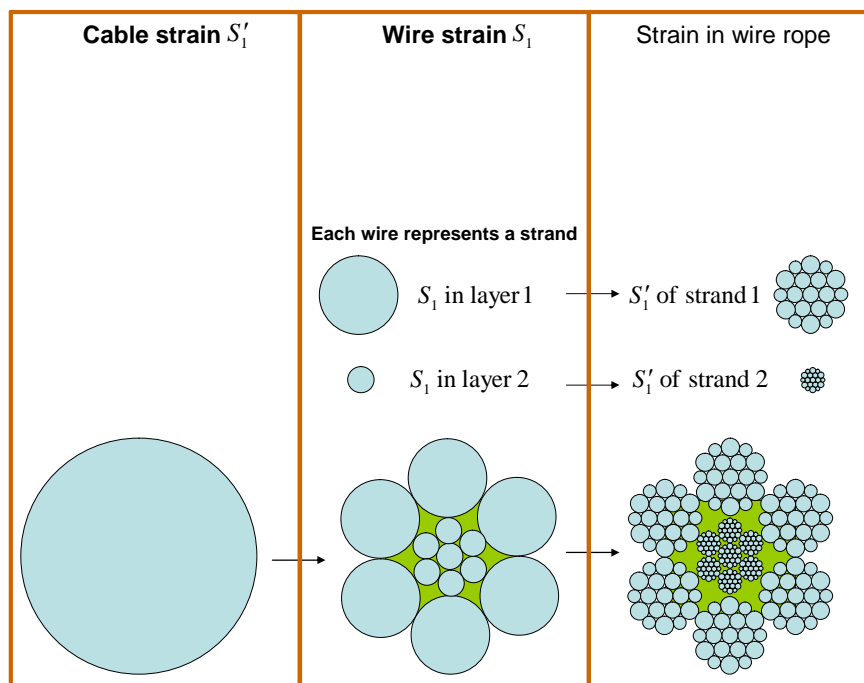


Figure 33: Schematical representation of approach 2 for applying the OST to MSR's.

The *first* approach is the same analytical route as is performed in [23] for SSR's. The parametric equations describing the double helix of a wire in a strand need to be derived. For the notation, it is referred to section A. To understand the following it is not needed to grasp the next equation 17. The z-coördinate as a function of the polar angle  $\phi_{11}$  is taken from equation 32 and given by:

$$z_0 = r_{11} \left( \frac{(\cot \alpha_{10})(\cot \alpha_{11})\phi_{11}}{\sqrt{1 + \cot \alpha_{10}}} - \sin \alpha_{10} \sin \phi_{11} \right) \quad (17)$$

A first step in deriving the theory is to determine the change in lay-angle  $\alpha_{11}$  due to the strain of the helical strand as a result of the applied load where the strand length  $L'_{strand}$  after deformation is given by:

$$L'_{strand} = L_{strand} (1 + \epsilon_{strand}) \quad (18)$$

As pure tension is considered the change in polar angle is zero thus  $\frac{\delta \phi}{\Delta}$ . Applying this to a double helix appears to be impossible analytically as this means that one needs to write equation 17 for the polar angle  $\phi_{11}$ .

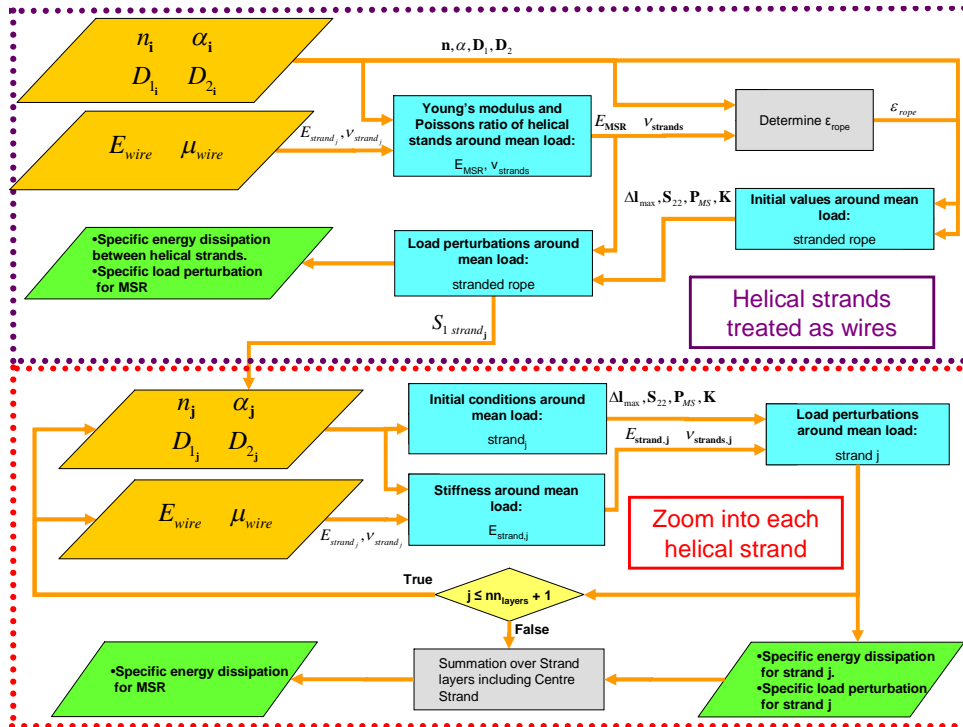


Figure 34: Flow chart for determining the energy dissipation  $\psi_{MSR} = \frac{\Delta U_{cycle}}{U_{cycle}}$  of a MSR depending on  $\frac{\text{Load Perturbation}}{\text{Mean Load}}$ .

The *second* approach is basically performing the OST twice. An important assumption for this approach is:

*The helical strands are approached as being straight.*

Approach 2 is possible. At small helical strand strains, in the order of  $5e-3$ , the effects of the bending of the helical strand will be expected to be negligible. Though this has not been investigated quantitatively, qualitatively it is fairly safe to state that the elongation of the strand approximates an infinitesimal part of the whole strand. At this scale the bending of the helical strand on the double helical wires is almost non-existent. This approach is chosen to be applied.

The procedure, in accordance with approach 2, to determine the specific energy dissipation for a multi-strand rope is shown in figure 34.

### 5.2.3 OST procedures

A blue block in the flowcharts of figures 32 and 33 hide another flowchart. These blocks show the details of the implementation of the OST. Next each block will be described and a flowchart shown for clarification. It is stressed here that the flowcharts shown are not designed on efficiency but more on clarifying the procedures to determine the various strand properties.

**Young's modulus around mean load**  
 $E_{strand}$

The no-slip Young's Modulus of a wire rope depends on the strand tensile strain  $S'_1$ , and thus the tensile load. The kinematic relations are solved for a chosen  $S'_1$ . The diametral strain  $S_{2i}$  of the wire layer is then used to determine the line contact force  $P_{RC_i}$ . The determination has not yet taken the multilayered construction of a strand into account. This is done by taking the resultant strand radial load  $X_{R_i}$  into account. The resulting line contact force  $P_{MS}$  can then be used to determine the diametral compliance of the strain tensor in the wire layer  $i$ . The compliance  $S_{66}$  depends on the wire slippage  $\Delta_l$ . Two situations are evaluated, the no-slip and full-slip. When the sliding of wires is in the full-slip regime,  $S_{66}$  is infinite. It has been found that taking a value 1 is relatively infinite. For the no slip regime  $\Delta_l = 0$ .

Recall from section 5.1.4 that the other compliances  $S_{11}$  and  $S_{12}$  remain constant for each strand tensile strain  $S'_1$  and solely depend on the wire material properties  $\nu$  and  $E_{steel}$ .

Now that the compliances of the wire layer strain tensor are known, the effective Young's Modulus  $E_{eff_i}$  can be evaluated for layer  $i$ .

When all wire layers have been analysed for  $E_{eff_i}$ , the results can be summed over all layers yielding  $E_{strand}$ .

**Constants around mean load**  
strand

Above the effective no- and full-slip Young's Modulus has been evaluated for a chosen strain  $S'_1$ . The results can be applied to determine the tensile strain of a strand subjected to given mean tensile load.

Before evaluating the specific damping around a mean load of a strand subjected to a cyclic tensile loading, initial values need to be determined for each wire layer  $i$ ;  $S_{22_i}$ ,  $P_{MS}$ ,  $\Delta_{l_{max}}$  and  $K_i$ . These initial values are found to remain fairly constant for perturbations around a mean load. In figure 36 it is shown that also the wire strain  $S_{1_i}$  is an output. The wire strain  $S_{1_i}$  is utilized for MSR's where first



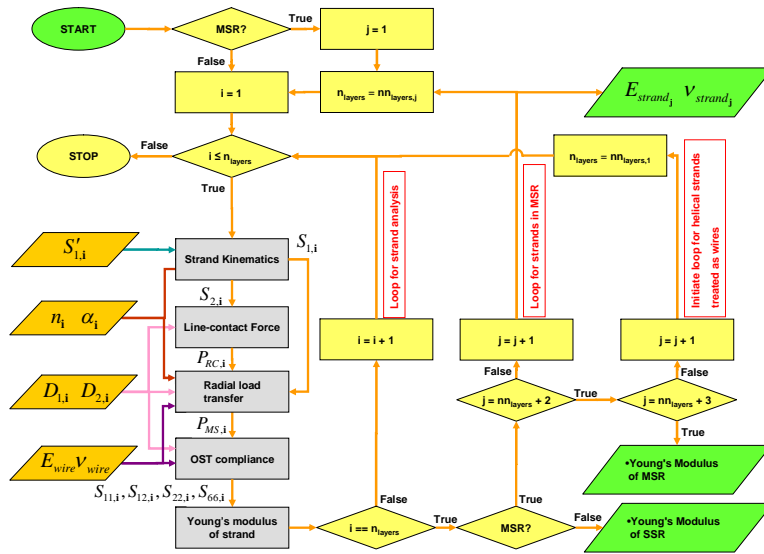


Figure 35: Flow chart for determining the effective Young's Modulus  $E_{eff}$  of a SSR depending on  $\frac{\text{Load Perturbation}}{\text{Mean Load}}$ .

helical strands are treated as wires.

The procedure to determine the initial values is very similar to the determination of  $E_{strand}$ . The difference lies in the end of the procedure. Instead of evaluating all OST compliances, only the compliance in the diametral direction of the OST,  $S_{22}$ , will be evaluated. The final desired initial value,  $\Delta_{lmax}$ , can therewith be determined.

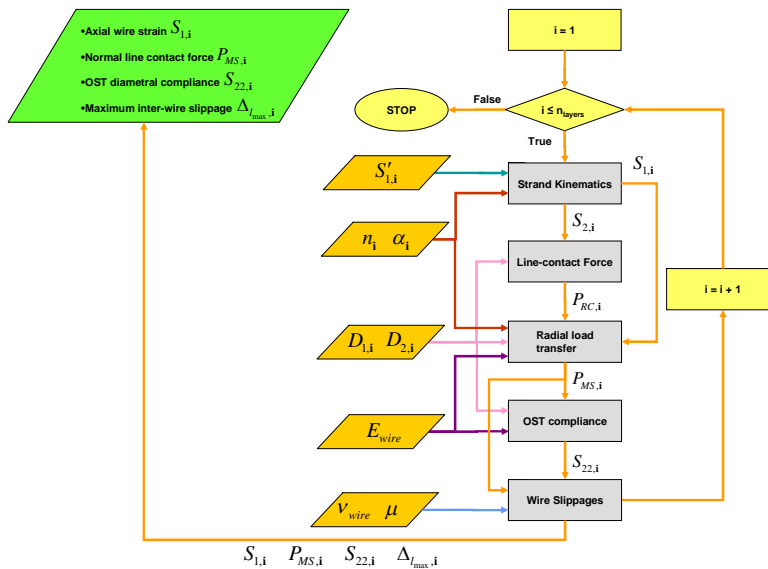


Figure 36: Flow chart for determining values of a strand kept constant around a mean load.

**Load perturbations around mean load strand**

The strand kinematics are again solved for each chosen strand perturbation. The resulting tensorial shear strain  $S_{6T}$  is used to determine the inter-wire slippage  $\Delta_l$ . The previously determined initial values  $S_{22i}$ ,  $P_{MSi}$ ,  $\Delta_{lmax_i}$  and  $K_i$  are used to determine  $E_{eff_i}$  and the specific damping  $\psi_i$ .

When all layers have been analysed, the results for each wire layer  $i$  are summed to finally yield  $\psi_{strand}$  and  $E_{strand}$  for each load perturbation around a mean load.

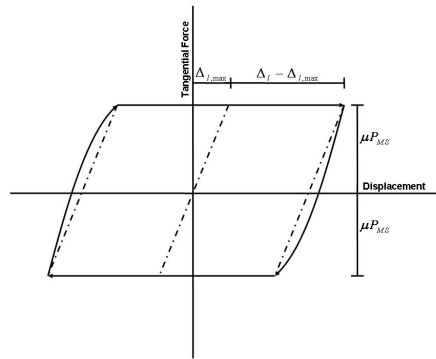


Figure 37: Hysteresis cycle of friction with stick-slip regime.

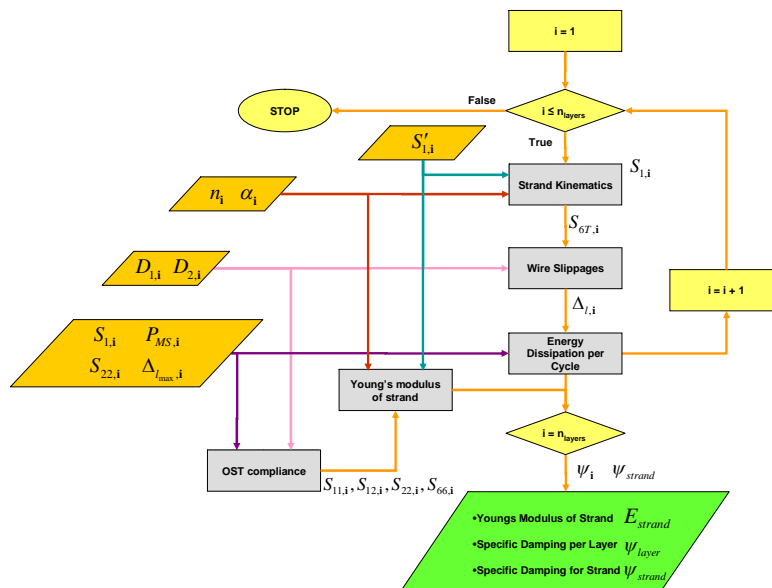


Figure 38: Flow chart for determining the energy dissipation  $\psi_{SSR} = \frac{\Delta U_{cycle}}{U_{cycle}}$  of a SSR depending on  $\frac{\text{Load Perturbation}}{\text{Mean Load}}$ .

### 5.2.4 Implementation for Dynamic Model for SSR's and MSR's

The OST has been developed for *cyclic* tensile loads. The tensile loads on the hoisting wire ropes of the PS, however, are *non-cyclic*, see figure 10a. It is thus difficult to reason a mean tensile load. The mean load is needed to implement the stick-slip behavior as is shown in section 5.2.1. Take e.g. the de- and increase shown in figure 10b. What can be seen as the mean load? Is it the mean of the previous oscillation? Is it the peak force considered divided by two? And for the increase, is it the slack situation, etc.? Basically, how can a mean load be reasoned on physics? And if the mean load is reasoned for different parts of the tensile loading, how can the reasoning be implemented?

It is decided that the stick-slip behavior is neglected for the non-cyclic dynamic implementation of the OST. Higher friction forces and thus energy dissipation will then result. The results are then upper limits of expected frictional energy. recall that for the cyclic implementation, the line contact forces  $P_{MS}$  are kept constant. In the dynamic model  $P_{MS}$  will be allowed to change for each time-step. This too, will result in higher frictional energy compared to the cyclic-implementation.

In figure 39 the flowchart is shown of the procedure for each time step. Whether the dynamic model is cyclic or non cyclic, the strand kinematics are solved followed by calculating the wire slippage  $\Delta_l$ . When the tensile load is cyclic, the friction forces in each layer are calculated based on the initial conditions that are kept constant;  $P_{MS_i}$ ,  $S_{22_i}$ ,  $b_i$  and  $\Delta_{l,max_i}$  for each wire layer  $i$ . The friction forces  $F_{fric_i}$  for each layer are then calculated according to the hysteretic behavior of the inter-wire slip. When the tensile load is non-cyclic,  $\Delta_{l,max}$  is not taken into account and is thus continuously in full-slip. The linecontact forces  $P_{MS_i}$  and associated contact width  $b_i$  are evaluated at each time step for each wire layer  $i$ .

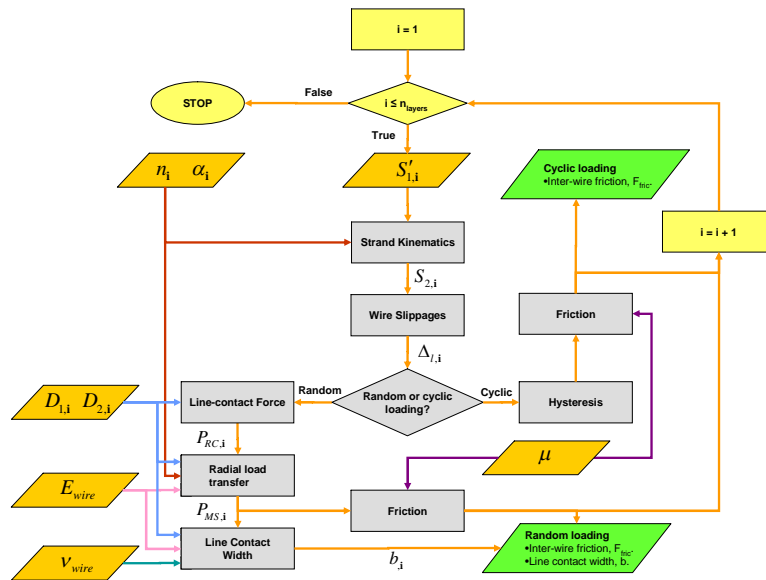


Figure 39: Flowchart of the implementation of the OST in a dynamic model where the hysteretic behavior is taken into account for a *cyclic* loading but not for *non-cyclic* loading. For the non-cyclic loading the slippage is continuously in the full-slip regime.

### 5.3 Results

In this section the results are shown for SSR's and MSR's. These result have been compared to examples provided in two papers of M.Raof, [23], [27], [29] and [25]. In the papers also numerical examples are provided of intermediate answers. For example a value of the tensorial shear strain  $S_{6T}$  is provided in [25] for a given  $S'_1$  of the  $39mm$  strand.

The comparison of results with these papers and also with a FEM model developed by [19] is described in appendix B.7. The main conclusion is:

*The implementation of the OST is performed satisfactory to determine the order of magnitude of temperature change within a wire rope subjected to tensile forces determined in [4].*

The two main results of the OST are the effective *Young's Modulus*  $E_{eff}$  and the *specific damping*  $\psi$ , both as a function of specific tensile load (or strain) perturbation. The construction details of the SSR and MSR are shown in table 3 and 4 respectively.

Layer	1	2	3	4	5	6
Number of Wires	30	24	18	12	7	1
Lay Angle ( $^{\circ}$ , +RH, -LH)	17.74	-16.45	-15.93	14.9	15.42	0
Wire Diameter (mm)	3.53	3.53	3.53	3.53	3.53	5.05
Mass (kg/m)	9.5					

Table 3: Construction details of a 39mm SSR taken from [26].

Layer		1	2	3	4
Wire Rope	Number of Strands	6	6	1	
	Lay Angle ( $^{\circ}$ , +RH, -LH)	17.92	18.19	0	
	Strand Diameter (mm)	12.78	5.13	5.62	
	Mass (kg/m)	9.5			
Strand Layer 1	Number of Wires	16	16	8	1
	Lay Angle ( $^{\circ}$ , +RH, -LH)	-18.29	-18.29	-18.29	0
	Wire Diameter (mm)	2.000	1.484	1.88	3.15
Strand Layer 2	Number of Wires	6	1	18	
	Lay Angle ( $^{\circ}$ , +RH, -LH)	14.88	0		
	Wire Diameter (mm)	1.68	2.000		
Core Strand	Number of Wires	6	1		
	Lay Angle ( $^{\circ}$ , +RH, -LH)	14.88	0	3	
	Wire Diameter (mm)	1.84	2.000		

Table 4: Construction details of a 40mm MSR taken from [29].

#### 5.3.1 Results for 39mm SSR

The results are shown for a  $39mm$  strand whereof the construction details are provided in [23].

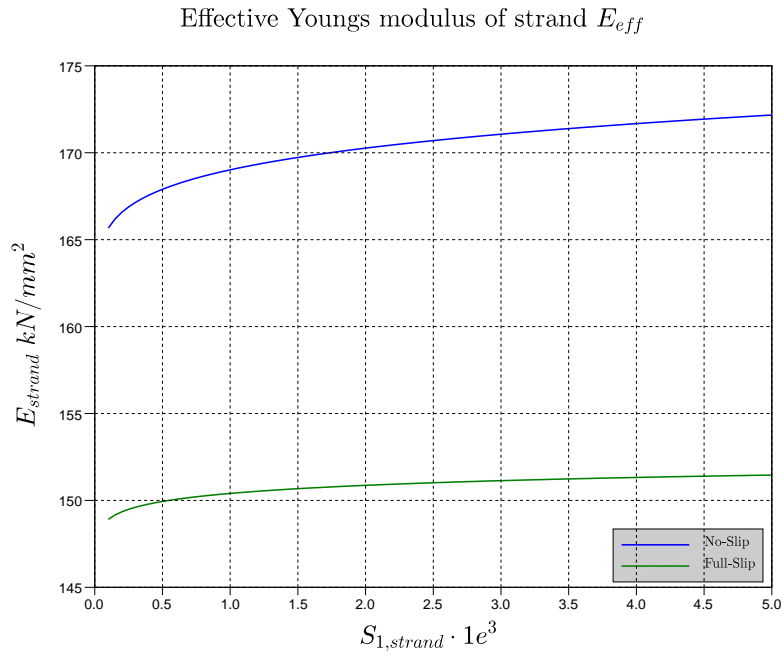


Figure 40: No-slip and full-slip effective Youngs' Modulus for the 39mm strand.

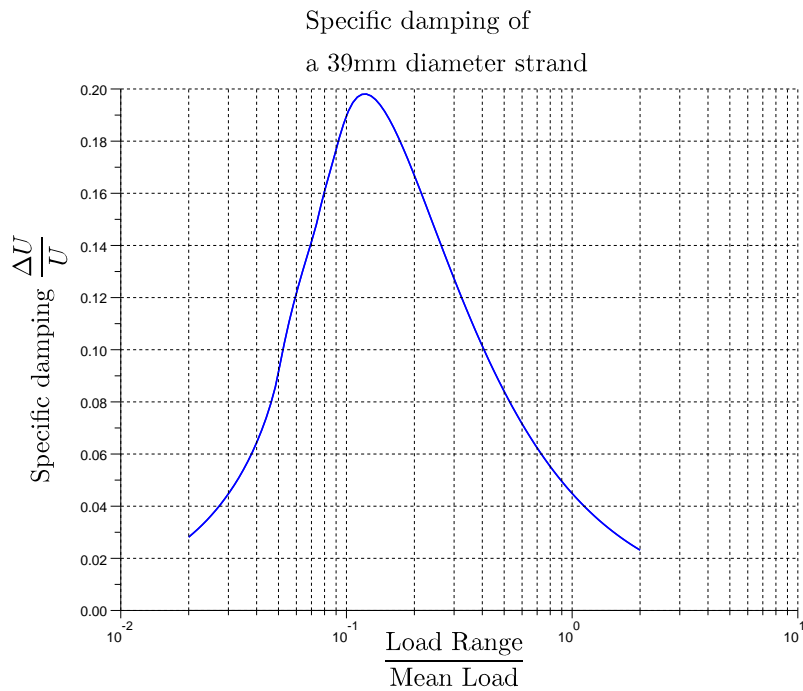


Figure 41: Specific damping  $\psi_{strand} = \frac{\Delta U}{U}$  for the 39mm strand. The mean load is 0.415MN

### 5.3.2 Results for 40mm MSR

The TP to implement the OST has been adapted for MSR's, as explained above in section 5.2.2. An important note is that the forces from one strand layer to another strand layer have, yet, not been taken into account. It is thus as if the strands are just touching each other, whether under tension or not. Results can now be produced for the MSR's treated as a strand, where the laid strands are treated as wires.

In [29], a similar approach as described in section 5.2.2 has been applied in determining the full-slip and no-slip Youngs Modulus of a MSR.

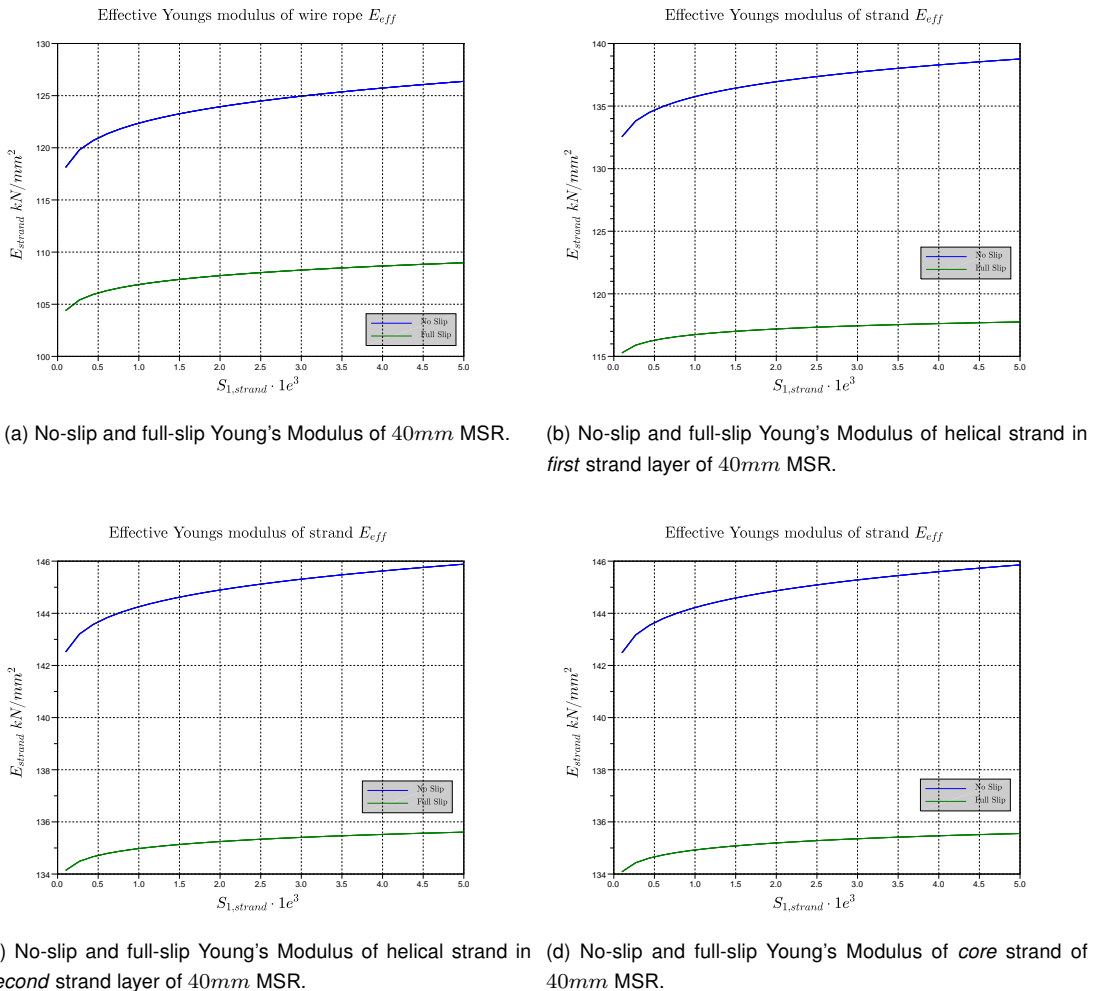


Figure 42: The no-slip and full slip Young's Moduli of 40mm MSR and its strands.

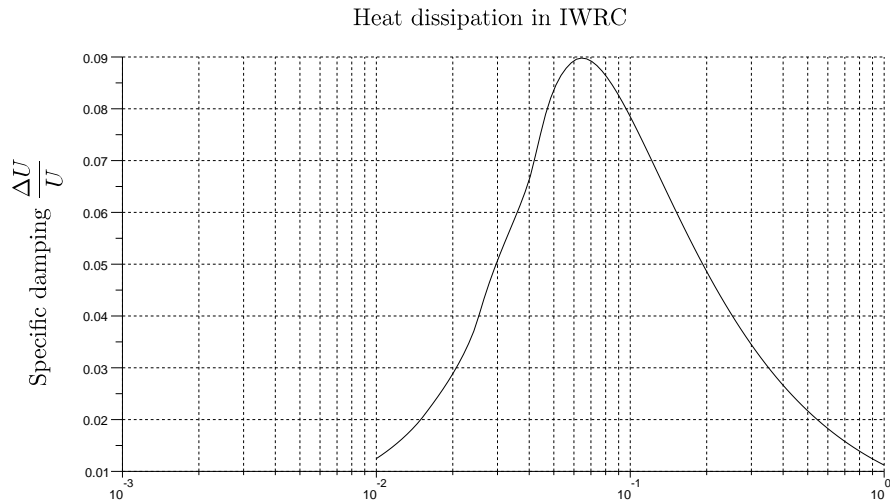


Figure 43: Specific damping  $\psi_{strand} = \frac{\Delta U}{U}$  for the 40mm IWRC. The mean load is 0.204MN.

## 5.4 Conclusions

In this chapter the OST has been understood and adapted twice, for MSR's and for the dynamic model (both for MSR's and SSR's). The following can be concluded:

- *OST successfully implemented for SSR's.*
- *OST successfully adapted and implemented for MSR's.*
- *OST adapted for implementation in cyclic and non-cyclic dynamic model.*





## 6 Frictional Energy Generation and resulting Temperature Changes

First, a dynamic multiscale FE<sup>2</sup> model is presented to determine the frictional energy generation in a wire rope subjected to a tensile loading. The tensile loadings applied have *cyclic* and *non-cyclic* characteristics. Second, the frictional energy determined by the multiscale FE<sup>2</sup> model is applied in a heat conduction model in 6.2 to determine the temperature change in the time domain in the cross-section of a wire.

### 6.1 Frictional Energy Generation

#### 6.1.1 Multiscale FE<sup>2</sup> Modeling

The amount of strain difference between the time steps influences the friction forces within the wire rope. To incorporate this effect into the dynamic model of the wire rope, friction needs to be evaluated for every time step. First, at each time step the strain is evaluated for each wire rope element (Macro Scale). Second, the resulting friction forces need to be determined for every wire rope element (Micro Scale). The model is thus evaluated at two different scales, hence the name *multiscale FE<sup>2</sup>*. Third, the results yielded by the micro scale model is fed back into the macro scale model. See figure 44 for an illustration of the method.

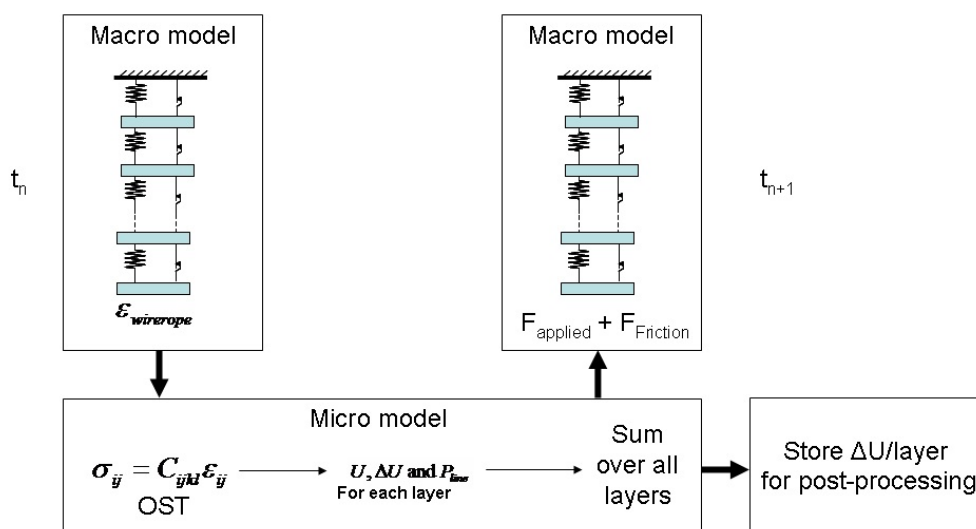


Figure 44: Schematic representation of multi-scale FE<sup>2</sup> modeling of a wire rope.

Friction forces between the wires counteract the strain direction of the wire rope. But the amount of strain difference (inter-wire slippage) also determines the friction forces. The non-linear variant of the numerical integration method *Newmark Method*, consists a convergence loop to deal with this. For every strain difference between two time steps, resulting friction forces can be evaluated. These friction forces are then substituted back into the dynamic equations and a residual force can be calculated. In case of an exact answer the residual will be zero. The convergence loop can be stopped when the

residual small enough. For each convergence the residual is compared to the a fraction of the total forces in the system.

The evaluation of the friction forces is computationally demanding compared to the time integration of the dynamic equations of the wire rope. A significant amount of time can be saved when these friction forces only have to be evaluated once. This is possible when the effect of the friction forces have a small influence on the dynamic response. In appendix D.2, a comparison is made between incorporating the evaluation of the friction forces in- and outside the convergence loop. It has been found that the influence on the dynamic response is negligible, thus:

*Evaluation of friction forces is kept outside the convergence loop of the numerical integration.*

The friction forces *do* have an effect on the dynamic response of the wire rope. If there is no friction, more internal wire rope vibrations will result compared to the same model *with* friction. These vibrations on their turn influence the frictional energy generation. It is also noted that the dynamic response of the overall system consisting the Jacket, Pieter Schelte etc, *is* negligible.

### 6.1.2 Wire Ropes used for Modeling

The construction details of the wire rope to be used (DB2K by Bridon) for the jacket (de)commissioning by the PS, see figure 8 in section 3.2.2, have not been made available. Several examples of wire ropes and their construction details, however, are presented in the papers by M Raouf. One *advantage* of using these examples for the following models is that intermediate results can be compared to examples from the papers by M. Raouf. One *disadvantage* is that it is not exactly clear what the exact influences are ... scaling etc. Two examples are applied, *first* a 39mm SSR and *second* a 40mm MSR. The construction details are presented in table 3 and 4.

It is desired that the resulting tensile strain in the wire ropes used for modeling results in the same tensile strain were the actual (DB2K) wire rope to be used. The Youngs Modulus times the area of the cross-section of the DB2K *is* available,  $E A_{DB2K} = 263MN$ . Note that the full-slip  $E_{eff}$  of the wire ropes is considered here. The following relation can be thus made with Hooke's law  $\sigma = \epsilon E$ :

$$\frac{\sigma_{example}}{E_{example}} = \frac{\sigma_{DB2K}}{E_{DB2K}} \quad (19)$$

An equivalent tensile force can now be derived:

$$\begin{aligned} F_{example} &= F_{DB2K} \frac{E_{example} A_{example}}{E_{DB2K} A_{DB2K}} \\ &= F_{DB2K} \cdot C \end{aligned} \quad (20)$$

The tensile loads calculated by the model of [4] thus have to be multiplied by the factor  $C$ . The Youngs Modulus  $E_{DB2K}$  is provided as a constant. In figures 40 and 42 it is observed that it is not a constant. It is also observed that beyond a tensile strain of  $1e^{-3}$  it does not change significantly. Even though the change in Youngs Modulus as a function of tensile strain *is* taken into account in the model, the coefficients  $C$  in equation 20 is evaluated once with the average  $E_{eff}$  of the wire rope examples from the papers by M. Raouf.

For the two different example wire ropes this yields;

$$\begin{aligned} C_{39mm} &= 0.571 \\ C_{40mm} &= 0.437 \end{aligned} \quad (21)$$

### 6.1.3 Cyclic Load

The Multiscale FE<sup>2</sup> technique is applied als for a cyclic load. The resulting energy dissipation per cycle is used to determine the specific damping  $\psi = \frac{\Delta U}{U}$ . The hysteresis loop differs in shape from the hysteresis loop described in [23]. The stick-slip phase is for the dynamic model linear, where it is non-linear as applied in [23]. The difference in energy dissipation, however, will be within a few %. It can thus be compared to the specific damping  $\psi$  as determined by the OST, section 5.2.1. It is the OST that has been verified with experiments, and therefore it is the energy dissipation yielded by the dynamic model that can be verified with results for the OST.

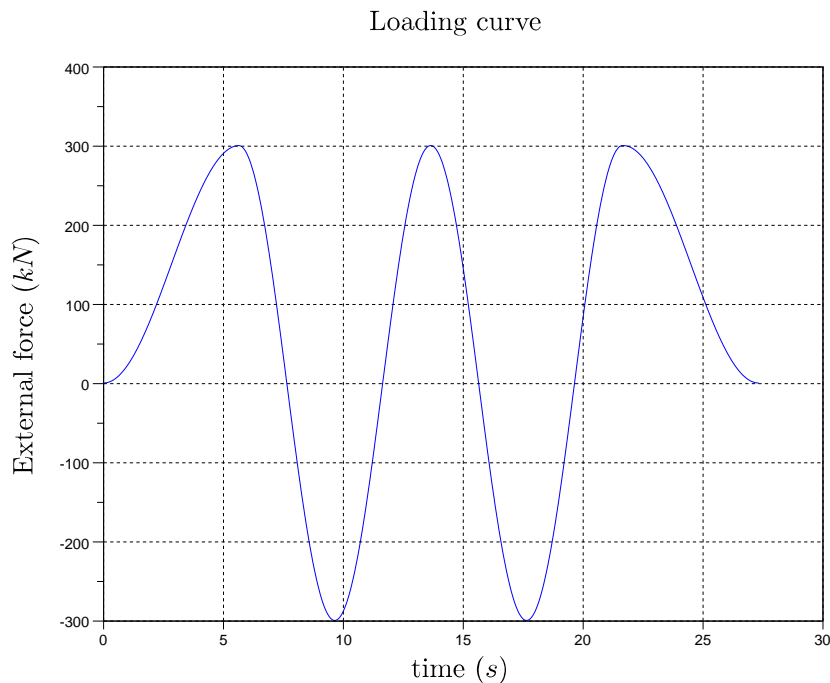


Figure 45: Cyclic axial load around a mean load applied

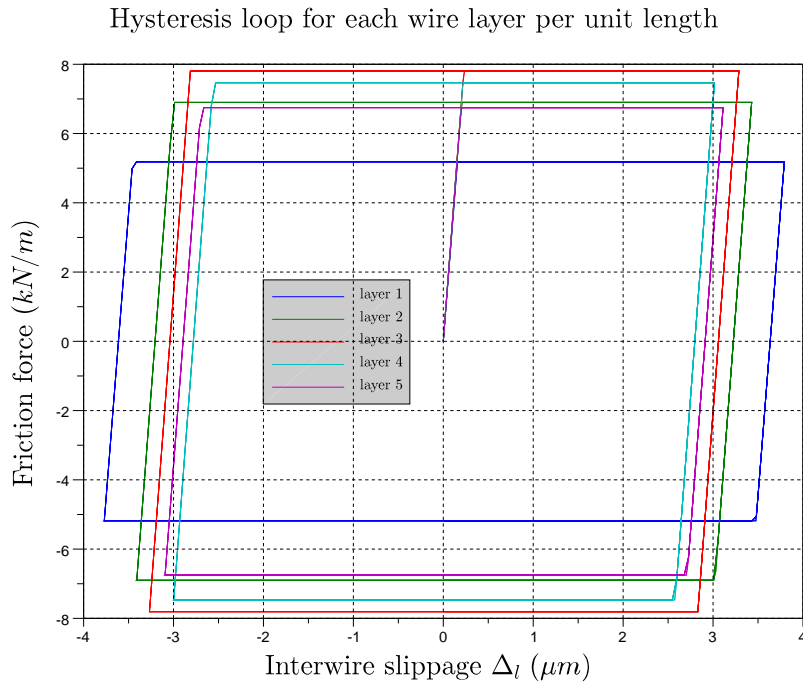


Figure 46: Hysteresis loop for the cyclic axial load shown in 45 around a mean load of 0.42MN

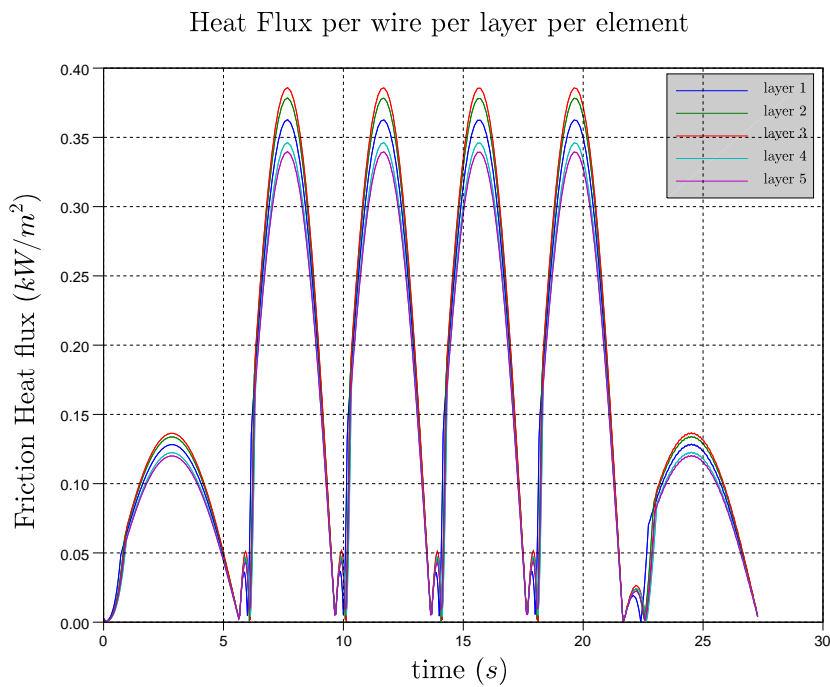


Figure 47: Heatflux (kW) in a wire layer of the bottom wire rope element resulting from the cyclic axial load shown in 45 around a mean load of 0.42MN

6.1.4 Non-Cyclic Load

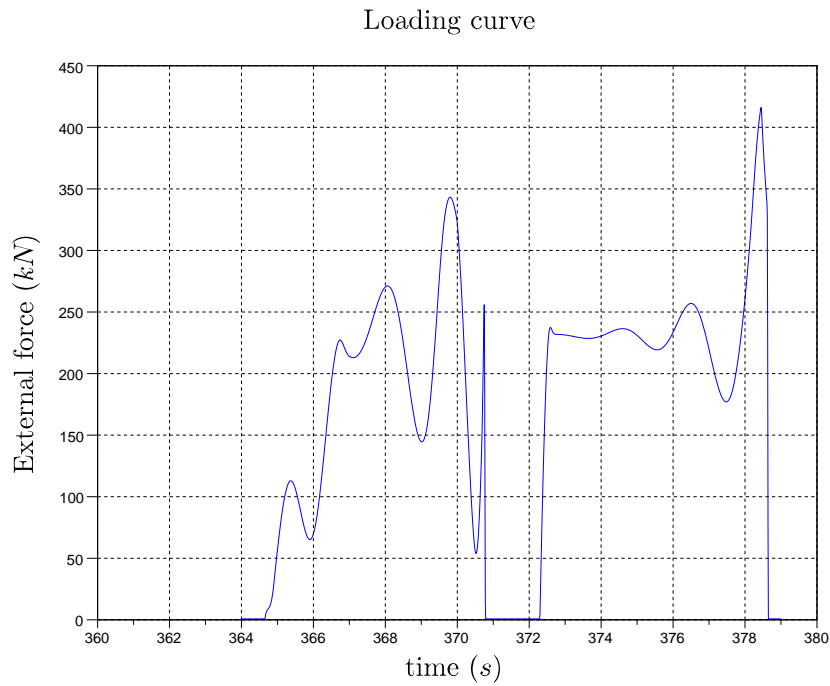


Figure 48: Random like axial loading occurring during Jacket decommissioning by the PS modeled in ADAMS by [4].

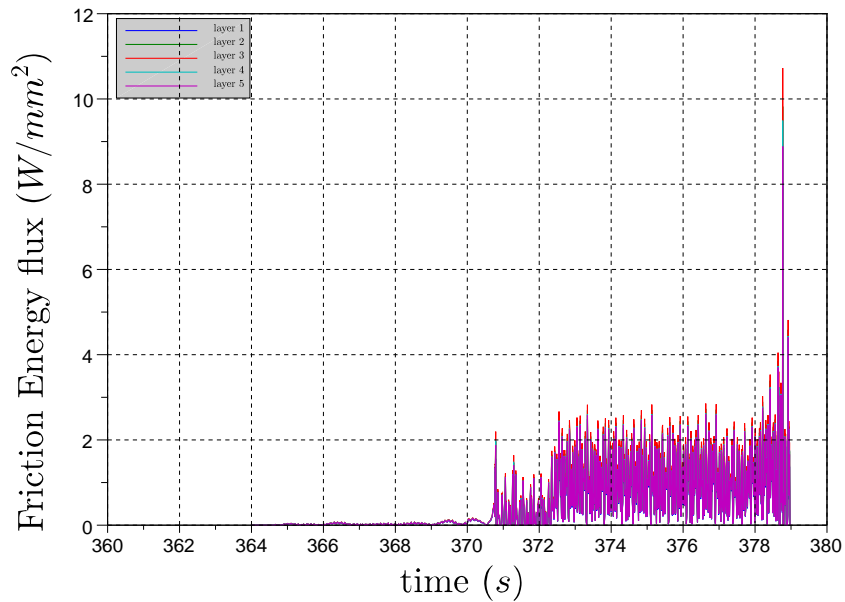


Figure 49: Energy flux on line contact area due to axial loading shown in figure 48.

## 6.2 Temperature Change

In the FEM package Ansys the temperature change has been modeled. Because of symmetry a cross-section of a wire has been modeled with the surrounding lubricant (SAE-90). It is stressed here that the model merely gives an impression.

The elements *Plane55* are used. The contact width  $b$  is not expected to influence the dissipation throughout the material significantly. It is thus chosen to take an average width.

The heat flux is applied on the surface as a constant. The constant value is taken from the highest heat flux calculated by the TP for both the  $39\text{mm}$  SSR and the  $40\text{mm}$  MSR.

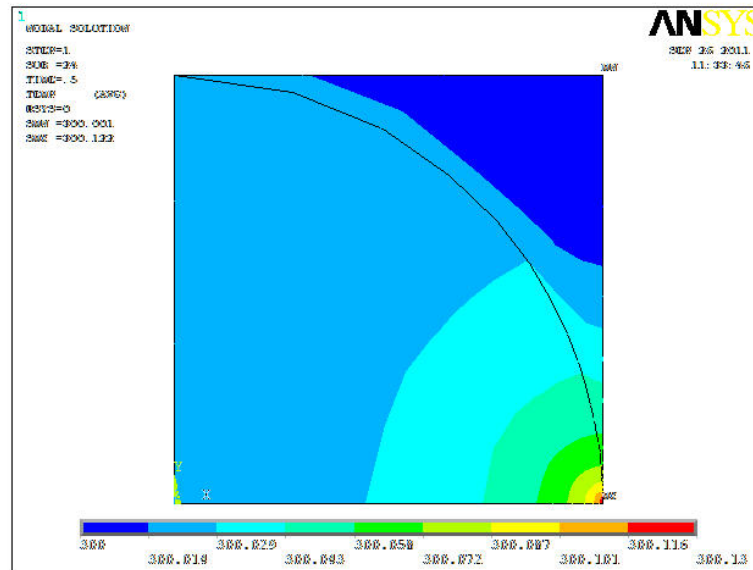


Figure 50: Temperature change after 0.5s of the highest magnitude of heat flux,  $11\text{kW}/\text{m}^2$  resulting from non-cyclic dynamic model for the  $39\text{mm}$  SSR.

For constant heat flux of large magnitudes as seen in figure 49, only a few tenths of degrees at the wire surface are expected.

## 6.3 Conclusions

The heat flux generated in a wire rope subjected to a cyclic load and to a non-cyclic load as yielded by [4]:

- Significant more, several orders, frictional energy generated under random like load compared to a cyclic load of same magnitude.
- No significant temperature rise, order of tenths of degrees, to be expected as a consequence from a non-cyclic loading.

## 7 Conclusions and Recommendations

### 7.1 Conclusions

First, for the chapters 4 to 6, the questions and conclusions are repeated here. Finally, the main conclusions that are drawn from these collective findings.

#### Chapter 4

- *What might cause premature failure of a wire rope resulting from slack combined with tensile loads with shockload (like) characteristics that occur during the jacket decommissioning by the Pieter Schelte?*

Four causes of possible premature failure have been preliminarily investigated:

1. Stress Doubling.
2. Birdcaging.
3. Hockling.
4. Frictional Energy Generation.

It has been found here that stress doubling is very unlikely to occur. Birdcaging and hockling, however, might occur. Techniques to determine whether they occur are available within Allseas. There are no techniques readily available to investigate frictional energy generation. It is therefore chosen to focus thereon, thus:

- *More insight is needed into frictional energy generation within wire ropes with respect to heat dissipation and resulting potentially significant temperature changes of the wire rope material.*
- *What is a suitable method to investigate the chosen cause of failure?*

Closed form theories and FEM approaches have been investigated. The FEM approaches have been found to take too much computing time, e.g. 21 hours, without yielding the desired information. Only one theory, the *Orthotropic Sheet Theory*, has been found to yield the desired information, thus:

- *It is chosen to apply the Orthotropic Sheet Theory (OST) to determine the frictional energy generated in a wire rope subjected to cyclic and non-cyclic tensile loading.*

**Chapter 5** The *Orthotropic Sheet Theory* (OST) is explained here. A program has been written (TP) and the results have been compared to examples from papers by M. Raouf. There is no full compliance between these examples and the TP. In appendix B.7 it is shown what the resulting differences are. It is also reasoned that the results can still be used to gain insight on internal frictional energy. The OST has been mainly developed for SSR's. The wire rope used for the jacket decommissioning by the PS, however, are MSR's. An analytical approach has been investigated though found to be impossible. Another approach is to first model a MSR as a SSR where the helical strands are treated as wires. The strains can be determined and subsequently the inter behavior of each helical strand can be analysed. It must then be assumed that the helical strands can be approached as being straight.

- *Despite non full compliance with examples in papers, there is confidence in using the line contact forces for investigating internal friction.*
- *OST implemented for MSR's.*

The intermediate result yielding the line contact forces and inter-wire slippage is used to develop an implementation for a dynamic model. The *stick-slip* behavior is neglected here because the slippages for the non-cyclic tensile loading expected for the jacket decommissioning are difficult to average and have significant more slippage than a cyclic loading. Also, because neglecting the stick-slip behavior results in higher friction forces, frictional energy will be higher. If the frictional energy does not endanger the lifespan of the wire rope, it will do so less when the stick-slip behavior *is* taken into account.

- *OST adapted for implementation in cyclic and random like dynamic model.*

**Chapter 6** *First*, a dynamic model has been developed. The OST is adapted for dynamic implementation as described in section 5.2.4.

Results have been compared between cyclic and non-cyclic loading. The resulting frictional energy is significant higher than for a cyclic loading. Not only because the stick-slip behavior is neglected, but especially because the tensile load spikes are much higher.

*Second*, the resulting frictional energy has used to investigate the temperature change within the wire. The temperature changes range from a few tenths degrees to several degrees, e.g. 9.

- *Effect of friction forces negligible compared to effects of axial load. Thus friction forces can be calculated outside the convergence loop of the Newmark Integrator.*
- *Significant more frictional energy generated under random like load compared to a cyclic load of same magnitude.*
- *No significant temperature rise to be expected as a consequence from a random like loading.*

## Main Conclusions

The research question has been aimed at answering whether the tensile loading characteristics can result in a significant temperature. It has been found that a lower limit of 50° C can lead to degradation of the lubricant and is advised to be avoided. According to the modeling this temperature will not be reached.

## 7.2 Recommendations

- Install wire breakage detectors, if only to learn more with respect to fatigue.
- Address the effect of random like loading on fatigue life (trellis contacts).
- Address the differences in results between the results found in the various papers and the results of the TP.





- Investigate hocking and birdcaging.
- Finish dynamic model for MSR's.
- Develop model for frictional energy generation within a wire rope subjected to repeated bending, e.g. for a heave compensating system.
- Perform curve fitting once a wire rope has been analyzed to create for e.g. the Young's Modulus as function of tensile strain. This will reduce the computing time significantly.





# APPENDICES



## A Wire Rope Geometry

In this appendix the geometric description of a core wire (single helix) and of a non-core wire (double helix) in a helical strand in a MSR, will be shown. The subscripts  $i$  and  $j$  in this section refer to the strand layer and wire layer respectively, where 0 is the core strand and 1 the first layer of strands around the rope core and so forth. The same convention applies to the wire layer. Taking thus i.e.  $r_{12}$ , this will refer to the radius of the *second layer* of wires around the core wire in a strand. That strand itself is part of the *first layer* of strands around the core of the wire rope, see figure 51.

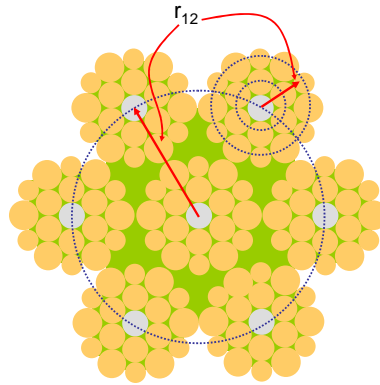


Figure 51: Cross-section of a MSR wherein the use of the subscripts in this section are clarified.

### A.1 Core Wire of a Helical Strand (Single Helix)

The core wire of a helical strand is a single helix. In figure 52 a part of the helix is shown. The helix properties are the lay-angle  $\alpha_{ij}$  and the helix radius  $r_{ij}$ . The single helical coordinates are described with the the polar angle  $\phi_{ij}$  in the  $\{x, y, z\}_j$  frame. This angle rotates around the longitudinal axis of the helix which is here chosen to be the  $z_0 - axis$  and coincides with the center line of the wire rope. Note again the use of the subscripts. In this case it is thus the core wire of a helical strand in the first strand layer. Thus this helix is described with  $\phi_{10}$  in the  $\{x, y, z\}_0$  frame. Its  $z_0 - axis$  is aligned with the longitudinal center axis of the wire rope. The orientations of the  $x -$  and  $y - axis$  are free, as long as they are orthogonal to the  $z - axis$  so the axes form an orthogonal reference frame. The parametric function is:

$$H_{10}(\phi_{10}) \begin{cases} x_0 = r_{10} \cos \phi_{10} \\ y_0 = r_{10} \sin \phi_{10} \\ z_0 = r_{10} (\cot \alpha_{10}) \phi_{10} \end{cases} \quad (22)$$

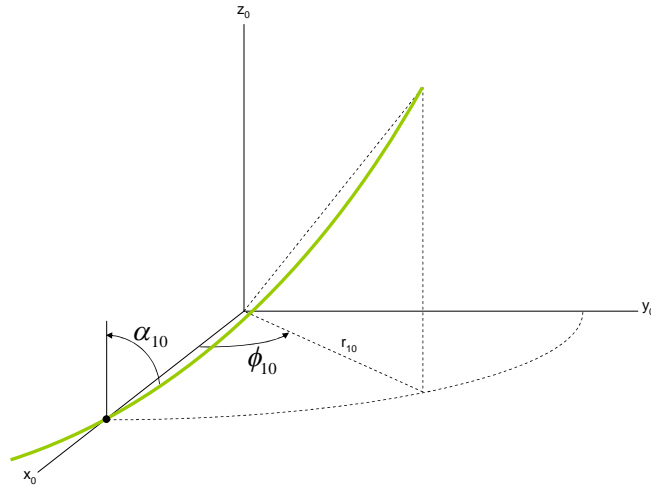


Figure 52: Geometry of the core wire of a helical strand in the first layer.

## A.2 Wires in a Helical Strand (Double Helix)

The double helix is a helix with respect to a center line that itself is a helix, hence *double* helix. To describe a double helix, a second reference frame is used, here denoted as the  $\{x, y, z\}_1$  frame. As an illustrative example, the first wire layer in the first strand layer is considered here. The subscripts are thus  $i = 1$  and  $j = 0$  for the single helix (core wire of strand), and  $i = 1$  and  $j = 1$  for the double helix (helical wire inside the strand). The aim in this section is to derive a parametric description of the double helix as a function of one variable, namely  $\phi_{10}$  in this example, in the  $\{x, y, z\}_0$  frame.

The double helix is first described as a single helix in the  $\{x, y, z\}_1$  frame. The origin of this frame is located at the (single) helical coordinates described by the polar angle  $\phi_{10}$  from the previous paragraph, equation 22. One can say that at first the axes of both frames are coincidental. Then the  $\{x, y, z\}_1$  frame is translated to the single helix coordinates described by  $H_{10}(\phi_{10})$ , equation 22. These coordinates form a vector  $\mathbf{d}_{10}$  which is the linear translation with respect to the origin of the  $\{x, y, z\}_0$  frame. As will be shown later in this section, subsequently the coordinates of  $H_{11}(\phi_{11})$ , equation 24, need to be rotated twice, first with an angle  $\phi_{10}$  and second with an angle  $\alpha_{10}$ . This transformation is performed with a final rotation matrix  $\mathbf{R}_{\phi_{10}\alpha_{10}} = \mathbf{R}_{\phi_{10}}\mathbf{R}_{\alpha_{10}}$ .

So  $H_{11}(\phi_{11})$  is described in the  $\{x, y, z\}_1$  frame as a single helix and this frame follows the tangent of the single helix  $H_{10}(\phi_{10})$ . These coordinates are then transformed to the  $\{x, y, z\}_0$  frame in such a way that they form a double helix, denoted as  $h_{11}(\phi_{10})$ , with respect to the  $\{x, y, z\}_0$  frame. In vector notation the double helix  $\mathbf{h}_{11}$  can be described as, see figure 53:

$$\mathbf{h}_{11} = \mathbf{d}_{10} + \mathbf{R}_{\phi_{10}\alpha_{10}}\mathbf{H}_{11} \quad (23)$$

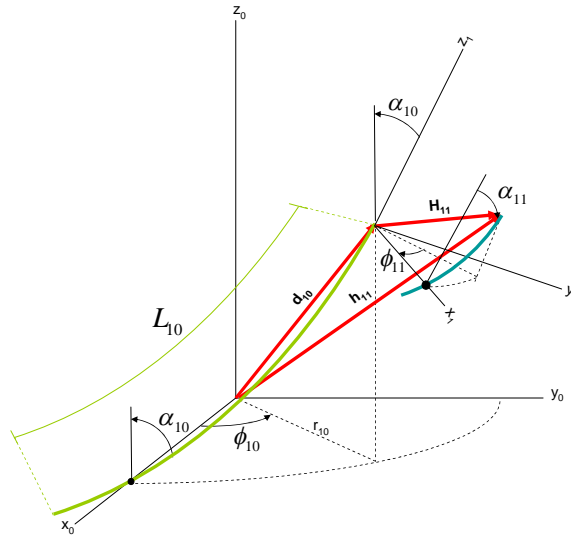


Figure 53: Geometry of the centre wire of a helical strand in the first layer.

The helical wire within the helical strand, and thus within the  $\{x, y, z\}_1$  frame, is described with the parametric function:

$$H_{11}(\phi_{11}) \begin{cases} x_1 = r_{11} \cos \phi_{11} \\ y_1 = r_{11} \sin \phi_{11} \\ z_1 = r_{11} (\cot \alpha_{11}) \phi_{11} \end{cases} \quad (24)$$

The  $z_1 - axis$  of the  $\{x, y, z\}_1$  frame is tangent to the single helix. This tangent is determined by the polar angle  $\phi_{10}$  describing the single helical core wire and its lay-angle  $\alpha_{10}$ .

Now let's say that at first both reference frames are fully coincidental. The coordinates of the double helix thus first need to be translated to the single helix with the vector  $\mathbf{d}_{10}$ . The next step is to make the  $z_1 - axis$  tangent with the single helix  $\mathbf{H}_{10}(\phi_{10})$ . This is accomplished with a rotation *first* around its  $z_1 - axis$  with polar angle  $\phi_{10}$  and *second* around the  $x - axis$  with angle  $\alpha_{10}$ . Note that for the first rotation it is necessary that  $H_{10}(\phi_{10} = 0) = [r; 0; 0]$ . These rotations can be performed with *rotation matrices*. They are for the polar angle  $\phi_{10}$ ;

$$R_{\phi_{10}} = \begin{bmatrix} \cos \phi_{10} & -\sin \phi_{10} & 0 \\ \sin \phi_{10} & \cos \phi_{10} & 0 \\ 0 & 0 & 1 \end{bmatrix} \quad (25)$$

and for the lay-angle  $\alpha_{10}$ :

$$R_{\alpha} = \begin{bmatrix} 1 & 0 & 0 \\ 0 & \cos \alpha_{10} & \sin \alpha_{10} \\ 0 & -\sin \alpha_{10} & \cos \alpha_{10} \end{bmatrix} \quad (26)$$

Note that the order *cannot* be chosen freely. A different order will result in a different transformation of coordinates, in other words; the multiplication of rotation matrices is not commutative. The final

rotation matrix is:

$$R_{\phi_{10}\alpha_{10}} = \begin{bmatrix} \cos \phi_{10} & -\sin \phi_{10} \cos \alpha_{10} & \sin \phi_{10} \sin \alpha_{10} \\ \sin \phi_{10} & \cos \phi_{10} \cos \alpha_{10} & \cos \phi_{10} \sin \alpha_{10} \\ 0 & -\sin \alpha_{10} & \cos \alpha_{10} \end{bmatrix} \quad (27)$$

The length of the helical strand can be written as a function of  $\phi_{10}$ . The length of this helix is determined with an integral that sums infinitesimal lengths determined with the Pythagoras theorem. In this case the length of the single helix,  $L_{10}$  is thus:

$$\begin{aligned} L_{10} &= \int_0^{\phi_{10}} \sqrt{\left(\frac{dx}{d\phi_{10}}\right)^2 + \left(\frac{dy}{d\phi_{10}}\right)^2 + \left(\frac{dz}{d\phi_{10}}\right)^2} d\phi_{10} \\ &= \int_0^{\phi_{10}} r_{10} \sqrt{1 + \cot^2 \alpha_{10}} d\phi_{10} \\ &= r_{10} \sqrt{1 + \cot^2 \alpha_{10}} \phi_{10} \end{aligned} \quad (28)$$

This length of the single helix at  $\phi_{10}$  is equal to the  $z$ -coördinate of the helix in the  $\{x, y, z\}_1$  frame, equation 24. A relation can thus be made between the polar angles  $\phi_{10}$  and  $\phi_{11}$  through the length  $L_{10}$  of equation 28;

$$\begin{aligned} L_{10} &= r_{10} \sqrt{1 + \cot^2 \alpha_{10}} \phi_{10} \\ &= r_{11} (\cot \alpha_{11}) \phi_{11} = z_1 \end{aligned} \quad (29)$$

and thus:

$$\phi_{11} = \frac{r_{10} \sqrt{1 + \cot^2 \alpha_{10}} \phi_{10}}{r_{11} (\cot \alpha_{11})} \quad (30)$$

It is now possible to describe the geometry of the double helical wire in the helical strand as a function of the polar angle  $\phi_{10}$  with respect to the reference  $\{x, y, z\}_0$ :

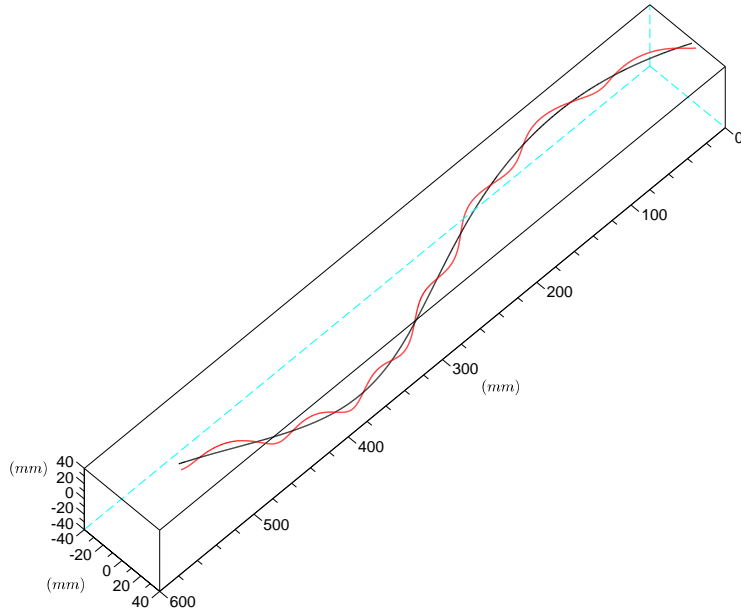
$$h_{11}(\phi_{10}) = \begin{bmatrix} r_{10} \cos \phi_{10} \\ r_{10} \sin \phi_{10} \\ r_{10} (\cot \alpha_{10}) \phi_{10} \end{bmatrix} + \begin{bmatrix} \cos \phi_{10} & -\sin \phi_{10} \cos \alpha_{10} & \sin \phi_{10} \sin \alpha_{10} \\ \sin \phi_{10} & \cos \phi_{10} \cos \alpha_{10} & \cos \phi_{10} \sin \alpha_{10} \\ 0 & -\sin \alpha_{10} & \cos \alpha_{10} \end{bmatrix} \begin{bmatrix} r_{11} \cos \phi_{11} \\ r_{11} \sin \phi_{11} \\ r_{11} (\cot \alpha_{11}) \phi_{11} \end{bmatrix} \quad (31)$$

On the right side of equation 31 the first term describes the location of the  $\{x, y, z\}_1$  frame, the second term describes the rotation of the coördinates written in the  $\{x, y, z\}_1$  frame. The final description of the double helix coördinates in the  $\{x, y, z\}_0$  frame is then:

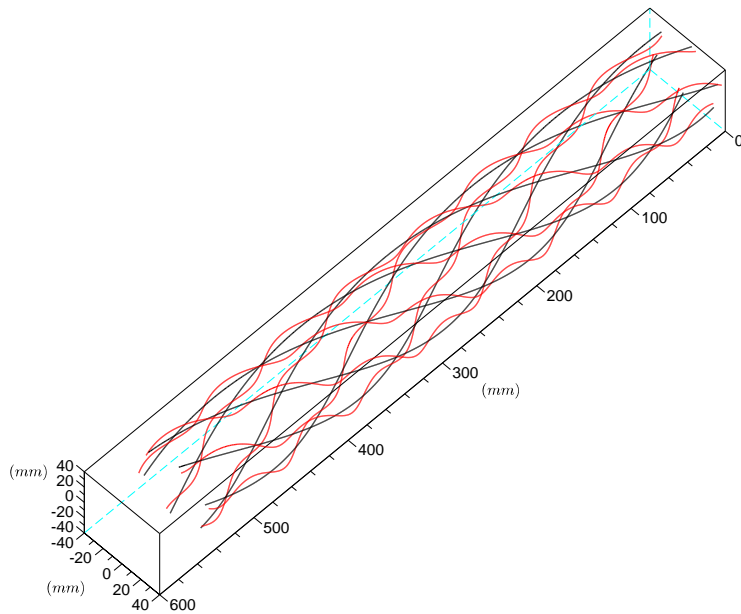
$$h_{11}(\phi_{10}) = \begin{bmatrix} r_{10} \cos \phi_{10} + r_{11} \cos \phi_{10} \cos \phi_{11} + r_{11} \sin \phi_{10} \cos \alpha_{10} \sin \phi_{11} \\ r_{10} \sin \phi_{10} - r_{11} \sin \phi_{10} \cos \phi_{11} + r_{11} \cos \phi_{10} \sin \alpha_{10} \sin \phi_{11} \\ r_{10} (\cot \alpha_{10}) \phi_{10} - r_{11} \sin \alpha_{10} \sin \phi_{11} \end{bmatrix} \quad (32)$$

To check this derivation a small program has been written. The resulting plots can be found in figure 54. Only one double helical wire is plotted per strand.





(a) Plot of one helical strand with one double helical wire.



(b) Plot of six helical strands each with one double helical wire.

Figure 54: Plot of a helical wire (red) around the core wire (black) of a helical strand.



## B Orthotropic Sheet Theory

In section 5 flowcharts are shown for:

- determining the Young's modulus of a strand around a mean tensile load.
- determining the constants  $\Delta_{lmax}$ ,  $S_{22}$  and  $P_{MS}$  around a mean tensile load.
- determining specific damping  $\psi = \frac{\Delta U}{U}$  for different perturbations around a mean tensile load.

In this appendix more light will be shed on the grey blocks in these flowcharts. Each of these grey blocks hides one or more equations and reasoning. The explanation is based on the work of M. Raof. The first published paper is of on his phd work, [23]. Thereafter he has published several more papers that are built on [23], amongst others these are [24], [25], [26], [27], [32] and [33].

The work of M. Raof is for some parts based on the work of Costello, [7] and [8], and Chi [6]. These two authors, however, have defined the lay-angle differently. For the reader that is interested in verifying the derivations for helical deformations based on the aforementioned work, a deconfusing drawing is presented here, figure 55.

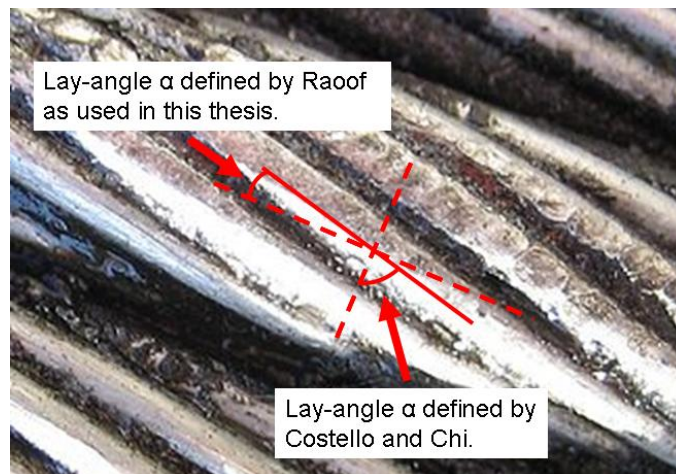


Figure 55: Lay angel  $\alpha$  as defined by the different authors.

### B.1 Symbols and Notation

Notation deviates from conventional notation. A table is presented here containing the symbols and notations as used in Raof's work and as used in other texts. Also presented are symbols that are exclusively used for the OST. In the wire layer the  $x$ -axis is coinciding with the wire centerline.

Orthotropic Tensor in Wire Layer					
$\begin{bmatrix} S_1 \\ S_2 \\ S_6 \end{bmatrix} = \begin{bmatrix} S_{11} & S_{12} & 0 \\ S_{12} & S_{22} & 0 \\ 0 & 0 & S_{66} \end{bmatrix} \begin{bmatrix} T_1 \\ T_2 \\ T_6 \end{bmatrix}$	$\equiv$	$\begin{bmatrix} \epsilon_x \\ \epsilon_y \\ \gamma_{xy} \end{bmatrix} = \begin{bmatrix} \epsilon_{11} & \epsilon_{12} & 0 \\ \epsilon_{21} & \epsilon_{22} & 0 \\ 0 & 0 & \epsilon_{33} \end{bmatrix} \begin{bmatrix} \sigma_x \\ \sigma_y \\ \tau_{xy} \end{bmatrix}$	<b>Material Tensor</b>	<b>Strain</b>	
$S_{6T}$	:	Tensor shear strain within wire layer.			
$S'_{2C}$	:	Radial strain of layer with the rigid core present and includes rigid body movement of the wires and the contact patch deformations.			
$S'_{2R}$	:	Strand radial strain due to changes of lay-angle where the wires are treated as rigid bodies and the rigid core is absent.			

Here the  $z - axis$  is coinciding with the strand centerline.

## B.2 Strand Kinematics

**Strand Kinematics**

The kinematics of a system describe the motions and deformations of the bodies without considering the forces acting on it. In other words applying to a wire rope:

*How do the movements and deformations of wires and strands in a wire rope relate to each other when the wire rope is subjected to a tensile strain  $T'_1$ .*

The basic shape of the strand design is the helix. The helix properties, i.e. lay-angle  $\alpha$  and helix radius  $r$ , can alter the strand properties. In e.g. [32] the influence of the lay-angle on the strand stiffness, torsional and tensile, is investigated. In an actual strand, the wires might deviate from the perfect helical shape. Though this deviation is assumed to have negligible effects on the strand properties. Therefore, the shape of the wires in a strand is assumed to be a perfect helix. Moreover, it is assumed that:

*Center line of wire forms a helix both before and after deformation.*

And so the kinematic analysis of a strand starts with the parametric representation of this helix. The helix is described by the polar angle  $\phi$ . So if  $\phi = 360$ , a wire has wound one revolution around the longitudinal axis of a strand. In appendix A, the parametric equations of a single helix are explained in more detail. They are reproduced here without the subscripts. The  $z$ -coordinate is coincidental with the strand axis, see figure 52:

$$x = r \cos \phi \tag{33a}$$

$$y = r \sin \phi \tag{33b}$$

$$z = r (\cot \alpha) \phi \tag{33c}$$

There are three radial strains defined for the kinematic relations. *First*, the net radial strand strain  $S'_2$  to

be used for the orthotropic sheet is the strain that occurs including trellis contact patch deformations. It is the difference between the two other radial strains to be defined  $S'_{2C}$  and  $S'_{2R}$ . The latter does not represent wire deformations and must therefore be subtracted from the former yielding:

$$1. \quad S'_2 = S'_{2C} - S'_{2R} \quad (34)$$

Second, for the radial strand strain  $S'_{2C}$  of a wire layer, the wires are subject to a tensile strain  $S_1$  and the effect thereof is taken into account. The subscript  $C$  refers to the rigid core being removed. To determine  $S'_{2C}$ , first a relation needs to be derived between the helix properties  $r$  and  $\alpha$  and the strand strain  $S'_1$ .

The deformed and undeformed strand lengths  $L'$  and  $L$  can be described with equation 33c, where  $z$  is equal to the strand length. Consider now that for a strand subjected to a pure tensile strain, the ends are not permitted to rotate and thus,

$$\frac{\phi' - \phi}{L} = 0 \quad (35)$$

and applying equation 35 for the deformed and undeformed strand lengths  $L'$  and  $L$  described by equation 33c yields:

$$\begin{aligned} \frac{\tan \alpha}{r} - \frac{L'}{L} \frac{\tan \alpha'}{r'} &= 0 \\ \frac{\tan \alpha'}{\tan \alpha} &= \frac{L}{L'} \frac{r'}{r} \end{aligned} \quad (36)$$

The strand tensile strain can be written as  $\frac{L}{L'} = \frac{1}{1+S'_1}$ , and substituting into equation 36 yields the desired relation:

$$\frac{\tan \alpha'}{\tan \alpha} = \frac{r'}{r(1+S'_1)} \quad (37)$$

By now substituting the radial strain relation  $r' = r(1+S'_{2C})$  into equation 37, a relation can be made between the radial strain  $S'_{2C}$  and the strand strain and lay-angles before and after deformation:

$$2. \quad S'_{2C} = (1+S'_1) \frac{\tan \alpha'}{\tan \alpha} - 1 \quad (38)$$

Third, a strand radial strain,  $S'_{2R}$ , due to change in lay-angle resulting from the axial strand deformation can be derived. The subscript  $R$  refers to the wires being treated as rigid bodies and experience thus, unlike for  $S'_{2C}$ , no strain. Its relation is analogous to  $S'_{2C}$ , thus  $r' = r(1+S'_{2R})$ .

The helix radii  $r$  and  $r'$  are now a function of the wire radius  $R$  and the lay-angle  $\alpha$  and  $\alpha'$  before and after deformation respectively. The helix radii can be determined exactly when the following ideal situation is assumed:

*In the unloaded situation the wires within the layer are just touching each other.*

Furthermore, it is also assumed that:

*The cross-section of the thin wires is an ellipse.*

It is then possible to derive an exact relation for the helix radius  $r$  geometrically, figure 56. They

have been derived in [7] by G.A. Costello and are reproduced here:

$$\frac{r}{R} = \sqrt{1 + \frac{\tan^2 \left( \frac{\pi}{2} - \frac{\pi}{n} \right)}{\cos^2 \alpha}} \quad (39)$$

Note that  $\alpha$  in [7] is defined differently, namely with respect to the radial strand axis instead of the axial strand axis, figure 55, and is therefore described with a sine term instead of a cosine term. By looking now at equation 39, one can see that under a positive strain of a strand, where  $\alpha' < \alpha$ , the helix radius becomes smaller after deformation,  $r' < r$ .

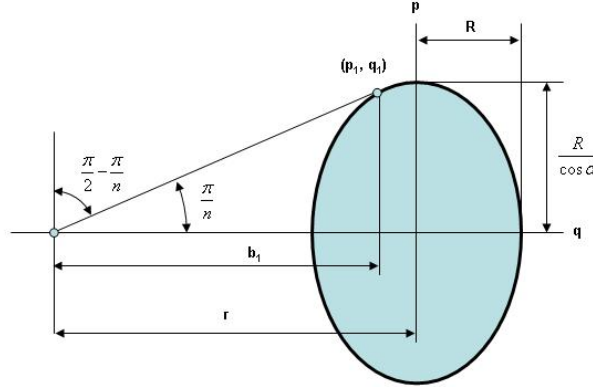


Figure 56: Cross-section of helical wire normal to strand axis.

By using equations 39 and strain expression  $S_{2R} = \frac{r'-r}{r}$ , a relation can be derived between the lay-angles  $\alpha$  and  $\alpha'$  and the helix radii  $r$  and  $r'$  before and after deformation. Note that this strain is a result of change in lay-angle that occurs as a result of axial strand deformation  $S'_1$ , but *not* due to deformation of the wires themselves. The wires are treated as rigid bodies. Furthermore, the wires are *just touching* before and after the change in lay-angle  $d\alpha$ . Consequently,  $S_{2R}$  does not contribute to inter-wire forces and deformations. The relation for  $S_{2R}$  is:

$$\boxed{3.} \quad S'_{2R} = \sqrt{\frac{\cos^2 \alpha \left( \cos^2 \alpha' + \tan^2 \left( \frac{\pi}{2} - \frac{\pi}{n_i} \right) \right)}{\cos^2 \alpha' \left( \cos^2 \alpha + \tan^2 \left( \frac{\pi}{2} - \frac{\pi}{n_i} \right) \right)}} - 1 \quad (40)$$

For strands with non-rotating ends, the tensile wire strain  $S_1$  is derived by Chi [6], as mentioned in [23]. It is an exact geometric derivation between the engineering strains in the helical and core wires. It must be noted that, as earlier mentioned for the theories in [7], the lay angle  $\alpha$  is defined with respect to the radial strand axis as opposed to the strand axial axis, figure 55. The expression of the radial strain for the helix radius deformation,  $\frac{r'}{r} = 1 + S'_{2R}$ , is substituted therein. Note again that the ends are not permitted to rotate, thus  $\phi = 0$ :

$$\begin{aligned} S_1 &= \cos \alpha \sqrt{(1 + S'_1)^2 + \left( \frac{r'}{r} \tan \alpha - r' \frac{r' \phi}{L} \right)^2} - 1 \quad [6] \\ &= \cos \alpha \sqrt{(1 + S'_1)^2 + (1 + S'_{2R}) \tan^2 \alpha} - 1 \end{aligned} \quad (41)$$

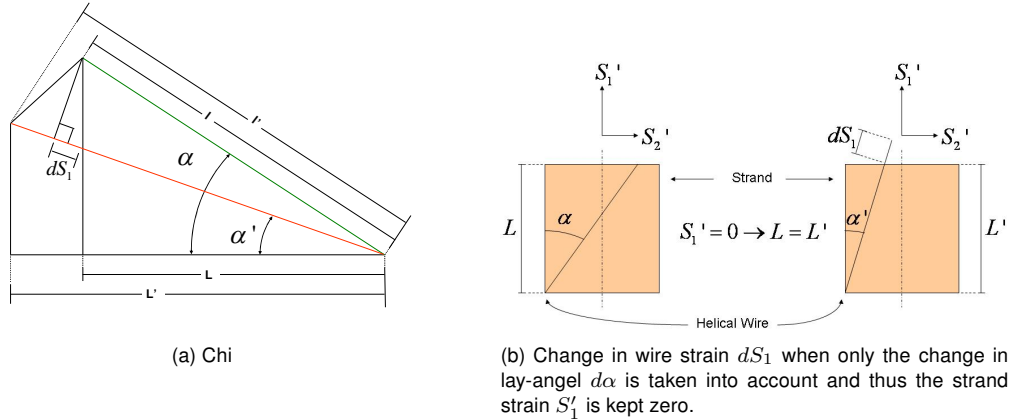


Figure 57: eeeh

Due to the change in lay-angle there is a slight change in tensile wire strain  $S_1$ . Subsequently this change  $dS_1$  can be found by setting the strand strain  $S_1'$  to zero where now the (negative) tensile wire strain as a consequence of strand tensile strain is taken out of the relation and thus:

$$4. \quad \cos \alpha \sqrt{1 + (1 + S_{2R}') \tan^2 \alpha} + 1 - dS_1 = 0 \quad (42)$$

The next relation involves the tensorial shear strain  $S_{6T}$  which is directly related to the inter-wire slippage  $\Delta_l$ . This slippage is crucial in determining the inter-wire friction. A sketch has been reproduced here from [23] for clarification in deriving this important relation. In figure 58 the diameter  $D$  before and after deformation remains the same, though there is actually transverse contraction resulting from tensile wire strain. The following assumption is thus made for deriving the expression for inter-wire slip,  $\beta$ , in presence of a rigid core.

*The influence of the transverse contraction is assumed negligible for the derivation of the wire slippage  $\beta$  in the presence of a rigid core.*

Thus,

$$\beta = D (\tan \alpha (1 + S_1 - dS_1) - \tan \alpha') \quad (43)$$

In figure 58 it can be seen that the engineering shear strain  $\gamma$  is accounted fully by the change in  $\alpha$  in accordance with the above assumption and thus resulting only in a diametral shear strain. The influence of the deformed wire diameter  $D'$ , however, is taken into account for the diametral shear strain. The engineering shear strain, considering angles  $\ll 1^\circ$ , is:

$$\begin{aligned} \tan \gamma &= \frac{\beta}{D'} = \frac{\sin \gamma}{\cos \gamma} \approx \frac{\gamma}{1} \\ \gamma &= \frac{\beta}{D'} \end{aligned} \quad (44)$$

Now the tensorial shear strain is  $S_{6T} = \frac{1}{2}\gamma$  and the diametral wire strain within a wire layer is  $S_2 =$

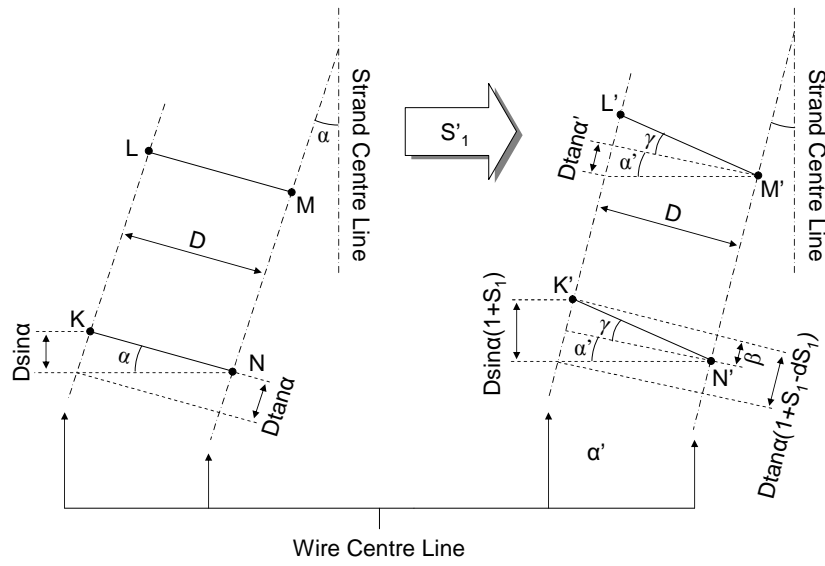


Figure 58: Sketch clarifying the derivation for the wire slippage between two adjacent helical wires.

$\frac{D'-D}{D}$ . Applying these expressions to equations 43 and 44 yields the following relation for  $S_{6T}$ :

$$5. \quad S_{6T} = \frac{\tan \alpha (1 + S_1 - dS_1) - \tan \alpha'}{2(1 + S_2)} \quad (45)$$

A straightforward derivation of a relation between  $S'_1$  and  $S_1$  and  $\alpha$  and  $\alpha'$  before and after deformation can be made from Figure 59a, yielding:

$$6. \quad \frac{1 + S'_1}{\cos \alpha'} = \frac{1 + S_1}{\cos \alpha} \quad (46)$$

In figure 59 the coordinate transformation is shown for strands. The following relations can be derived therewith;

$$7. \quad -\frac{S'_1 - S'_2}{2} \cos 2\alpha' + \frac{S'_1 + S'_2}{2} - S_2 = 0 \quad (47)$$

and,

$$8. \quad S_{6T} - \frac{S'_1 - S'_2}{2} \sin 2\alpha' = 0 \quad (48)$$



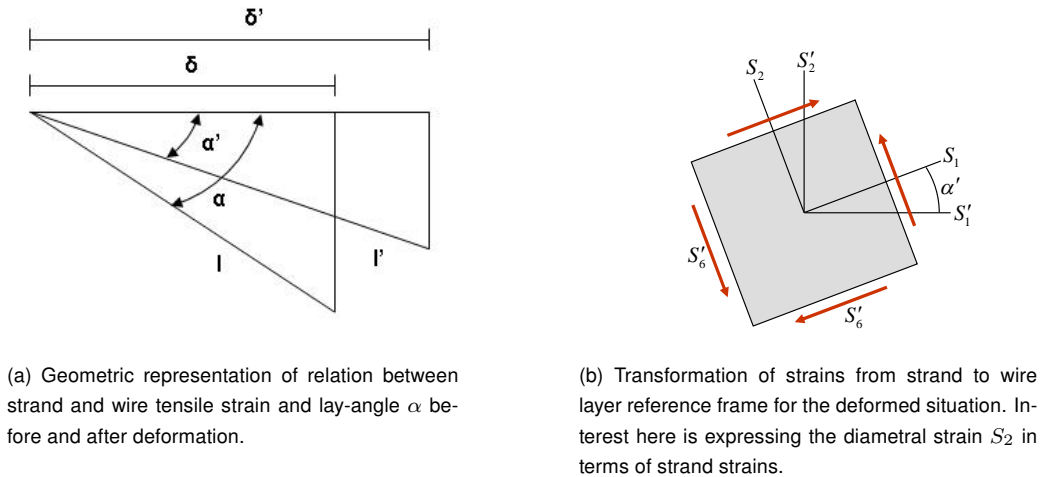


Figure 59: Strain relations between strand and wire layer.

There are now an equal number of equations and unknowns, equations 34, 38, 40, 42, 45, 46, 47 and 48. It is now possible to find a solution for  $S_1, S_2, S_{6T}, S'_2, S'_{2C}, S'_{2R}, \alpha', dS_1$ . The aforementioned equations are, however, strongly non-linear and thus cannot be solved with a Gauss elimination as with a linear set of equations. A well known method to find a solution for these type of problems is the Newton-Raphson method, see section E.1.

### B.3 Internal Forces of a Strand

In this section, the determination of the forces that are at play within a strand are explained. *First*, the line-contact force  $P_{RC_i}$  is determined for each wire-layer  $i$ . For  $P_{RC_i}$  (RC is Rigid Core) the outer-layer forces are not considered. *Next*, all forces at play are considered to determine the actual line-contact force  $P_{MS_i}$  (MS is Multi-layerd Strand) for this statically indeterminate problem. The latter will be used in conjunction with  $\mu$  to determine the frictional force  $F_{fric_i} = \mu P_{MS_i}$  between two adjacent wires in wire layer  $i$ .

#### Line-contact Forces

In section B.2, kinematic relations have been derived for a strand subjected to a pure tensile strain  $S'_1$ . Solving these relations yields the diametral strain  $S_2$  amongst others. To accommodate for  $S_2$ , the wires will deform. This deformation is directly related to the line-contact force between the two adjacent wires, thus:

*What is the line-contact force  $P_{RC_i}$  in wire layer  $i$  between two adjacent wires subjected to a diametral strain  $S_{2_i}$  that results from a strand tensile strain  $S'_1$ .*

The line-contact force  $P_{RC}$  is calculated within each wire layer. The subscripts  $RC$  refer to situation where each layer is investigated as if it is resting on a rigid core. The assumption for  $P_{RC_i}$  is:

Each layer is approached as resting on a rigid core and outer layers are absent.

With  $S_2$  the diametral deflection  $\delta_n$  can be determined. The diametral deflection is the change in distance between the centerlines of two wires in line-contact, figure 60. Even though this deflection is not linear it can be approximated as such because  $\delta_n \ll D_1 < D_2$ . Here  $D = \frac{1}{2}(D_1 + D_2)$ :

$$\delta_n = (D' - D) = S_2 D \tag{49}$$

Another way to determine the diametral deflection  $\delta_n$  is to apply *Hertz contact theory*. This theory has been developed by Heinrich Hertz. It encompasses localized stresses that develop as two curved surfaces come in contact and deform slightly under the imposed loads. The deformation of the surfaces depends on the geometry of the object, normal contact forces between the bodies (e.g  $P_{RC}$ ) and the material properties Poisson's ratio  $\nu$  and Young's modulus  $E$ . Formula's resulting from this theory have been collected by Roark and Young and have been reissued in [42].

Two formulas consider two cylinders in line-contact pressed together. In [23] the cylinders have equal

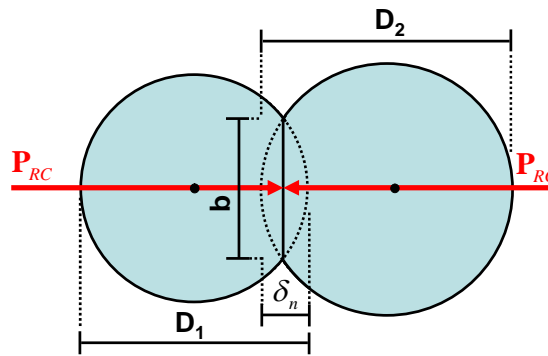


Figure 60: Cross-section of two wires in line-contact showing the diametral deflection  $\delta_n$  as a result of the line-contact force  $P_{RC}$ .

diameters. The wire rope to be used for the JLS, however, contains wire layers consisting two *unequal* wire diameters alternately. The steps taken by M. Raof in [23] thus have to be followed to derive a relation for  $P_{RC}$  for unequal wire diameters based on the contact formula's in [42]. An important note is that  $b$  refers to *half* the line-contact width in [23] and to the *full* line-contact width in [42]. The derivation of half the contact width is used for  $b$  as in [23].

*First*, the formula relating the line-contact width  $b$  to the line-contact force  $P_{RC}$  and the wire (material) properties is:

$$b = 0.8 \sqrt{\frac{D_1 D_2}{D_1 + D_2} \frac{2 P_{RC} (1 - \nu^2)}{E_{steel}}} \tag{50}$$

*Second*, the diametral deflection  $\delta_n$  is given to be:

$$\delta_n = \frac{2 P_{RC} (1 - \nu^2)}{\pi E_{steel}} \left( \frac{2}{3} + 2 \ln \frac{\sqrt{D_1 D_2}}{b} \right) \tag{51}$$

By substitution of equation 50 into equation 51, a very non-linear relation results. The only unknown here is  $P_{RC}$ . Recall that  $\delta_n$  can be determined with equation 49:

$$C_1 = \frac{4(1-\nu^2)}{\pi} \quad (52a)$$

$$C_2 = C_1 \left( \frac{1}{3} + \ln \left( \frac{1}{0.8\sqrt{2(1-\nu^2)}} \right) \right) \quad (52b)$$

$$\boxed{1.} \quad \delta_n = \frac{P_{RC}}{E_{steel}} \left( C_2 + C_1 \ln \left( \sqrt{\frac{E_{steel}(D_1 + D_2)}{P_{RC}}} \right) \right) \quad (52c)$$

To solve this relation, a second Newton-Raphson iteration is performed to obtain the unknown  $P_{RC}$ . With the normal loads between the wires now known, in each layer of the strand, load transfer from one layer to the next (moving inward layer by layer) can be taken into account. This is described next.

**Radial load transfer**

For each wire layer  $i$  it is possible to determine the normal line contact force,  $P_{RC_i}$ , between the wires. The above derived  $P_{RC_i}$  is determined with the assumption that a rigid core is present and that there are no other forces acting upon the layer. The subscripts  $RC$  refer to the rigid core being present.

Resulting forces in one layer acting upon the next one thus still need to be taken into account and are denoted as  $P_{MS}$  and  $X_{MS}$ . The subscripts  $MS$  refer to the multilayered strand where the force equilibrium takes all layers into account. The force equilibrium describing the whole strand is a statically undetermined problem.

*What is the line-contact force  $P_{MS_i}$  for two adjacent wires within wire layer  $i$  when all layers are taken into account for the statically indeterminate problem.*

When moving from the outside layer  $i = 1$  into the next one,  $i = 2$ , there is a radial force acting on layer  $i = 2$ . This radial force can be determined with [7]. It results from the helical trying to straighten due to the strand tensile strain  $S'_2$ , as they restrict each others movement forces result from one layer onto another (moving outward inward) in the strand radial direction:

$$\boxed{1.} \quad X_{RC} = \frac{EAS_1 \sin^2 \alpha}{r} \quad (53)$$

Here  $r$  is the helix radius. This relation has been derived geometrically with the assumption that:

*Wires carry only pure tension.*

It is stated in [23] that not only does each wire layer  $i$  have a certain  $P_{RC_i}/X_{RC_i}$  ratio, the ratio also changes for different strand tensile strains  $S'_1$ . It is therefore necessary to calculate the  $P_{RC_i}$  and  $X_{RC_i}$  forces for each tensile strain perturbation for each layer and use their ratio to determine the multi-strand line contact force  $P_{MS}$ . The resulting radial force  $X_{R_i}$  can finally be determined and the next layer can be evaluated. Note that  $P_{MS_i}$  in each layer is important for the dynamic model including friction.

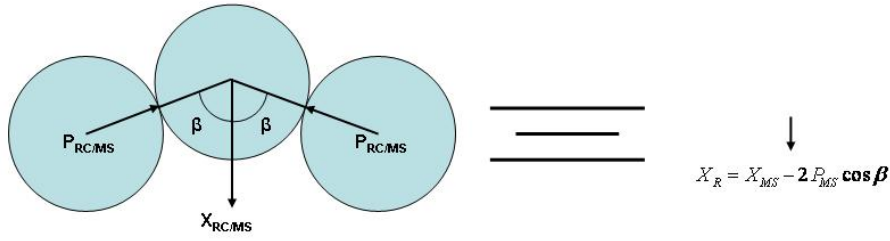


Figure 61: Forces,  $P_{RC/MS_i}$  and  $X_{RC/MS_i}$ , acting on the wire center (left) and the resultant force  $X_{R_i}$  (right).

First, the acting forces due to tensile tension are evaluated in the outside layer of the strand. In this layer  $P_{RC_1} = P_{MS_1}$  and  $X_{RC_1} = X_{MS_1}$  and one then continues to move further inside each time evaluating the forces in layer  $j = i + 1$ . The radial force  $X_{R_i}$  of the previous layer is added to the radial force  $X_{RC_j}$  of the next layer according to:

$$2. \quad X_{MS_j} = X_{RC_j} + X_{R_i} \frac{n_i \cos \alpha_j}{n_j \cos \alpha_i} \quad (54)$$

The line contact force  $P_{MS_j}$  can now be determined with the force ratio's within layer j:

$$3. \quad P_{MS_j} = \frac{P_{RC_j} X_{MS_j}}{X_{RC_j}} \quad (55)$$

By looking at figure 61 it can be easily seen that there is a resultant radial force  $X_{R_i}$  in layer i acting onto the next layer j according to:

$$4. \quad X_{R_j} = X_{MS_j} - 2P_{MS_j} \cos \beta \quad (56)$$

With the resultant radial force  $X_{R_j}$ , the next wire-layer  $j + 1$  can be analyzed. Starting with equation 53 to then take again the radial force into account of the previous wire layer  $j$ , yielding  $X_{MS_{j+1}}$  and so on.

With  $P_{MS_i}$  known for every wire layer  $i$ , the friction force  $F_{fric_i}$  can be determined with the friction factor  $\mu$ :

$$F_{fric_i} = \mu P_{MS_i} \quad (57)$$

## B.4 OST Compliances

### OST compliances

The strain tensor relation within a wire-layer has the form:

$$\begin{bmatrix} S_1 \\ S_2 \\ S_6 \end{bmatrix}_i = \begin{bmatrix} S_{11} & S_{12} & 0 \\ S_{12} & S_{22} & 0 \\ 0 & 0 & S_{66} \end{bmatrix}_i \begin{bmatrix} T_1 \\ T_2 \\ T_6 \end{bmatrix}_i \quad (58)$$

The compliances need to be known, thus:

What are the compliances  $S_{mn}$  of the orthotropic strain tensor for each wire layer  $i$ .

The OT is determined for a cylindrical shell. The gross area  $A_{gross,i}$  for each shell  $i$  is approximated by approaching each wire as a square with sides equal to the diameter  $D_1$  or  $D_2$  of the wire. In order to conserve the effective longitudinal stiffness of a wire layer,  $k_{wl}$ , the area ratio needs to be taken into account by determining a Young's Modulus  $E_{gross}$  compliant with this stiffness. The stiffness per unit length of a wire-layer  $i$  in the direction of orthotropy is  $k_{wl} = E_{steel}A_{net,i}$ . Thus to conserve this stiffness, the relation between *gross* and *net* it can be written that:

$$\frac{E_{gross}}{E_{steel}} = \frac{A_{net,i}}{A_{gross,i}} = \frac{\pi}{4} \quad (59)$$

According to *Hooke's law*, tensor compliances  $S_{11}$  and  $S_{12} = S_{21}$ , in the direction of the wire axis and the coupling compliance of approaching wire centers and the wire axis respectively, in the OT are now;

$$\boxed{1.} \quad S_{11} = \frac{1}{E_{gross}} = \frac{4}{\pi E_{steel}}, \quad (60)$$

and,

$$\boxed{2.} \quad S_{12} = -\frac{\nu}{E_{gross}} = \frac{4\nu}{\pi E_{steel}} \quad (61)$$

To determine the compliance in diametral direction,  $S_{22}$ , the Hertz contact theory is applied as in section B.3 where it is applied for the line-contact force  $P_{RC}$ . The resulting equation 51 is to be used here. This equation determines  $\delta_n$ . The associated line-contact force here is  $P_{MS}$ . As explained in appendix B.3,  $P_{MS}$  is the line-contact force where the forces from outer layer *are* taken into account. A change in diametral deflection  $\delta_n$  is realized by a change in line-contact force  $P_{MS}$ . The magnitude of the change in deflection  $\delta_n$  depends also on the deflection that has already occurred. The diametral deflection  $\delta_n$  thus also depends on the wire center distances. The compliance  $S_{22}$  can be derived as follows, where  $C_1$  and  $C_2$  are shown in equation 52a and 52b respectively:

$$\boxed{3.} \quad S_{22} = \frac{2}{D_1 + D_2} \frac{d\delta_n}{d\left(\frac{2P_{MS}}{D_1 + D_2}\right)} = \frac{1}{E_{steel}} \left( C_1 - \frac{1}{2}C_2 + C_2 \ln \sqrt{\frac{E_{steel}(D_1 + D_2)}{P_{MS}}} \right) \quad (62)$$

The tangential compliance  $S_{66}$  relates the shear stress  $T_6$  to the shear strain  $S_6$ .

In [23] it is explained in more detail that in [5] the case is considered of a force  $T$  acting in a plane. This force  $T$  is parallel to the principal axis of an elliptic contact and is monotonically increasing. In the case of inter-wire slippage it is the friction force  $F_{fric}$  acting in the direction of the inter-wire line contact.

When inter-wire slip occurs under a normal line contact force  $P_{MS}$ , the tangential force assumed as  $F_{fric} = \mu P_{MS}$  is reasonable. The coefficient  $\mu$  is the friction factor.

The author further explains that [10] evaluated constant displacement. One of the results is the following equation for cylinders sliding tangentially. In this relation,  $G$  is the shear strain,  $a$  is the length of

the contact area:

$$\Delta_l = \frac{3\mu P_{MS} (2 - \nu)}{16Ga} \left[ 1 - \left( 1 - \frac{T}{\mu P_{MS}} \right)^{\frac{2}{3}} \right] \xi \quad (63)$$

The term represented by  $\xi$  depends on the geometry of the two bodies in contact. This term is derived later in this section. Now the tensorial shear strain compliance  $S_{66}$  is given as:

$$S_{66} = \frac{d(2\Delta_l)}{dT} = \frac{2 - \nu}{4Ga} \left( 1 - \frac{T}{\mu P_{MS}} \right)^{-\frac{1}{3}} \xi \quad (64)$$

When full slip occurs, the wires are considered to slide with respect to each other as rigid bodies. The tangential force, or in this case friction force is then  $F_{fric_i} = \mu P_{MS_i}$ . Applying this to equation 63, yields the maximum wire slippage  $\Delta_{l_{max}}$ . Beyond this point the friction force remains equal to  $\mu P_{MS_i}$ :

$$\Delta_{l_{max}} = \frac{3\mu P_{MS} (2 - \nu)}{16Ga} \xi \quad (65)$$

By now substituting equation 65 into equation 63, a relation is made between the inter-wire slippage  $\Delta_l$  and the line-contact force  $P_{MS}$ :

$$\Delta_l = \Delta_{l_{max}} \left[ 1 - \left( 1 - \frac{T}{\mu P_{MS}} \right)^{\frac{2}{3}} \right] \quad (66)$$

For plane strain and no slip  $T = 0$ :

$$S_{66} = \frac{S_{22}}{1 - \nu} \quad (67)$$

When no slip  $T = 0$  in equation 64 combining with equation 67 yields:

$$\xi = \frac{4Ga S_{22}}{(2 - \nu)(1 - \nu)} \quad (68)$$

Substituting equations 68 and 66 into equation 64

**4.** 
$$S_{66} = \frac{S_{22}}{1 - \nu} \left( 1 - \frac{\Delta_l}{2\Delta_{l_{max}}} \right) \quad (69)$$

## B.5 Strand hysteresis under cyclic loading

In appendix B.4 the shear compliance  $S_{66}$  of the strain tensor of the wire-layer is derived. One outcome of the steps in deriving these, equation 66, can be rewritten to describe the hysteresis loop.

$$T = \left[ 1 - \left( 1 - \frac{\Delta_l}{\Delta_{l_{max}}} \right)^{\frac{3}{2}} \right] \mu P_{MS} \quad (70)$$

The surface area enclosed by this loop is the energy dissipated in the stick-slip region, blue loop in figure 62. When  $\Delta_l > \Delta_{l_{max}}$ , the sliding wires are in the gross-slip region and the tangential force  $T$  is at its maximum, see horizontal part in figure 62.

The energy dissipated in the full-slip region is the surface area enclosed by the green loop minus the

energy dissipated in the stick-slip region.

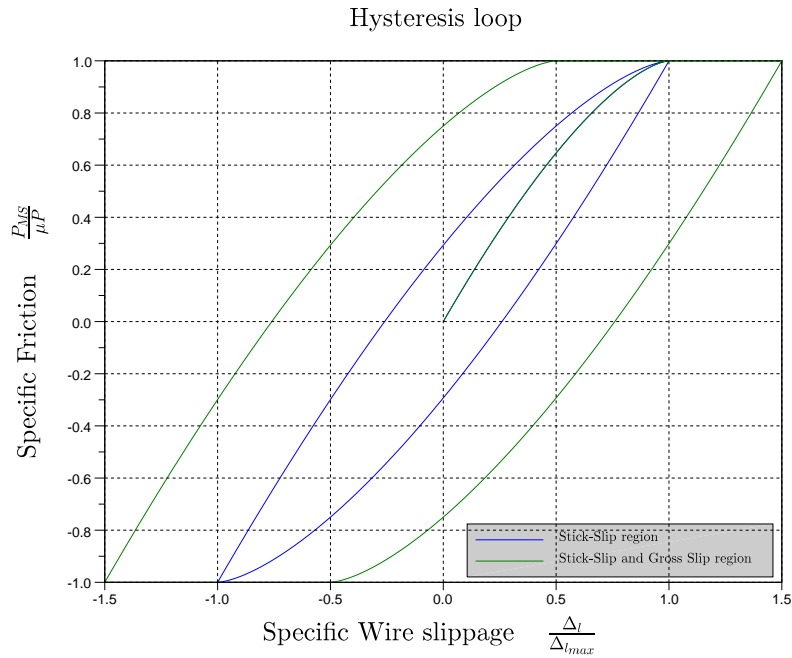


Figure 62: Hysteresis loop as applied in the OST.

**Wire slippages**

The wire slippage used for the dynamic model are the relative movements between adjacent wires within the same layer:

What is the relative (maximum) wire slippage within a wire layer of a strand subjected to a tensile strain  $S_1^t$ .

Combining equations 65 and 68 from appendix B.4 yields a relation to determine the maximum wire slippage  $\Delta_{l_{max}}$ . This slippage refers to the point when the frictional force  $F_{fric}$  reaches its maximum. It is determined with respect to the mean tensile load when the load is cyclic:

1. 
$$\Delta_{l_{max}} = \frac{3\mu P_{MS} S_{22}}{4(1 - \nu)} \tag{71}$$

Recall that in appendix B.2 it is explained that the tensorial shear strain  $S_{6T} = \frac{1}{2}\gamma$ . It is also shown that the wire slippage  $\beta = D'\gamma$ . Combining these relations yields:

$$\beta = 2D'S_{6T} \tag{72}$$

Now the wire slippage  $\Delta_l$  to be used is approximated with the undeformed wire diameter:

2. 
$$\Delta_l = 2DS_{6T} \tag{73}$$

**Energy dissipation per cycle**

Each load perturbation around a mean load has an associated specific energy dissipation  $\psi$ .

*How much energy  $\Delta U$  is dissipated in a strand subjected to a tensile load perturbation around a mean load for one cycle and what is the resulting specific energy dissipation  $\psi$ .*

The cyclic tensile load with amplitude  $\frac{\text{Load Range}}{2}$  does work on the wire rope, unit  $Nm = J$ . This work is the energy input to deform a wire rope element of length  $L_{mean}$  to  $L_{mean} + dL$ . It is thus the applied load times the displacement. Here  $L_{mean}$  is the length of the wire rope subjected to the mean load and  $dL$  is the change in length due to the load perturbation. For a wire rope with stiffness  $k_{wr}$  this means integrating the applied load,  $\frac{\text{Load Range}}{2}$ , over the displacement  $x = [0, dL]$ , thus.

$$\begin{aligned} U_{cycle} &= \int_0^{dL} k_{wr} dx \\ &= \frac{1}{2} k_{wr} dL^2 \end{aligned} \quad (74)$$

The input in the OST to determine the specific damping is the wire rope tensile strain  $S'_1$ . The tensile strain associated with the mean load is  $S'_{1,mean}$  where  $dS'_1$  is associated with the load perturbation. The stiffness and Youngs modulus of the wire rope per unit length are,

$$k_{wr} = E_{wr} A_{wr} \quad (75)$$

$$E_{wr} = \frac{\text{Load Range}}{2A_{wr} dS'_1} \quad (76)$$

First note that  $dL = dS'_1 L$  By now substituting equation 76 into 75 and substituting the result into equation 74, the total elastic energy for one cycle around a mean tensile load per unit length ( $L = 1$ ) is:

$$\mathbf{1.} \quad U = \frac{1}{2} \left( \frac{\text{Load Range}}{2} \right) dS'_1 \quad (77)$$

For each inter-wire slippage within a layer, the energy dissipation  $\Delta E$  can be determined by taking the surface area enclosed by the hysteresis loop, see figure 37. This energy dissipation has been derived in [10], as stated in [23]. The energy dissipation in the stick-slip region for two parallel cylinders can be derived with  $\xi$  of equation 68. The energy dissipation in the gross-slip region is the surface of a parallelogram equaling the surface of a square with sides  $2\mu P_{MS}$  and  $2(\Delta l - \Delta l_{max})$ :

$$\mathbf{2.} \quad \Delta E_i = \begin{cases} \frac{18\mu^2 P_{MS_i}^2 S_{22}}{5(1-\nu)} \left[ 1 - \left( 1 - \frac{T'}{\mu P_{MS_i}} \right)^{\frac{5}{3}} - \frac{5}{6} \frac{T'}{\mu P_{MS_i}} \left( 1 + \left( 1 - \frac{T'}{\mu P_{MS_i}} \right)^{\frac{2}{3}} \right) \right] & \text{if } \Delta l_i < \Delta l_{max_i} \\ \frac{3}{5} \frac{\mu^2 P_{MS_i}^2 S_{22}}{1-\nu} + 4\mu P_{MS_i} (\Delta l_i - \Delta l_{max_i}) & \text{if } \Delta l_i \geq \Delta l_{max_i} \end{cases}, \quad (78)$$

The total energy  $U$  is determined in the direction of the strand axis. The wire-layer is under a lay-angle  $\alpha$ . Therefore the dissipated energy  $\Delta E$  is a component of the resolved dissipated energy  $\Delta U$  in strand



axis direction. Taking this into account and summing over all wire layer yields:

$$\boxed{3.} \quad \Delta U = \sum_{i=1}^N \frac{n_i \Delta E_i}{\cos \alpha_i} \quad (79)$$

The specific energy dissipation per unit length for a strand is thus:

$$\boxed{4.} \quad \psi = \frac{\Delta U}{U} \quad (80)$$

## B.6 Strand's Young's Modulus

### Young's modulus of strand

A strand is constructed of helical wires. When a strand is under tension, due to the helical wires, the strand will also twist,  $\Gamma$ . Recall from appendix A.2 the length of a helix given in equation 28. The change in lay-angle  $\alpha$  is negligible thus  $\alpha' \approx \alpha$ . Equation 28 can be rewritten for the polar angle  $\phi$  for the deformed and undeformed situation. The change in polar angle  $d\phi$  due to tensile strain is then:

$$d\phi = \frac{dL}{dr\sqrt{1 + \cot^2 \alpha}} \quad (81)$$

From equation 81 it can be seen that twist will clearly result from tensile strain, or, when the ends are not permitted to rotate, torsional energy will be built up. There is thus a coupling between twist and tensile strain. The constitutive equations for a wire rope are postulated, in e.g [7], [26] and [40]. Herein,  $T$  and  $M$  are the tensile stress and twisting moment respectively and  $\epsilon$  and  $\Gamma$  are the tensile strain and twist per unit length respectively:

$$\frac{T}{E_{steel}} = d_1 \epsilon_{wr} + d_2 \Gamma_{wr} \quad (82a)$$

$$\frac{M}{E_{steel}} = d_3 \epsilon_{wr} + d_4 \Gamma_{wr} \quad (82b)$$

The constitutive constants describing the twist-tensile strain coupling should be equal due to symmetry,  $d_2 = d_3$ . Though due to assumption in the OST, and other theories, a discrepancy arises. It results from the various assumptions whereon the theories are based.

For the case investigated in this thesis, only tensile tension and no twist and is considered. There is here no interest in the torsional energy built up nor is there twist allowed. Equation 82b thus reduces to:

$$\frac{T}{E_{steel}} = d_1 \epsilon_{wr} \quad (83)$$

According to *Hearmon's notation* [17], the strain tensor with respect to wire rope axes is:

$$\begin{bmatrix} S'_1 \\ S'_2 \\ S'_6 \end{bmatrix}_i = \begin{bmatrix} S'_{11} & S'_{12} & S'_{16} \\ S'_{12} & S'_{22} & S'_{26} \\ S'_{16} & S'_{26} & S'_{66} \end{bmatrix}_i \begin{bmatrix} T'_1 \\ T'_2 \\ T'_6 \end{bmatrix}_i \quad (84)$$

The compliances of the strain tensor with respect to a wire layer have been determined in appendix B.4. For each wire layer these compliances can be transformed to the wire rope reference frame. This can be accomplished with [17]:

$$\begin{aligned}
 S'_{11} &= m^4 S_{11} + 2m^2 n^2 S_{12} + n^4 S_{22} + m^2 n^2 S_{66} \\
 S'_{12} &= m^2 n^2 S_{11} + (m^4 + n^4) S_{12} + m^2 n^2 S_{22} - m^2 n^2 S_{66} \\
 S'_{16} &= -2m^3 n S_{11} + 2mn(m^2 - n^2) S_{12} + 2mn^3 S_{22} + mn(m^2 - n^2) S_{66} \\
 \text{1. } S'_{22} &= n^4 S_{11} + 2m^2 n^2 S_{12} + m^4 S_{22} + m^2 n^2 S_{66} \\
 S'_{26} &= -2mn^3 S_{11} - 2mn(m^2 - n^2) S_{12} + 2m^3 n S_{22} - mn(m^2 - n^2) S_{66} \\
 S'_{66} &= 4m^2 n^2 S_{11} - 8m^2 n^2 S_{12} + 4m^2 n^2 S_{22} + (m^2 - n^2)^2 S_{66}
 \end{aligned} \tag{85}$$

where  $m = \cos \alpha$  and  $n = \sin \alpha$

Recall that the ends are not permitted to rotate and thus the wire rope shear strain  $S'_6 = 0$ . Equation 84 can then be solved for the tensile stress-strain relation  $\frac{T'_1}{S'_1}$  for each wire layer  $i$ :

$$\text{2. } k_{11,i} = \frac{T'_1}{S'_1} = \left( S'_{11} + K_1 S'_{12} - \frac{S'_{16}}{S'_{66}} (S'_{16} + K_1 S'_{26}) \right)^{-1} \tag{86}$$

The stress-strain relation  $k_{11}$  ( $N/mm^2$ ) is developed for two adjacent wires. A wire layer  $i$  consisting of  $n_i$  wires contains an equal number of sets of adjacent wires. Thus,  $k_{11,i}$  needs to be multiplied with  $n_i$ . Next, it needs to be summed over the wire layers  $i = 1, \dots, N$ . For the OT, the area  $A_{gross}$  is used. This explains the factor  $\frac{4}{\pi}$  as shown in appendix B.4. Herein  $d_1$  represents the constitutive constant ( $mm^2$ ) for the axial direction of the strand, thus:

$$\text{3. } d_1 = \frac{4}{\pi E_{steel}} \sum_{i=1}^N A_{net,i} k_{11,i} + A_{core} \tag{87}$$

By looking at equation 83 it can be seen that for the pure tensile tension case, the effective Young's modulus can be determined finally as follows:

$$\text{4. } E_{eff} = \frac{E_{steel} d_1}{A_{gross}} \tag{88}$$

In appendix B.4 it is observed that the shear compliance of the wire layer  $S_{66}$  depends on the amount of wire slippage  $\Delta_l$ . When  $\Delta_l > \Delta_{l,max}$ , the adjacent wires experience full-slip and the friction force will be at its maximum,  $F_{fric,i,max} = \mu P_{MS_i}$ . It has been found that a value 1 is relatively infinite. Thus by setting  $S_{66} = \frac{S_{22}}{1-\nu}$  (no-slip) and  $S_{66} = 1$  (full-slip), both associated effective Young's Moduli can be calculated for different tensile load/strain perturbations.

## B.7 Validation of implemetation with Numerical Examples

A solid amount of papers have been written by M. Raof on the subject of OST for wire ropes. The papers contain examples with respect to axial stiffness and specific damping amongst others. These examples are accompanied with numerical examples that are gratefully used in investigating the cor-

rectness of the implementation of the OST. Though also different strands have been used for producing numerical results in the various papers, the most often analysed strand is a 39mm multilayered strand. The details of this strand are provided in table 3 in section 5.3.

### B.7.1 Validation

**Kinematic Relations** A *first* example is provided in the paragraph *Results* of [25]. A given strand tensile strain is  $S'_1 = 0.003$ . In this paper a relation is made by parameterisation resulting in a function  $\frac{S_1}{S'_1}(\alpha)$ .

A *second* example is provided in [27]. Here too, parameterisation has been performed in order to create shortcuts for calculating various strand properties. A given strand strain in this example is  $S'_1 = 0.002891$ . In this paper more numerical results are provided. For the first layer they are;  $S_1, \alpha'_1$  and  $S_{6T}$ , and for the second layer they are;  $S_1, \alpha'_1$

The percentage errors (%) of the results yielded by the Newton-Raphson I iteration developed for this thesis is compared with the numerical examples that are shown in table 5

	Percent Error (%)		
	$S_1$	$\alpha'_1$	$S_{6T}$
Reference [25]	0.250	NA	NA
Reference [27], layer 1	0.233	0.00736	0.0157
Reference [27], layer 2	0.00719	0.00736	NA

Table 5: Relative errors of implementation of Newton-Raphson for solving for line contact forces.

The magnitude of the percentage errors determined for the available numerical examples show that the Newton-Raphson solving the kinematical relations from appendix B.2 iteration has been performed successfully.

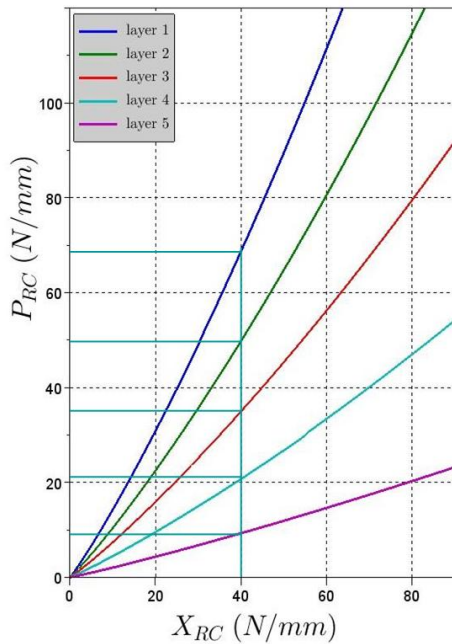
**Line Contact Forces  $P_{RC}$**  A numerical example is provided in the earlier mentioned paragraph *Results* of [25]. The result of the line contact force is given to be  $P_{RC} = 34.39(N/mm)$ . The Newton-Raphson iteration developed for this thesis yields  $P_{RC} = 33.34(N/mm)$  which translates into a percentage error of 3.053%.

In the paper [23], graphs are produced of intermediate results. These results are based on the 39mm strand with the construction data shown in table 3. Amongst others, plots of the  $P_{RC}$  data against the  $X_{RC}$  data for each wire layer  $i$  are provided. The data produced by the TP and of the reference [23] are shown in figure 63. The graphs in figure 63 compare very well. Moreover, the comparison of these graphs also indicates proper calculation of the radial force  $X_{RC}$ .

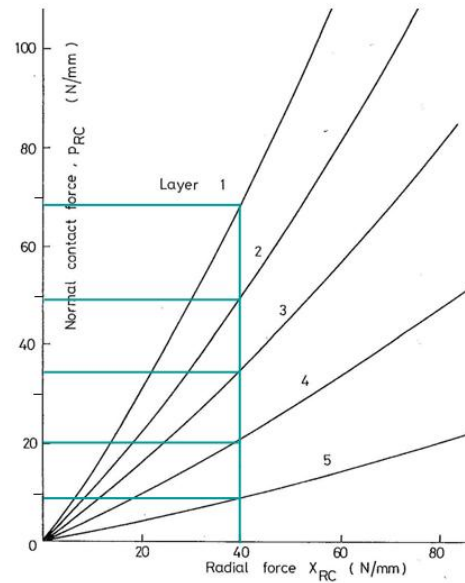
It can be concluded that the Newton-Raphson II iteration, as well as the calculation of  $X_{RC}$  data, has been performed successfully.

**Line Contact Forces  $P_{MS}$**  This is the line-contact force determined for each wire layer  $i$  with the effects of all layers taken into account. It is these forces that are used to determine the friction forces in the dynamical model,  $F_{fric} = \mu P_{MS}$ . The amount of friction with the associated contact surface

Line contact force vs radial force.



(a) Result produced by the TP.



(b) Result produced by M. Raouf in [23]

Figure 63:  $P_{RC}$  data vs  $X_{RC}$  data for a 39mm strand. The construction data can be found in table 3 taken from [23] and [26].

directly determines the amount of frictional energy.

In figure 64 the results of the TP are compared with data provided in [23]. For the outer layer  $P_{MS} = P_{RC}$  as there are no external forces acting upon this layer. The lines for layer one are thus expected to match and this is indeed the case. The the data don't match, one layer more or less than another, for all layers moving inward.

It can be seen in figure 64 that at  $P_{MS} = 50N/mm$  the second, third and fourth layer match fairly well. Layer five however is the worst match. Comparing the data at  $P_{MS} = 100N/mm$ , it can be seen that the match, except layer one, deteriorates even more. The  $P_{MS}$  data calculated by the TP is smaller than the data produced in [23]. It has not been found where the mismatch originates from. There is confidence that the radial load transfer from layer to layer, appendix B.3, has been properly understood and implemented.

The  $P_{MS}$  data will be used for calculating the frictional energy. The results from the heat conduction, section 6.2, show that the temperature change is very small, in the order of tenths of degrees. The relation between  $P_{MS}$  and surface temperature is fairly linear. Eventhough the match is not optimal with the shown example from [23], it is good enough to determine the scale of the frictional energy generation and the resulting temperature change on the surface of the wire.

**Specific damping in layers and for the whole strand**

The specific damping  $\psi$  per wirel layer appears to be smaller than the example from [24]. The characteristics however are fairly similar. The position of the maximum  $\psi$  for each wire layer appear to be

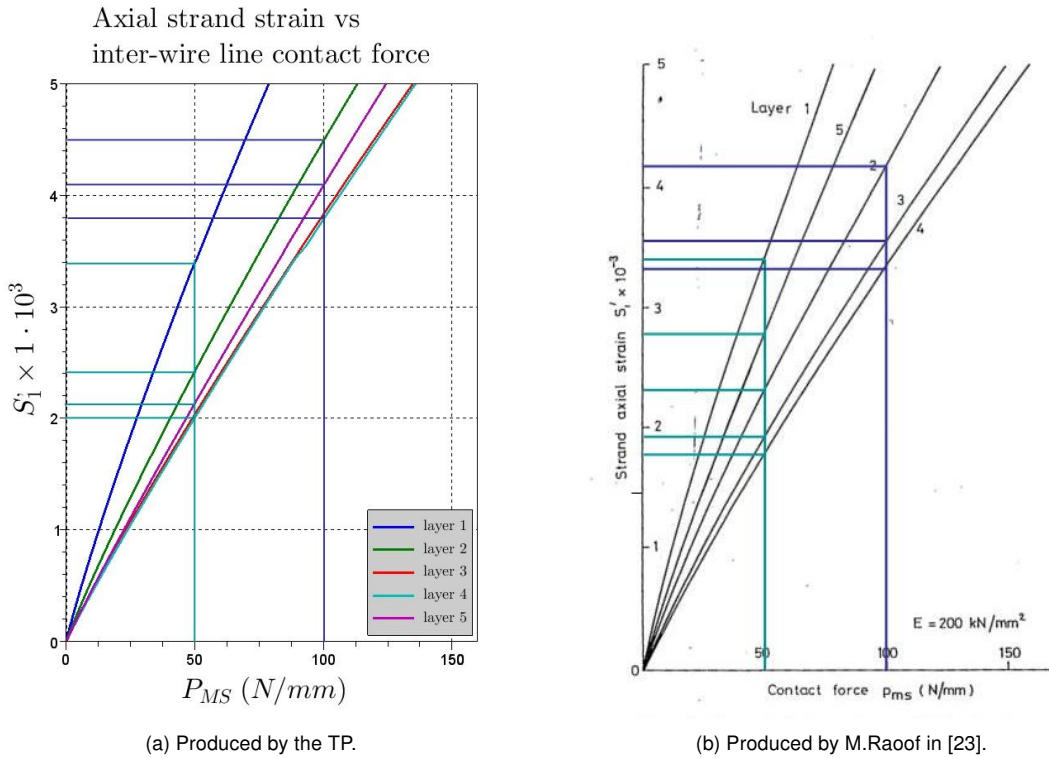


Figure 64: Plot of tensile strand strain  $S_1$  vs line contact force  $P_{MS}$  produced by the TP (left) and produced by M. Raof in [23] (right)

at similar load perturbations as in the example from [24]. Though this is hard to verify exactly with the plots provided.

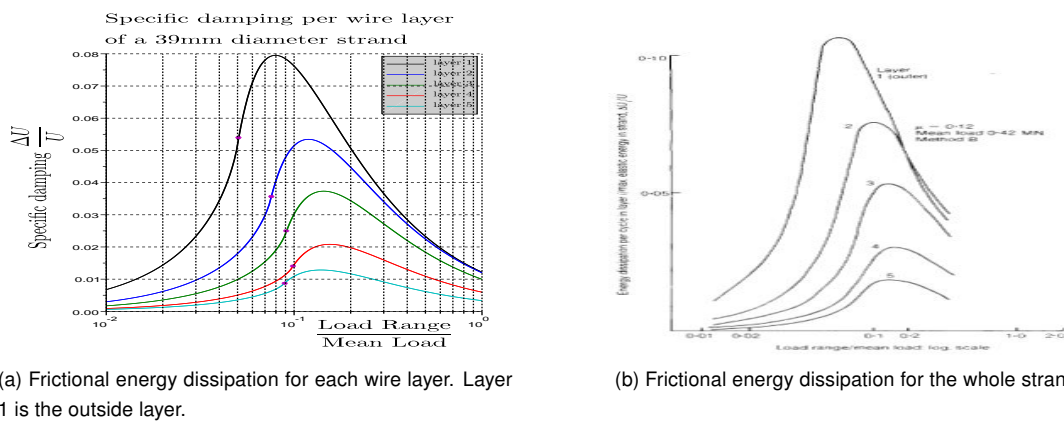


Figure 65: Frictional energy dissipation in a strand subjected to a mean tensile strand load of 0.42MN as a function of load perturbation.

M Raof has compared his theoretical results with experiments [24] (black spots). The results are shown in figure 66. Also shown in the figure is the result of the TP (blue line). The position of the peak

is provided for the specific of the whole strand. The peak from [24] is located at  $\frac{\text{Load Range}}{\text{Mean Load}} = 0.127$  where the peak determined by the TP is located at  $\frac{\text{Load Range}}{\text{Mean Load}} = 0.122$ .

The experimental results are very scattered. So even though there is no full compliance with the example of [24], it is good enough to determine the order of magnitude of the inter-wire frictional forces.

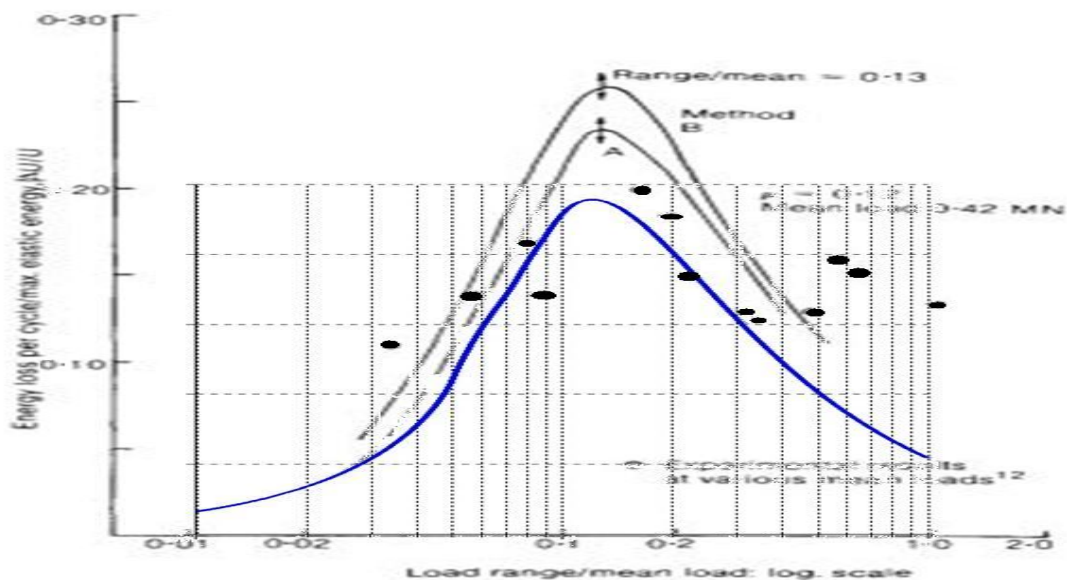


Figure 66: Results for the 39mm SSR by the TP and from [24].

**Effective Young's Modulus of strand** In section 5.3.1 results are shown for the effective Young's Modulus for the 39mm strand of table 3 for strains up to  $5e^{-3}$ , figure 40. In [27] it is mentioned that for a tensile strain of 0.002891, the associated effective Young's Modulus is  $149.4kN/mm^2$ . The TP yields for the same strain an effective Young's Modulus of  $157.5kN/mm^2$ . The difference is thus 5.4%. Also,  $E_{eff}$  has been determined in section 5.3.2 for a 40mm MSR. This example is taken from [29]. Therein, it is shown in a graph that the no-slip  $E_{eff}$  value for a mean load of  $250kN$  is  $124.0kN/mm^2$  and the full-slip value is  $107.4kN/mm^2$ . The no-slip value is associated with a tensile strain of  $S'_1 = 2.055e^{-3}$  in the TP. Applying this strain to calculate the tensile load yields  $F = 272kN$ . This is 8.7% higher than  $250kN$ . The associated full-slip value is  $107.8kN/mm^2$ , this is 0.37% higher than the example from [27]. The main error is thus the mean load.

**Inter-wire contact stress within a wire layer** An FEM model to determine, amongst others, inter-wire contact stresses is shown in [19]. It considers an 'ordinary strand' (one core wire and one wire-layer with six wires). All construction details are provided and a comparison can be made between the results of the FEM method applied in [19] and the OST.

In [19] the contact stress of the strand considered subjected to an axial strain of 0.0003 is given to be  $0.98GPa$ . The TP yields for the same strain and strand  $1.06GPa$ . The result yielded by the TP is 8% higher. It has not been investigated what the exact causes are of this difference. Nevertheless, it can be said that the results are very similar and are considered good.

### B.7.2 Conclusions

There are still differences between the results produced by the TP and the examples of various results provided in the papers of M.Raouf. When the scale of the differences is compared to the differences between theory and experiments, it can be said that the results produced are of the right magnitude. The main research question is whether temperatures can rise significantly to endanger the life of the wire rope. It *is* important to know whether the temperature change is in the order tens of degrees. It *is not* important to get an accurate value.

*The implementation of the OST is performed satisfyingly to determine the order of temperature change within the wire rope subjected to the tensile forces determined in [4].*





## C Friction

This appendix elaborates on friction. There are many types of friction models. The choice depends on what is investigated from a model. Take for example a mechanism which inevitably consist of parts that slide on each other thus causing friction forces. These friction forces can influence the dynamic behavior of the mechanism significantly. It is possible that a mechanism modelled without friction shows a stable behavior, though when friction is taken into account it can become unstable.

In this thesis what is asked from the friction model is to show the magnitude of the energies involved with inter-wire friction in a wire rope. As the friction forces are small compared to other influences (i.e. weight of the jacket), they are not expected to influence the dynamics of the wire rope.

A simple friction model is thus chosen. It is based on the well know Coulomb's dry friction model, appendix C.1. This simple model will be applied in the random like dynamic multiscale model described in section 6.1. For the homogenized model, steady state perturbation around a mean load as described in section 6.1.3, Masing's rule is applied, appendix C.2, too take stick slip behavior into account with the transition to full-slip.

### C.1 Coulomb's dry friction Law

This law encapsulates a complexity of interactions in one constant friction factor  $\mu$ . It is postulated that  $\mu$  linearly relates the normal force  $F_N$  acting between two surfaces to a resistive (frictional) force  $F_{fric}$  acting opposite in the direction of relative movement, figure 67.

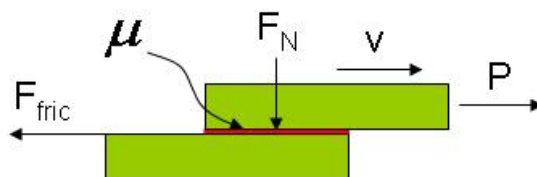


Figure 67: Schematical representation of Coulomb's law.

A distinguishment is made between two types of friction factors, *static* and *kinetic*. Static friction is the force that resists any relative motion between two bodies. When the point is reached that the static force is no longer sufficient to resist relative motion, the kinetic friction comes into play which is the resistive force of two bodies *with* relative motion. This distinguishing is made because it has been found that i.e it may take less force to retain a motion with sliding surfaces than it takes to create motion in the first place.

Note that in the following mathematical expression of Coulomb's law the external force  $P$  has no resulting motion as it is smaller than:

$$F_{fric} = \begin{cases} \mu F_N \cdot \text{sgn}(v) & |P| \geq \mu F_N \\ -P & |P| < \mu F_N \end{cases} \quad (89)$$

## C.2 Masing's Rule

Here the hysteresis loop is shown as applied in the TP.

$$F_{fric,t_n} = \begin{cases} \mu F_N \cdot \text{sgn}(v), & |\Delta_{l,t_n}| \geq \Delta_{l_{max}} \\ \frac{\mu F_N}{\Delta_{l_{max}}} \cdot (\Delta_{l,t_n} - z) \cdot \text{sgn}(v), & |\Delta_{l,t_n}| < \Delta_{l_{max}} \end{cases} \quad (90)$$

where,  $z = \Delta_{l,t_{n-1}} - \frac{F_{fric,t_{n-1}}}{\mu F_N \cdot \Delta_{l_{max}}}$

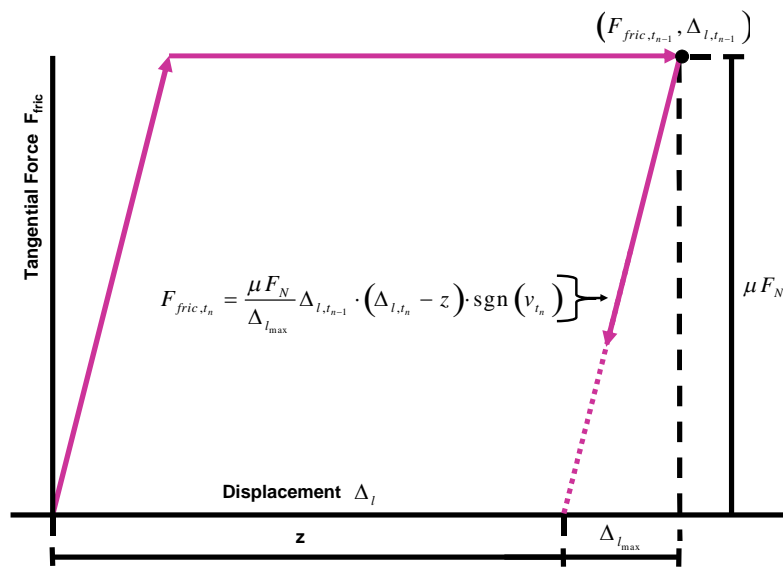


Figure 68: Graphical representation of function accomodating for stick-slip behavior.

## D Dynamic Modeling

Two FE models of the wire rope have been developed for this thesis. *First* a linear model has been developed. It considers the homogenized approach and is described in appendix D.1. *Second* a non-linear model has been developed. It considers the multiscale  $FE^2$  approach and is described in appendix D.2.

In figures 69 and 72 it can be seen that the wire rope is modeled as being attached at the top and having a free end at the bottom. At the top end, in the actual situation the wire rope is running over several sheaves. At the free-end, the loads are applied that have been calculated by the ADAMS model developed by [4]. There is thus no interaction with the sheaves nor bending of the wire ropes taken into account. Also there is no feedback of the dynamic response of the wire rope back into the jacket and thus the rest of the system considered. Furthermore the load applied on the wire ropes are actually under an angle, though for this thesis only the resultant loads in the axial direction of the wire rope have been considered. A possible effect that has consequently been left out is that of *whipping*. Summarizing, the following assumptions have thus been made for both models:

- The influence of the axial dynamic response of the wire rope on the rest of the system is negligible.
- The effects of wire ropes running over sheaves have a negligible effect on the axial dynamic response of the wire rope.
- The off-axis external forces have negligible effect on the axial dynamic response of the wire rope and thus whipping remains uninvestigated.

For both wire rope models the *Newmark Method* has been implemented to perform the time integration. This method is described in more detail in [34]. For the *homogenized* model in appendix D.1, the linear variant has been applied. For the *multiscale  $FE^2$*  model in appendix D.2, the non-linear variant has been applied.

### D.1 Homogenized Model

The homogenized model considers the situation where there is a cyclic axial load perturbation around a mean mean load acting on the wire rope. It has been shown in section 5 (and appendix B) that around this mean load, a constant specific damping  $\psi$  and wire rope Young's modulus  $E_{eff}$  can be determined. When the applied load is a steady state cyclic perturbation around the mean axial load, the specific damping  $\psi$  can be transformed to an equivalent viscous damping  $c_{eq}$ .

#### D.1.1 Mathematical model

Each element consists of a point mass, a dashpot (viscous damping) and a linear spring, see figure 69. The differential equations describing the dynamics of this system can be represented in vector notation as:

$$\mathbf{M}\ddot{\mathbf{x}} + \mathbf{C}\dot{\mathbf{x}} + \mathbf{K}\mathbf{x} = \mathbf{F}_{ext} \quad (91)$$

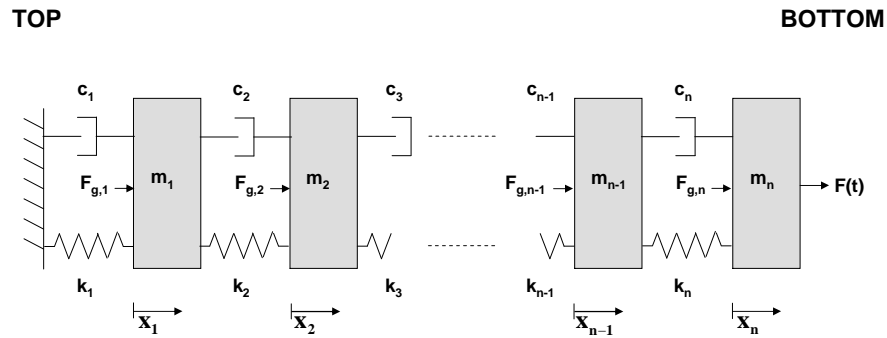


Figure 69: FEM of wire rope with viscous damping between the wire rope elements

### D.1.2 Solving Dynamic Model

**Linear Newmark Intergration  $\beta$  method** The *Linear Newmark Integration* method is described in more detail in [34]. It is predictive-corrective numeric integration scheme developed for linear differential equations of the form:

$$\mathbf{M}\ddot{\mathbf{x}} + \mathbf{C}\dot{\mathbf{x}} + \mathbf{K}\mathbf{x} = \mathbf{F}_{\text{ext}}(t) \quad (92)$$

The approach is that a *Taylor series expansion* is made of the displacements and velocities of a time dependent function  $f(t_n)$ . The resulting expansion allows for calculation of the velocity and displacement states at time  $t_{n+1} = t_n + h$ , where  $h$  is the timestep. The calculation involves integral terms of the acceleration. These accelerations are approximated with numerical quadrature. It is here that the coefficients  $\gamma$  and  $\beta$  are introduced, see [34]. They are introduced in such a way that when  $\gamma = 0$  and  $\beta = 0$ , the numerical time integration scheme reduces to the purely explicit form.

The constant average acceleration method,  $\gamma = \frac{1}{2}$  and  $\beta = \frac{1}{4}$ , is chosen for this thesis. It is associated with zero amplitude error and a periodicity error of  $\frac{\omega^2}{h^2}$  where  $\omega$  is the first Eigen Frequency of the system. The zero amplitude error is important as the amplitude of the response is directly linked to the inter-wire slippage. Furthermore, this method is *unconditionally stable*, meaning the choice in timestep size is free. It is stressed, however, that to incorporate the contribution of the highest frequency oscillator, the timestep is generally taken as  $h \leq \frac{T}{4}$  [34], where  $T$  is the period of the expected free oscillation.

The numerical scheme is depicted in figure 70

**Implementation** The wire rope properties, stiffness  $k$  and damping  $c$ , are kept constant in this model. The stiffness  $k$  of each element is determined with the wire ropes' Young's modulus  $E_{\text{eff}}$ , the cross-section  $A_{\text{wire rope}}$  and the element length  $L_{\text{el}}$ . The stiffness of the wire rope actually varies per unit length. It is thus discretized in the model by dividing the wire rope into a number of elements where the Youngs' modulus is replaced by an equivalent stiffness associated with the length of the element:

$$k = \frac{E_{\text{eff}} A_{\text{wire rope}}}{L_{\text{el}}} \quad (93)$$

A consequence of discretizing is that the *Eigen Frequencies* of the wire rope become more accurate as the number of elements increases. For further modeling it is crucial to choose a minimum amount of

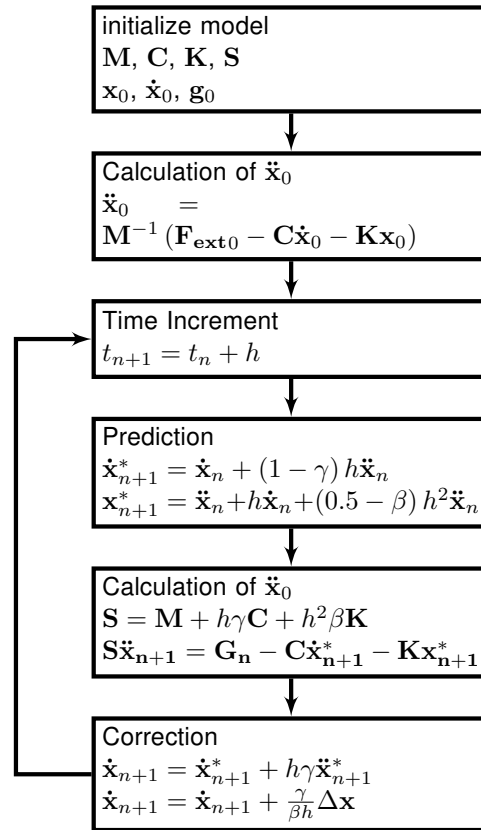


Figure 70: Scheme for Linear Newmark Intergration  $\beta$  method

elements due to the influence on computation time. A small algorithm has been written that calculates the Eigen Frequencies for  $i = 1, 2, \dots etc.$  elements. The relative difference between the first Eigen Frequencies of the wire rope built up of  $i$  and  $i - 1$  elements is used as a measure for approximation error. The iteration stops when  $error = \frac{abs(\omega(i) - \omega(i-1))}{\omega(i)} < 1e^{-2}(Hz)$ . The result is that according to this criterium the amount of elements to be used is 8, where the first Eigen Frequency is  $8.2Hz$ , figure 71.

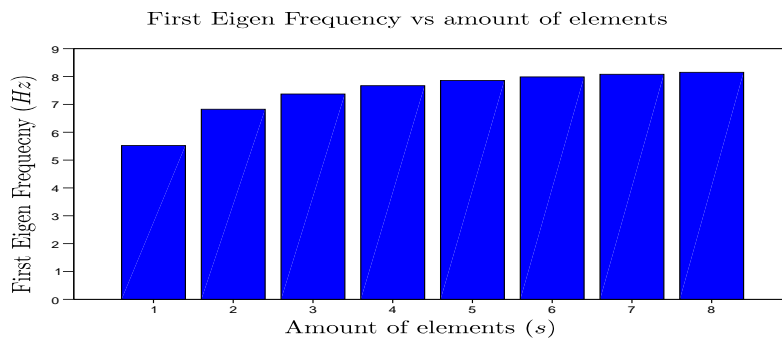


Figure 71: First Eigen Frequency for corresponding amount of elements.

The specific damping  $\psi$  is determined around a mean load with the OST as shown in section 5 and

appendix B. The specific damping can be replaced by an equivalent viscous damping  $c_{eq}$  that is valid at a single frequency load perturbation. The energy dissipation  $\Delta U$  for viscous damping and for frictional damping can be compared. The comparison results in an equivalent  $c$  being the only unknown, where  $\omega$  is the frequency of the sinusoidal load perturbation:

$$c = \frac{k\psi}{\omega} \tag{94}$$

All values are now known and the differential equations 91 can be solved with the *Linear Newmark Integration*  $\beta$  method in the time domain.

## D.2 Multiscale $FE^2$ Model

### D.2.1 Mathematical model

The difference with the homogenized model is that the viscous damping is replaced by the inter-wire friction forces. The mathematic model is thus now written as:

$$\mathbf{M}\ddot{\mathbf{x}} + \mathbf{F}_{friction} \text{sgn}(\dot{\mathbf{x}}) + \mathbf{K}\mathbf{x} = \mathbf{F}_{ext} \tag{95}$$

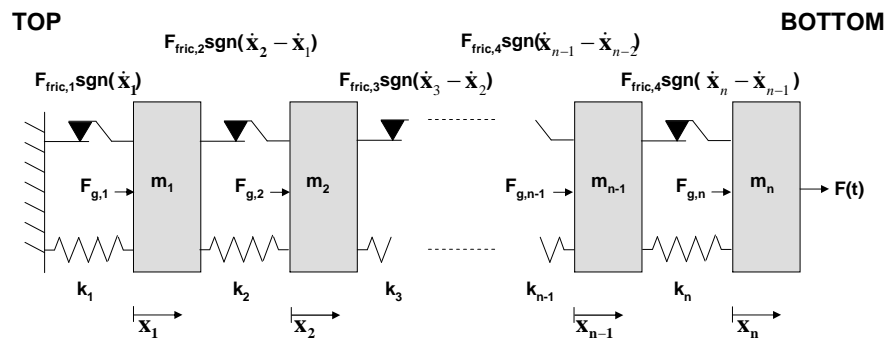


Figure 72: FEM of wire rope with frictional damping between the wire rope elements

### D.2.2 Solving Dynamic Model

**Non-Linear Newmark Intergration  $\beta$  method** The non-linear variant procedure is shown in figure 73. For detailed explanation it is referred to [34].

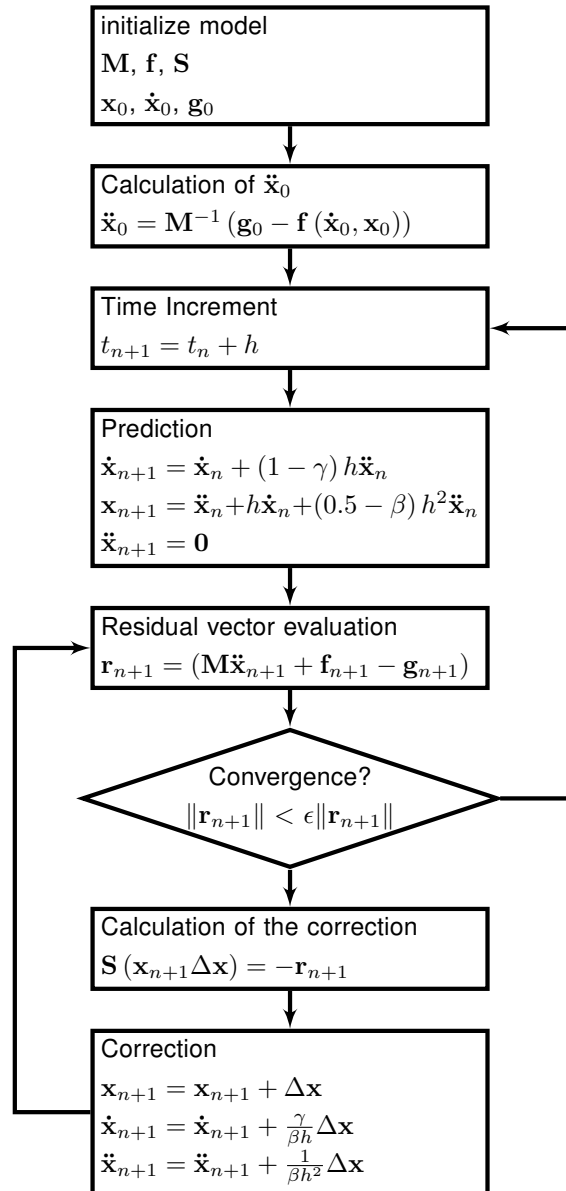


Figure 73: Scheme for Non-Linear Newmark Intergration  $\beta$  method.

**Implementation** In this thesis a multiscale FE<sup>2</sup> approach is used. One can define multiscale FE<sup>2</sup> as follows:

*The modeling where the interaction between the macro- and micro model is made.*

The inter-wire friction depends on the inter-wire slippage  $\Delta_l$ . The  $\Delta_l$  depends on the axial strain that on its turn is determined with the element positions  $\mathbf{x}$ . The inter-wire friction forces are thus a function of element displacement. Thus the OST yielding the microscopic behavior must be incorporated into the convergence loop, figure 74.

The resulting heat flux is not incorporated into the convergence loop. The results might indicate a significant change in temperature which will have an effect on the friction factor  $\mu$ . Because  $\mu$  will on its turn have a direct effect on the friction forces, the change in  $\mu$  will then have to be taken into account in the time integration. This will result in a multiscale FE<sup>3</sup> model. It is shown in section 6.2, however, that this is not the case.

Moreover, it is shown in section 6.1 that the inter-wire friction forces have negligible effect on the dynamic response of the wire rope. The OST can thus be taken out of the convergence loop as shown in figure 75. It is thus chosen to not apply a multiscale FE<sup>2</sup> approach where there is feedback from the microscale to the macroscale. This will save a significant amount of computing time. The results of the macroscale model are used for the microscale model to determine the heat flux.

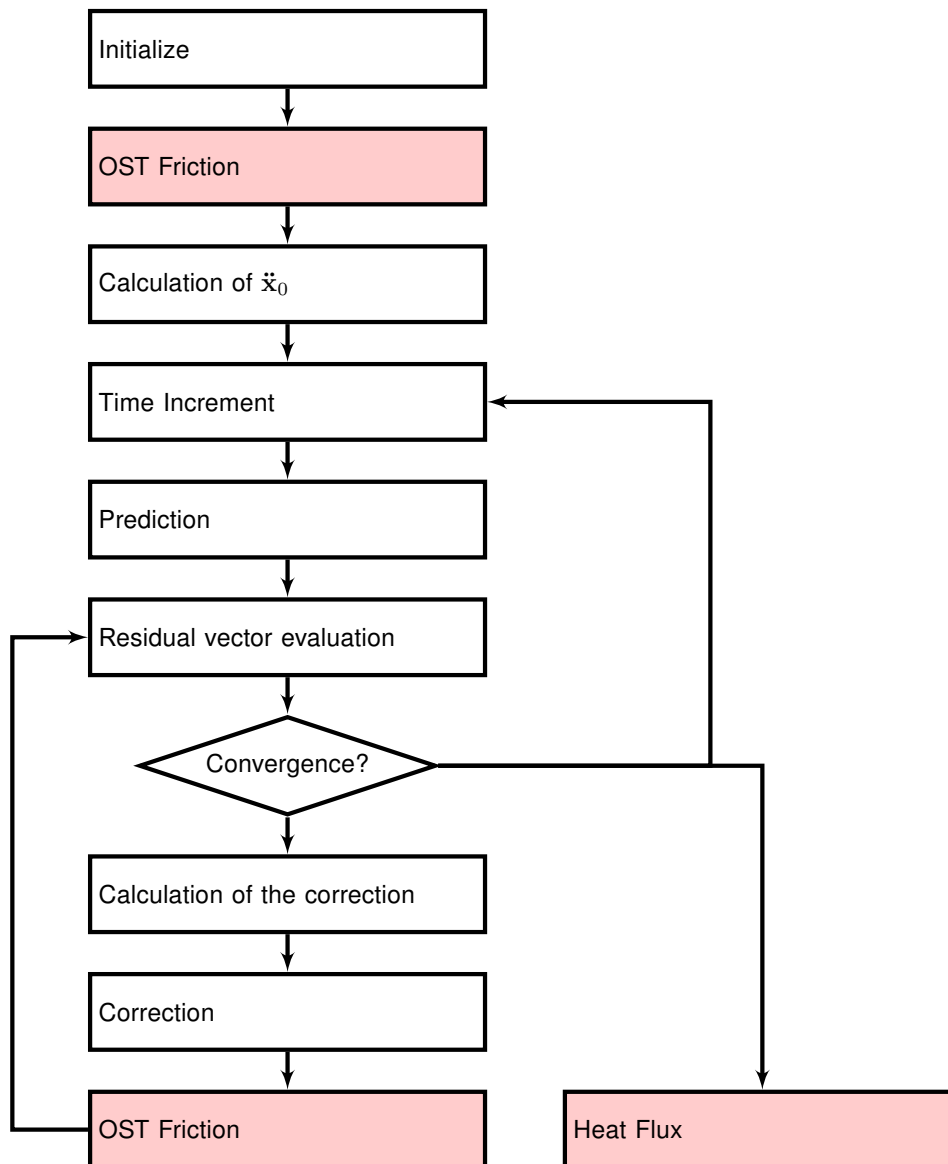


Figure 74: Scheme for Non-Linear Newmark Intergration  $\beta$  method where the OST yielding the microscopic behavior is implemented in the convergence routine.



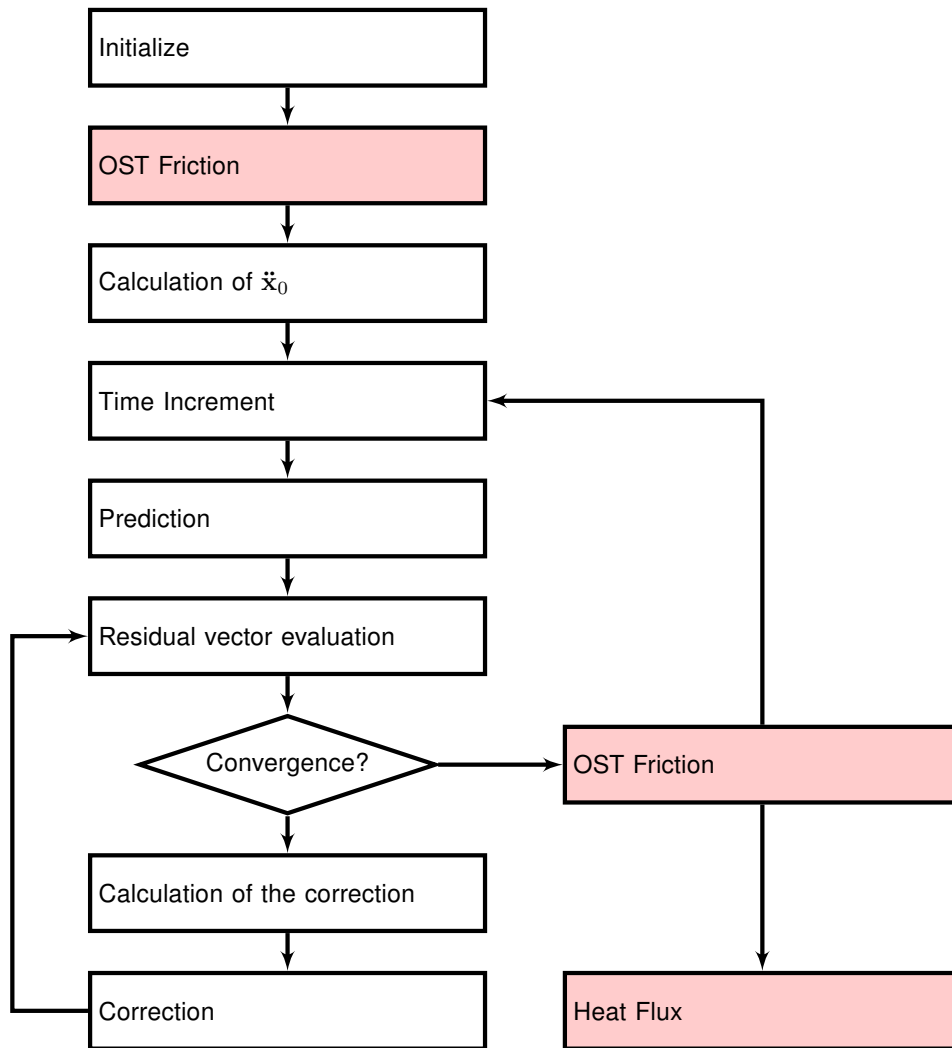


Figure 75: Scheme for Non-Linear Newmark Intergration  $\beta$  method where the OST yielding the microscopic behavior is kept outside the routine. It thus only yields the microscopic behavior as a consequence of the dynamic response but it does not influence the dynamic response.



## E Solving a set of non-linear functions

The subject of solving a set of non-linear functions is a very broad one. There are numerous methods and variations of methods and so forth. In this appendix only the chosen combination of methods will be described.

For the problems encountered in the OST, section B.2, the *Newton-Raphson method* is chosen for solving the root(s) problem of the (set of) non-linear function(s) in combination with the *Central Difference method*, a numerical differentiation method. Differentiation is a necessary step of the Newton-Raphson method.

### E.1 Newton-Raphson

This numerical method for finding the root(s) of a (set of) non-linear function(s) has first been developed by *Isaac Newton* and later been simplified by *Joseph Raphson*.

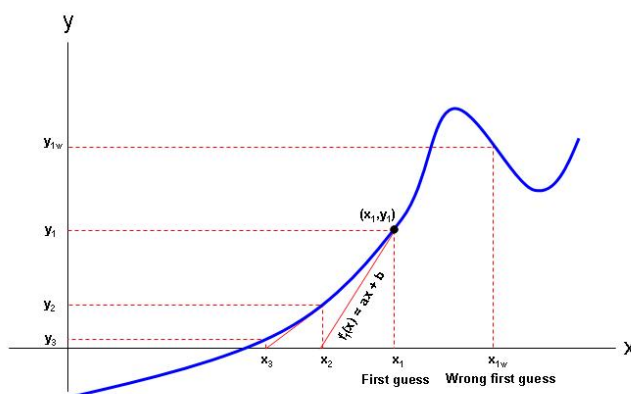


Figure 76: Graphical representation of Newton-Raphson method.

To visualize the method it is easiest to look at a function  $f(x)$  with one unknown as shown in figure 76. One starts with a guestimate,  $x_1$ , and evaluates the function for this point yielding  $y_1$ . The reasoning of this guestimate depends on the function and thus cannot be generalized. At the point  $(x_1, y_1)$  the slope needs to be determined so subsequently the line going through this point can be determined with slope  $a$  and offset  $b$  at  $x = 0$ :

$$f_1(x) = ax + b \tag{96}$$

It is clear that finding the root of this line is very straightforward. The root of this line will be the next point  $x_2$  where the function will be evaluated again and further the above described procedure will be performed. Doing this iteration  $i = 1, \dots, n$ -times, the root of the non-linear function can be approximated, see figure 76. Generalized, the method for a function of one variable can be written as:

$$x_{i+1} = x_i - \frac{f(x_i)}{f'(x_i)} \tag{97}$$

Expanding the method to a *set* of functions yields:

$$\delta_i = -[\mathbf{J}_i]^{-1} f_i, \quad x_{i+1} = x_i + \delta_i, \quad i = 0, 1, \dots, n \tag{98}$$

Where  $\mathbf{J}_i$  is the *Jacobian* of the set of functions evaluated at the  $i^{th}$  found root.

Conditions need to be chosen to limit the number of iterations. Two conditions must be applied.

*First*, at each iteration the function can be evaluated to check whether the answer is 'close enough' to zero. The last root will then be taken as the final solution. The words 'close enough' depend on the desired accuracy and computation time. A higher accuracy will result in longer computation time. One way to check for accuracy is to use the scale of the unknown(s) and a chosen tolerance that will evaluate what this accuracy actually is. In case of a function with only one variable the absolute value of the evaluation at the last found root  $x_i$  can be taken as a measure of accuracy. This value can be compared with a tolerance of a number representative of the scale inherent to the function. If the function depends on i.e. a force variable in the scale of kN's, then a fraction of a force representative of this scale can be taken as a condition. Expanding this to a set of functions, instead of one value the length of the vector containing the evaluations of each function at the last found root is used. Another way is to check for the difference between the  $i - 1^{th}$  root(s) and the  $i^{th}$  root(s). This value is multiplied with a chosen tolerance setting the threshold for the iteration to stop when the change in roots is below this threshold.

*Second*, a maximum number of iterations needs to be chosen to safeguard against non-convergence. This can happen when a 'wrong' first guestimate is determined, see figure 76. It is clear that a root will most probable not be found or at least not within an acceptable number of iterations.

## E.2 Central Difference method

The derivative of a function (or Jacobian for a set of functions) can be derived analytically or evaluated numerically. In case it is not possible or too cumbersome to determine the derive of the function analytically, there is a variety of numerical methods to approximate the slope at any point of the function. One of these methods is the *central difference method* which is easily implemented and very intuitive.

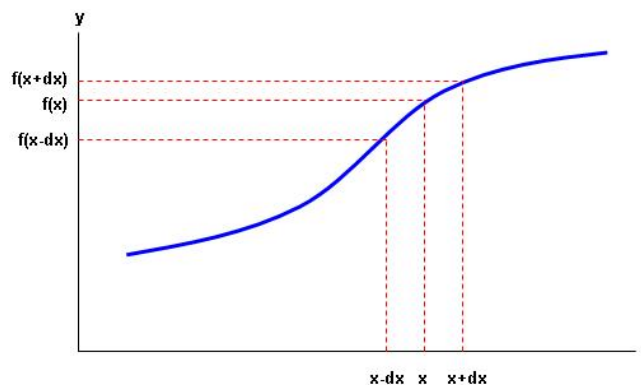


Figure 77: Graphical representation of Central-Difference method.

Let's again first look at a function of one variable. In words the central difference method evaluates the function 'just' before and after a point on the x-axis. The word 'just' refers to  $dx$  whose value can be reasoned depending on the characteristics of the function. The slope can then be calculated with these results as the difference in y-value and x-value is now known around this point, figure 77:

$$f'(x) = \frac{f(x+dx) - f(x-dx)}{2dx} \quad (99)$$

Expanding the method to a set of functions yields;

$$f'(x_1, \dots, x_n) = \begin{bmatrix} \frac{f_1(x_1+dx_1, x_2, \dots, x_n) - f_1(x_1-dx_1, x_2, \dots, x_n)}{2dx_1} & \dots & \frac{f_1(x_1, \dots, x_{n-1}, x_n+dx_n) - f_1(x_1, \dots, x_{n-1}, x_n-dx_n)}{2dx_n} \\ \vdots & \ddots & \vdots \\ \frac{f_n(x_1+dx_1, x_2, \dots, x_n) - f_n(x_1-dx_1, x_2, \dots, x_n)}{2dx_1} & \dots & \frac{f_n(x_1, \dots, x_{n-1}, x_n+dx_n) - f_n(x_1, \dots, x_{n-1}, x_n-dx_n)}{2dx_n} \end{bmatrix} \quad (100)$$

### E.3 Implementation in the OST

The solving of non-linear function(s) is done twice when implementing the OST. The *first* is the set of functions describing the kinematical relationships when a strand has a given strain  $S_1'$ , *Newton Raphson I*. The *second* is to solve the function for the line contact force  $P_{RC}$ , *Newton Raphson II*. The following two paragraphs describe shortly the guestimate for each of the Newton-Raphson method implementations and what the choices are with respect to accuracy and the size of the difference step for the Central-Difference method. Also results are compared with available numerical examples.

**Newton Raphson I** Investigating the set of functions describing the kinematical relationships, it is found that actually only one guestimate is needed, that of the helical wire axial strain  $S_1$ . This wire strain is always slightly less than the strand axial strain  $S_1'$ , approximately 5 - 15% less. Trial and error has shown that guestimating the wire axial strain at  $0.9S_1'$  is fairly good. With  $S_1$  evaluated, the remaining unknowns can be evaluated by choosing the right, noting there are several, sequence of the kinematical functions:

1.  $S_1 = 0.9S_1'$
2.  $\alpha' = \arccos\left(\frac{\cos \alpha(1+S_1')}{S_1+1}\right)$
3.  $S_{2R}' = \sqrt{\frac{\cos^2 \alpha(\cos^2 \alpha' + \tan^2 A)}{\cos^2 \alpha'(\cos^2 \alpha + \tan^2 A)}} - 1$
4.  $S_{2C}' = \frac{(1+S_1') \tan \alpha'}{\tan \alpha} - 1$
5.  $S_2' = S_{2C}' - S_{2R}'$
6.  $dS_1 = \cos \alpha \sqrt{1 + (1 + S_{2R}')^2 \tan^2 \alpha} - 1$
7.  $S_{6T} = \frac{(S_1' - S_2') \sin 2\alpha'}{2}$
8.  $S_2 = -\frac{(S_1' - S_2') \cos 2\alpha'}{2} + \frac{S_1' + S_2'}{2}$

Experience has learned that the first guestimate is very reasonable and thus to is also suited to be used as a reference value for accuracy and to determine a stepsize.

The length of the guestimate is thus taken as a reference value to check for accuracy. The tolerance is found to stop improving the accuracy significantly if  $tolerance < 1e^{-6}$ .

The step size for the Central-Difference method must be different for each unknown because they differ in order of magnitude. A fraction of the size of the first guestimate is chosen. The stepsize is found to reduce the number of iterations when chosen  $\frac{1}{100}^{th}$  of the guestimate. Making the stepsize larger does not seem to reduce the number of iterations any further.

A numerical example can be taken from [25]. The given resulting axial wire strain,  $S_1 = 0.00261$ , compares well to the result,  $S_1 = 0.002604$ , yielded by the TP. Furthermore, the length of the residual, deviation from zero of the nullified equations, for this example is  $1.471e^{-11}$  which is significantly less than the length of the final solution,  $0.003202$ . The lay angle is excluded as its order of magnitude is an order 100 - 1000 times larger than the other unknowns. For the lay angle the residual is  $-196.8e^{-14}rad$  which on its turn, too, is significantly less than the final solution for the lay angle of  $0.3129rad$ . This gives confidence in the correct implementation of *Newton Raphson I*.

**Newton Raphson II** As only the root of one function of one variable needs to be found, only one value needs to be guestimated here.

It is chosen to make a guestimate of line contact width  $b$  that depends on the wire diameter. With this guestimate, the guestimate of the line contact force  $P_{RC}$  can then be calculated. After some trial and error combined with the knowledge that the contact width is a fraction of the wire diameter, it is found that if  $b = \frac{D_{wire}}{100}$  only a few iterations are needed. From a numerical example given in [25], it is calculated that for this example  $\frac{\text{guestimate}}{\text{final answer}} = 0.962$  and thus is close to the 'true' (final approximated) answer. Therefor it is not felt necessary to find a better guestimate, thus:

$$\begin{array}{l} \boxed{1.} \quad b \quad = \quad \frac{D_{wire}}{100} \\ \boxed{2.} \quad P_{RC} \quad = \quad -\frac{\delta_n}{4(1-\nu^2)\left(\frac{1}{3} + \ln \frac{D_{wire}}{b}\right)} \end{array}$$

The guestimate of  $P_{RC}$  is used as a reference for the accuracy. As described above this turns out to be a very good guestimate and thus gives confidence for being a good reference for accuracy. A tolerance of  $1e - 18$  is found by trial and error to improve accuracy.

The step size is a fraction of the first guestimate and, again by trail and error, is found to improve the number of iterations, roughly 3 - 6, when the step size is chosen to be  $\frac{1}{100}^{th}$  of  $P_{RC}$ . A larger step size does not improve the number of iterations.

The same numerical example as before from [25] is used. The results compare less well unlike for the *Newton Raphson I*;  $P_{RC} = 34.39kN/m$  in [25] where  $P_{RC} = 33.34kN/m$ . Though when implemented in the OST, the results for the  $P_{RC}$  vs the  $X_{RC}$  data, as is shown in appendix B.3, taken from [23] do compare very well with the results from the TP. Furthermore the residual for the numerical example is  $-0.406e^{-15}$  which compares small even to  $\delta_n = 0.106e^{-5}m$ .

Thus there is reason for confidence that the *Newton-Raphson* algorithm to determine the line contact forces  $P_{RC}$ , too, has been implemented correctly.

## References

- [1] Achenbach JD, *Wave propagation in elastic solids*, The technological institute, Northwestern University, Evanston Illinois, NHPC Amsterdam, AEPC New York, 1973.
- [2] Alexander S, *Heave Compensation - In Service Experience*, Acergy, Heave Compensation Workshop, Schiphol, February 2010.
- [3] Alp industries, *Wire rope inspection*, www.alpind.com, 2010.
- [4] Belderbos E, *Analysis of slack wire occurrence in the jacket lift system of Pieter Schelte*, Thesis M.Sc. in Engineering, Catholic University, Leuven, Belgium & Allseas Engineering, Delft, Netherlands, 2010.
- [5] Cattaneo C, *Sul Contatto di Due Corpi Elastici*, Accademia dei Lincei, Rendiconti, Series 6, folio 27, Part I: p342 - p348, Part II: p434 - 436, Part III: p474 - 478, 1938
- [6] Chi M, *Analysis of operating characteristics of strands in tension allowing end-rotation*, Institute of Ocean Science and Engineering, Department of Civil and Mechanical engineering, Washington D.C., 1971.
- [7] Costello GA, *Theory of Wire Rope*, Springer-Verlag, ISBN 0-387-97189-0, New York Berlin Heidelberg, 1990.
- [8] Costello GA, *Mechanics of Wire Rope*, Department of Theoretical and Applied Mechanics, University of Illinois at Urbana-Champaign, Mordica Lecture-Interwire, Wire Association International, Atlanta, Georgia, may, 2003.
- [9] Coyne J, *Analysis of the Formation and Elimination of Loops in Twisted Cables*, AT&T Bell Laboratories, Whippany, IEEE Journal of Oceanographic Engineering, Vol. 15 No. 2, April 1990.
- [10] Deresiewicz H, *Oblique contact of non-spherical bodies*, Journal of Applied Mechanics, Vol 24, p623-624, 1957.
- [11] Drumheller DS, *Introduction to Wave Propagation in Nonlinear Fluids and Solids*, Cambridge University Press, 1998, ISBN 0521587468.
- [12] Ermolaeva NS, Regelink J, Krutzen MPM, *Hockling behaviour of single- and multiple-rope systems*, Allseas Engineering B.V., Delft, Netherlands, Engineering Failure Analysis, vol. 15, p142-153, November, 2006.
- [13] Feld G, Rueben RL, Owen DG, Crockett AE, *Power ropes and umbilicals - conductor strain under pure bending*, Proceedings of the first International Offshore and Polar Engineering Conference, Vol II, p228-235, 1991.
- [14] Feyrer K, *Wire Ropes: Tension, Endurance, Reliability*, Springer, ISBN-10: 3642070361 ISBN-13: 978-3642070365, 2007.
- [15] Gatti-Bono C and Perkins NC, *Dynamic Analysis of Loop Formation in Cables under Compression*, Mechanical Engineering University of Michigan, The International Society of Offshore and Polar Engineers, ISBN 1-880653-58-3, ISSN 1098-6189, 2002.

- [16] Goss VGA, HeijdenG HM van der, Thompson JMT and Neukirch S, *Experiments on Snap Buckling, Hysteresis and Loop Formation in Twisted Rods*, Society for Experimental Mechanics, 2004.
- [17] Hearmon RFS, *Applied Anisotropic Elasticity*, Oxford University Press, 1961.
- [18] Imrak CE and Erdönmez C, *On the problem of wire rope model generation with axial loading*, Istanbul Technical University, Mathematical and Computational Applications, Vol. 15, No. 2, pp. 259-268, 2010.
- [19] Jiang WG, Warby MK, Henshall JL, *Statically indeterminate contacts in axially loaded wire strand*, European Journal of Mechanics, Vol 27, p69-78, 2007.
- [20] Jun MA, Shi-rong GE, De-kun Z, *Distribution of wire deformation within strands of wire ropes*, Journal of China University of Mining & Technology, Vol 18, No 3, p475-478, 2008.
- [21] Leech CM, Overington MS, *Dynamics of Wire Rope Subjected to Shock Axial Loads*, 14th Annual Offshore Technology Conference 4308, Houston , Texas, 1982.
- [22] Páczelt I, Beleznai R, *Non-Linear contact-theory for analysis of wire rope using high-order approximation in the FEM*, Computers & Structures, Vol 89, p1004-1025, 2011.
- [23] Raof M, Hobbs RE, *Inter-wire slippage and fatigue prediction in stranded ropes for TLP thethers*, Imperial College, U.K., 1982.
- [24] Raof M, Hobbs RE, *Hysteresis in Bridge Strand*, Imperial College, U.K., Proc. Inst. Civ. Engrs., Part 2, 77, Dec, 445-464., 1984.
- [25] Raof M, Hobbs RE, *Analysis of multilayered structural strands*, Journal of Engineering Mechanics, Vol 114, No 7, July, 1988.
- [26] Raof M, *The prediction of axial damping in spiral strands*, Journal of strain analysis, Vol 26, No 4, 1990.
- [27] Raof M, *Methods for analysing large spiral strands*, Journal of strain analysis, Vol 26, No 3, 1991.
- [28] Raof M, Huang YP, Pithia KD, *Response of axially preloaded spiral strands to impact loading*, Computers and Structures, Vol 51, No 2, p125-135, 1992.
- [29] Raof M, Kraincanic I, *Analysis of Large Diameter Steel Ropes*, Journal of Engineering Mechanics, Vol 121, No 6, p667-675, 1995.
- [30] Raof M, Dacies TJ, *Axial fatigue design of sheathed spiral strands in deep water applications*, International Journal of Fatigue, Vol 30, p2220-2238, 2008.
- [31] Raof M, Kraincanic I, *Critical examinations of various approaches used for analysing helical ropes*, Journal of strain analysis, Vol 29, No 1, p43-55, 1994.
- [32] Raof M, Davies TJ, *Simple determination of the maximum axial and torsional energy dissipation in large diameter spiral strands*, Computer and Structures, Vol 84, 2006.
- [33] Raof M, Davies TJ, *Simple determination of the axial stiffness for large diameter independent wire rope or fibre core wire ropes*, Journal of strain analysis, Vol 38, No 6, p577 - 586, 2003.



- [34] Rixen DJ, *Numerical Methods in Engineering Dynamics, lecture notes for wb1416*, Department of Precision and Microsystems Engineering, TU Delft University, Delft, Netherlands, 2008.
- [35] Rosenthal F, *The application of Greenhill's formula to cable hockling*, Ocean Technology Division, Naval Research Laboratory, Applied Mechanics branch, Washington D.C., Journal of Applied Mechanics, p681-683, december 1976.
- [36] Singh MK, Mahto A, Thakur RN, Sinha A, *Failure Analysis of Wire Rope Used for Hoisting in Mining: a Case Study*, Journal of Failure Analysis and Prevention, Vol. 7, No. 2, p87 - 91, 2007.
- [37] Stanova E, Fedorko G, Fabian M, Kmet S, *Computer modelling of wire strands and ropes part II: Finite element-based applications*, Advances in Engineering Software, Vol. 42, p322-331, 2011.
- [38] Stump DM, *The hockling of cables: a problem in shearable and extensible rods*, Department of Mathematics, The University of Queensland, St. Lucia, Australia, International Journal of Solids and Structures, Vol. 37, p515-533, 2000.
- [39] Veldt HH van der , Gilheany JJ, *Propagation of a longitudinal pulse in wire ropes under axial loading*, Experimental Mechanics, Vol. 10, No 10, p401 - 407, 1970.
- [40] Velinsky SA, Anderson GL, Costello GA, *Wire rope with complex cross-sections*, Journal of Engineering Mechanics, ASCE, Vol. 110, p380-391, March, 1984.
- [41] Verreet Ing. R, Ridge Dr. I, *Wire Rope Forensics, Casar Drahtseilwerk*, PR GmbH, Aachen, Germany, 2005.
- [42] Warren CY, Budynas RG, *Roark's formulas for stress and strain*, ISBN 0-07-072542-X, 7th edition, McGraw-Hill, Table 14.1, p702, 2002.
- [43] Wasser FJM , *Pieter Schelte Jacket Lift Sytem*, Graduation at Allseas Engineering B.V. Innovations Department and TU Delft University Offshore Engineering, 2010.
- [44] Washington State Department of Labour & Industries, *Safety Standards for Construction Work*, [http://www.lni.wa.gov/wisha/rules/construction/HTML/296-155L\\_2.htm](http://www.lni.wa.gov/wisha/rules/construction/HTML/296-155L_2.htm), Chapter 296-155, Part L.
- [45] [www.wikihow.com/Start-a-Fire-with-Sticks](http://www.wikihow.com/Start-a-Fire-with-Sticks)